Any sign of Quantum Gravity?

Search for excited gravitons G^* in 13 TeV proton-proton collisions with the ATLAS detector at the LHC

Elisabeth Christensen

Thesis submitted for the degree of
Master in Nuclear and Particle Physics
60 credits

Department of Physics
Faculty of mathematics and natural sciences

UNIVERSITY OF OSLO
Spring 2021

Any sign of Quantum Gravity?

Search for excited gravitons G^* in 13 TeV proton-proton collisions with the ATLAS detector at the LHC

Elisabeth Christensen

"Any sign of Quantum Gravity? Search for excited gravitons G^* in 13 TeV proton-proton collisions with the ATLAS detector at the LHC"
http://www.duo.uio.no/

Abstract

The Standard Model (SM) of particle physics does not incorporate gravity. In addition, it suffers from the hierarchy problem. An approach to these two predicaments is the idea of introducing extra spatial dimensions. The Randall-Sundrum (RS) model proposes that we live in a multi-dimensional Universe consisting of two (3+1)-dimensional branes separated from each other by a five-dimensional bulk in which gravity propagates. The hypothetical massless mediators of gravity, "gravitons", can be detected experimentally in a detector via the leptonic decay of their massive Kaluza-Klein partners. In this thesis we search for high-mass resonances of the lightest Kaluza-Klein graviton G^* in the invariant mass distributions of electron and muon pairs. The exclusion limits for the G^* in pp collisions recorded in the ATLAS detector at $\sqrt{s} = 13\,\text{TeV}$, corresponding to an integrated luminosity of $139\,\text{fb}^{-1}$, are extracted. The data are consistent with the background consisting mainly of SM Drell-Yan, top and diboson processes. "Fake" electrons stemming from non-prompt backgrounds are also taken into account. We interpret the data in terms of a hypothetical RS graviton with coupling to leptons, $k/\overline{M}_{Pl} \in [0.1, 0.3]$, where $\overline{M}_{Pl}$ is the reduced Planck mass. Both statistical and systematic uncertainties are taken into account. Masses less than 4.10 TeV, 4.01 TeV and 4.38 TeV are excluded at 95% C.L. for $k/\overline{M}_{Pl} = 0.1$, while masses less than 5.27 TeV, 4.98 TeV and 5.40 TeV are excluded for $k/\overline{M}_{Pl} = 0.3$ in the electron, muon and combined channels, respectively.

Acknowledgements

First and foremost, I would like to thank my supervisor Farid Ould-Saada, for giving me the opportunity to not only work on the exciting topic of quantum gravity, but also for allowing me to participate workshops at CERN, and to take part in the educational program of ATLAS OpenData developing code. I'd also like to extend my gratitude to my co-supervisor Magnar Kopangen Bugge for invaluable help and suggestions whenever I found myself stuck, and for providing insightful answers to questions I didn't even know to ask. A big thank you goes to Even Simonsen Håland for always taking the time to help out whenever my programming skills fell short.

I'm very grateful to the social environment here at HEPP, with both indoor lunch breaks and social gatherings outdoors, providing a much-needed break from the workload whenever needed. I'd also like to thank my fellow master students Per-Dimitri, Håkon, Alida and Sushma for interesting discussions both on and off the topic of particle physics.

These last few years at Blindern wouldn't be the same without the friends I've made, shaping the experience to be a unique one, thank you. Finally, I'd like to thank my siblings and especially my parents, Tor and Mette, for their continuous support and encouragement throughout my studies.

Elisabeth Christensen

25th May 2021

Contents

List of Figures

List of Tables

Introduction

Withstanding the test of time, the Standard Model (SM) is widely recognised as the most robust theory in particle physics, classifying existing particles in terms of symmetry groups. There exist three generations of leptons, three generations of quarks and particles mediating the forces between them. These include the strong force, electromagnetic and the weak force. The SM also describes the unification of the weak and electromagnetic force, coined the electroweak force. In addition, it also predicts the Higgs boson responsible for spontaneous symmetry breaking. The Standard Model can thereby account for all fundamental forces except gravity.

First developed by Sir Isaac Newton during the 17th century, and extended, to put it mildly, by Albert Einstein in his theory of General Relativity during the beginning of the 20th century, gravity is to date extraordinarily and elegantly described on a classical level. However, this elegance does not necessarily apply to the quantum level. The cornerstones of the Standard Model, provided by quantum field theory described in Ch. 1, do not account for gravity. Nor can gravity be incorporated into the framework of the Standard Model. In other words, we must look for new physics to be sensitive to gravity on a quantum level. One way to do so is by extra dimensional models, one of which is providing the theoretical predictions for this thesis (the Randall-Sundrum model, which is discussed in Ch. 2).

Being provided the theoretical predictions we can embark on an attempt at testing them experimentally. In this thesis, we will do so by studying final states of proton-proton (pp) collisions. When studying interactions between particles we first and foremost need to know their kinematical properties and behaviours in hadron collisions, discussed in Ch. 3. We must also be able to detect and extensively describe the outgoing particles, as outlined in Ch. 4. In this thesis, we will make use of the ATLAS detector at the Large Hadron Collider (LHC) for this purpose. We will make use of Bayesian analysis to help provide some statistical insight into the pp collision data, described in Ch. 5. The focus of this thesis will be the analysis procedure, that is, what we do with the data once we have acquired it from the ATLAS detector. What requirements do we impose on the final state particles to narrow down our search for the excited graviton resonances predicted by the RS model, and what other processes provided by the Standard Model do we need to account for when looking at the data? This, along with statistical inference of the data, is the topic of Ch. 6. Our final results are presented and discussed in Ch. 7.

Part I

Theoretical Overview of the Standard Model and Beyond

Chapter 1

Theoretical Framework

In this chapter we will have a look at the model which summarises our current knowledge about particle interactions, the Standard Model, and the theoretical framework from which the model is based on, discussed in Section 1.1. The Standard Model is discussed in Section 1.2. The material in this chapter is largely based on Refs. [1] and [2].

1.1 The cornerstones of the Standard Model

In order to describe the dynamics of a system consisting of fields $\phi(x)$ and their corresponding derivatives $\partial_\mu\phi(x)$ we may utilize a quantity known as the Lagrangian L, defined as the difference between kinetic and potential energy within the system, and may be written as a volume integral over the Lagrangian density $\mathcal{L}$,

$$L = \int \mathcal{L}(\phi, \partial_\mu\phi) d^3x. \tag{1.1}$$

We may employ the Lagrangian in another important element of quantum field theory (QFT), namely the action S. The action allows us to find the evolution of a system, through its time integral of the Lagrangian. That is,

$$S = \int_{t_1}^{t_2} dt L = \int d^4x \mathcal{L}. \tag{1.2}$$

By the principle of least action, we can find the path of a field in configuration space, between times t_1 and t_2, which requires the least amount of energy [1]. This is done by minimizing the action,

$$\begin{aligned} 0 &= \delta S \\ &= \int d^4x \left\{ \frac{\partial \mathcal{L}}{\partial \phi}\delta\phi + \frac{\partial \mathcal{L}}{\partial(\partial_\mu\phi)}\delta(\partial_\mu\phi) \right\} \\ &= \int d^4x \left\{ \frac{\partial \mathcal{L}}{\partial \phi}\delta\phi - \partial_\mu\left(\frac{\partial \mathcal{L}}{\partial(\partial_\mu\phi)}\right)\delta\phi + \left(\frac{\partial \mathcal{L}}{\partial(\partial_\mu\phi)}\delta\phi\right) \right\}. \end{aligned}$$

By considering $\delta\phi = 0$ at the boundaries, and letting the integral vanish for arbitrary $\delta\phi$, we can simplify the principle of least action and obtain the Euler-Lagrange equation for the motion of a field,

$$\partial_\mu \left(\frac{\partial \mathcal{L}}{\partial(\partial_\mu \phi)} \right) - \frac{\partial \mathcal{L}}{\partial \phi} = 0, \tag{1.3}$$

also known as the equation of motion.

1.1.1 Bosonic and fermionic fields

In order to get a sense of the properties of a relativistic quantum field, we must first understand the definition of a quantum field. There are two main categories of fields, mainly a *bosonic* field, describing scalar and vector fields, and a *fermionic* field describing spinor fields. The intuition behind the naming of these fields will be explained in the following.

Bosonic fields

The primary and perhaps the simplest type of a quantum field is the scalar field ϕ described by the Klein-Gordon (KG) Lagrangian according to eq. (1.3),

$$\mathcal{L}_{KG} = \frac{1}{2} \left[|\partial_\mu \phi|^2 - m^2 |\phi|^2 \right]. \tag{1.4}$$

The equation of motion following $\mathcal{L}_{KG}$ is

$$\left(\partial^\mu \partial_\mu + m^2 \right) \phi(x) = 0, \tag{1.5}$$

where $\partial^\mu \partial_\mu \equiv \frac{\partial^2}{\partial t^2} - \nabla^2$, otherwise known as the Klein-Gordon equation. In order to move from a classical field theory to a quantum field theory, we may utilize a procedure known as *second quantization*. That is, to promote the field wavefunctions ϕ and momentum densities $\pi = \frac{\partial \mathcal{L}}{\partial \dot{\phi}}$, to field operators which obey the canonical commutation relations. Working in the Scrödinger picture, the commutation relations for a real scalar field are

$$\begin{aligned} [\phi(\mathbf{x}), \pi(\mathbf{y})] &= i\delta^{(3)}(\mathbf{x} - \mathbf{y}), \\ [\phi(\mathbf{x}), \phi(\mathbf{y})] &= [\pi(\mathbf{x}), \pi(\mathbf{y})] = 0, \end{aligned} \tag{1.6}$$

where $\delta^{(3)}(\mathbf{x} - \mathbf{y})$ is the Dirac-delta function in three dimensions. We may express the scalar field $\phi(\mathbf{x})$ and its conjugate momentum $\pi(\mathbf{x})$ as

$$\phi(\mathbf{x}) = \int \frac{d^3p}{(2\pi)^3} \frac{1}{\sqrt{2E_\mathbf{p}}} \left(a_\mathbf{p} e^{i\mathbf{p}\cdot\mathbf{x}} + a_\mathbf{p}^\dagger e^{-i\mathbf{p}\cdot\mathbf{x}} \right), \tag{1.7}$$

$$\pi(\mathbf{x}) = \int \frac{d^3p}{(2\pi)^3} (-i) \sqrt{\frac{E_\mathbf{p}}{2}} \left(a_\mathbf{p} e^{i\mathbf{p}\cdot\mathbf{x}} - a_\mathbf{p}^\dagger e^{-i\mathbf{p}\cdot\mathbf{x}} \right), \tag{1.8}$$

where the ladder operators a and $a^\dagger$ can be interpreted as annihilation and creation operators, respectively, of momentum eigenstates with energy $E_{\mathbf{p}}$ and momentum 3-vector $\mathbf{p}$. In other words, they may be thought of as operators calling for particle excitations, carrying an energy-momentum relation $E_{\mathbf{p}} = \sqrt{|\mathbf{p}|^2 + m^2}$ and mass m, of a field. These indistinguishable quanta are known as Klein-Gordon particles, or *bosons* carrying integer spin, and obey the Bose-Einstein statistics. This, in essence, means that under any interchange of two particle states the wave function will remain invariant, and an arbitrary mode $\mathbf{p}$ may contain multiple particles, not subject to the Pauli exclusion principle[1].

Fermionic fields

Perhaps one immediate disadvantage of utilizing the Klein-Gordon equation in classical field theory is its treatment of probability densities. By looking at its possible energy solutions we see that they contain both positive and negative energies:

$$E_{\mathbf{p}} = \pm\sqrt{|\mathbf{p}|^2 + m^2}. \tag{1.9}$$

The probability density, $\rho(\mathbf{x}, t)$, of a wavefunction ψ may be expressed as

$$\rho(\mathbf{x}, t) = \psi^*(\mathbf{x}, t)\psi(\mathbf{x}, t). \tag{1.10}$$

Writing out and rearranging the KG-equation from eq. (1.5) such that the time derivatives are on the LHS and the spatial derivatives along with the mass are contained on the RHS, and taking the difference of the resulting equation and its hermitian conjugate, each multiplied with ϕ^* and ϕ respectively, we obtain

$$\phi^*\frac{\partial^2\phi}{\partial t^2} - \phi\frac{\partial^2\phi^*}{\partial t^2} = \phi^*(\nabla^2\phi - m^2\phi) - \phi(\nabla^2\phi^* - m^2\phi^*),$$

and simplifying

$$\frac{\partial}{\partial t}\left(\phi^*\frac{\partial\phi}{\partial t} - \phi\frac{\partial\phi^*}{\partial t}\right) = \boldsymbol{\nabla}\cdot(\phi^*\boldsymbol{\nabla}\phi - \phi\boldsymbol{\nabla}\phi^*). \tag{1.11}$$

From the charge density continuity equation,

$$\partial_\mu j^\mu = \boldsymbol{\nabla}\cdot\mathbf{j} + \frac{\partial\rho}{\partial t} = 0, \tag{1.12}$$

where $\mathbf{j}$ is the probability current, we may identify the probability density ρ from eq. (1.11) as

$$\rho = i\left(\phi^*\frac{\partial\phi}{\partial t} - \phi\frac{\partial\phi^*}{\partial t}\right) \quad \text{and} \quad \mathbf{j} = -i(\phi^*\boldsymbol{\nabla}\phi - \phi\boldsymbol{\nabla}\phi^*),. \tag{1.13}$$

[1]Due to the nature of indistinguishable particles, a two-particle bosonic state may be written as $\psi_+(\mathbf{x}_1, \mathbf{x}_2) = A\left[\psi_a(\mathbf{x}_1)\psi_b(\mathbf{x}_2) + \psi_b(\mathbf{x}_1)\psi_a(\mathbf{x}_2)\right]$. If $\psi_a = \psi_b$ then $\psi_+(\mathbf{x}_1, \mathbf{x}_2) \neq 0$, thus allowing the two indistinguishable bosons to occupy the same state.

where we include the factor i to ensure that ρ is real. Inserting a plane-wave solution in the probability density we find that $\rho = 2|N|^2 E_{\mathbf{p}}$, with $N \equiv \phi^* \phi$. In other words, the negative energy solutions give rise to negative probability densities! This relationship is due to the Klein-Gordon equation containing second order space and time derivatives. The Dirac equation starts off with a slightly different perspective leading to significant differences from that of Klein-Gordon. The Dirac equation is expressed in terms of first-order derivatives in both space and time,

$$(i\gamma^\mu \partial_\mu - m)\psi(x) = 0, \tag{1.14}$$

which when squared implies the Klein-Gordon equation[2]. The Dirac equation is the equation of motion for the Dirac Lagrangian,

$$\mathcal{L}_{\text{Dirac}} = \bar{\psi}(i\gamma^\mu \partial_\mu - m)\psi. \tag{1.15}$$

Here, $\psi(x)$ is a Dirac spinor and γ^μ are the Dirac-Pauli matrices in a chiral representation. That is,

$$\psi = \begin{pmatrix} \psi_L \\ \psi_R \end{pmatrix}, \text{ and } \gamma^0 = \begin{pmatrix} 0 & 1 \\ 1 & 0 \end{pmatrix}, \gamma^i = \begin{pmatrix} 0 & \sigma^i \\ -\sigma^i & 0 \end{pmatrix}$$

where σ^i are the Pauli spin matrices, and ψ_L and ψ_R are known as the left-handed and right-handed Weyl spinors[3], respectively. Quantizing the Dirac Lagrangian we follow the same formulae as with second quantization, with one exception; the field operator must now obey the canonical *anti*commutation relations[4]. That is,

$$\begin{aligned} \{\psi_a(\mathbf{x}), \psi_b^\dagger(\mathbf{y})\} &= \delta^{(3)}(\mathbf{x} - \mathbf{y})\delta_{ab} \\ \{\psi_a(\mathbf{x}), \psi_b(\mathbf{y})\} &= \{\psi_a^\dagger(\mathbf{x}), \psi_b^\dagger(\mathbf{y})\} = 0 \end{aligned} \tag{1.16}$$

where δ_{ab} is the Kronecker-delta function. The Dirac field operators may be expressed as

$$\psi(x) = \int \frac{d^3p}{(2\pi)^3} \frac{1}{\sqrt{2E_{\mathbf{p}}}} \sum_s \left(a_{\mathbf{p}}^s u^s(p) e^{-ip\cdot x} + b_{\mathbf{p}}^{s\dagger} v^s(p) e^{ip\cdot x} \right) \tag{1.17}$$

$$\bar{\psi}(x) = \int \frac{d^3p}{(2\pi)^3} \frac{1}{\sqrt{2E_{\mathbf{p}}}} \sum_s \left(b_{\mathbf{p}}^{s} \bar{v}^s(p) e^{-ip\cdot x} + a_{\mathbf{p}}^{s\dagger} \bar{u}^s(p) e^{ip\cdot x} \right) \tag{1.18}$$

where $u(p)$ and $v(p)$ originates from the positive and negative frequency solutions of the Dirac equation, respectively,

$$\psi_+(x) = u(p)e^{-ip\cdot x} \text{ and } \psi_-(x) = v(p)e^{+ip\cdot x},$$

[2]Every solution of the Dirac equation is then also a solution of the Klein-Gordon equation.

[3]I.e. they are the eigenstates of the helicity operator, whose eigenvalues reflects the direction of a particle's momentum in relation to its intrinsic spin.

[4]This is to ensure only positive-energy excitations of the vacuum. For the complete derivation of this reasoning the reader is referred to ref. [1], pp. 52-57.

with

$$u^s(p) = \begin{pmatrix} \sqrt{p \cdot \sigma}\xi^s \\ \sqrt{p \cdot \bar{\sigma}}\xi^s \end{pmatrix}, \quad v^s(p) = \begin{pmatrix} \sqrt{p \cdot \sigma}\eta^s \\ -\sqrt{p \cdot \bar{\sigma}}\eta^s \end{pmatrix}, \qquad s = 1, 2$$

where s represents the two possible spin states of a Dirac particle, spin-up $\xi^1 = \eta^1 = \left(\begin{smallmatrix} 1 \\ 0 \end{smallmatrix}\right)$ and spin-down $\xi^2 = \eta^2 = \left(\begin{smallmatrix} 0 \\ 1 \end{smallmatrix}\right)$ along the 3-direction. Again, the ladder operators a and $a^\dagger$ correspond to excitations of a spinor field, carrying energy $E_{\mathbf{p}}$ and momentum $\mathbf{p}$. However, the field operators are also now including the ladder operators b and $b^\dagger$. These represent anti-particles excited from the spinor field. These particles can mathematically be thought of as the negative energy states from eq. (1.9), travelling backwards in time[5]. Physically, they are interpreted as the counterpart of the original particle, characterised by the same properties, except for the charge which is the opposite of that of the particle. For example, the anti-particle of an electron is a positron. The quanta excited from a Dirac spinor field are known as Dirac particles, or *fermions* carrying half-integer spin, and follow the Dirac-Fermi statistics. That is, the wavefunction is anti-symmetric under any interchange of two particle states. An arbitrary mode $\mathbf{p}$ may never contain multiple particles in the same state, i.e. fermions are subject to the Pauli exclusion principle[6].

1.1.2 Symmetries

An astounding feat of classical field theory is the capability of finding the relation between symmetries and conservation laws in nature.[7] In this section we delve into the two main categories representing the transformations leading to potential invariance in a theory; *continuous* and *discrete* transformations.

Continuous symmetries

Noether's theorem [3] states that if a continuous transformation,

$$\phi(x) \to \phi'(x) = \phi(x) + \alpha\Delta\phi(x),$$

leaves the equations of motion, the Euler-Lagrange equation from eq. (1.3), invariant then we may call the transformation a symmetry. This is ensured if the action remains invariant under the transformation. Likewise, for any transformation of the Lagrangian density $\mathcal{L}$,

$$\mathcal{L}(x) \to \mathcal{L}(x) + \alpha\partial_\mu \mathcal{J}^\mu, \qquad \text{with } \mathcal{J}^\mu \equiv \left(\frac{\partial \mathcal{L}}{\partial(\partial_\mu \phi)}\Delta\phi\right),$$

which satisfies the continuity equation from eq. (1.12) we have a conservation law. Noether's theorem can also be applied to spacetime transformations, such as rotations and

[5] According to the Feynman-Stückelberg interpretation.

[6] A two-particle fermionic state is expressed as $\psi_-(\mathbf{x}_1, \mathbf{x}_2) = A\left[\psi_a(\mathbf{x}_1)\psi_b(\mathbf{x}_2) - \psi_b(\mathbf{x}_1)\psi_a(\mathbf{x}_2)\right]$. If now $\psi_a = \psi_b$, then $\psi_- = 0$, meaning the wave function in essence disappears.

[7] As derived by German mathematician Emmy Noether.

translations. Under the infinitesimal transformation $x^\mu \to x^\mu + a^\mu$ of a field configuration $\phi(x)$,

$$\phi(x) \to \phi(x+a) = \phi(x) + a^\mu \partial_\mu \phi(x),$$

the Lagrangian density transforms as

$$\mathcal{L} \to \mathcal{L} + a^\mu \partial_\mu \mathcal{L} = \mathcal{L} + a^\nu \partial_\mu (\delta^\mu{}_\nu \mathcal{L}).$$

From eq. (1.12) the conserved charge is expressed as

$$Q \equiv \int_{\text{all space}} j^0 d^3x.$$

Discrete symmetries

There are other symmetries within nature which cannot be described by continuous transformations. These are known as *discrete* symmetries, and require specific spacetime operations on the field. A discrete transformation $\hat{X}$ is regarded as a symmetry if it commutes with the Hamiltonian of the system, that is $[\hat{X}, H] = 0$. As seen above, the continuous spacetime transformations are in the form of e.g. translations and rotations. But what about reflections in spacetime? This is where discrete symmetries enter. A short introduction to three types of discrete symmetries of the Lorentz group acting on the Dirac spinor field will be given here.

- *Parity*: When acting on the wavefunction of a particle, parity (a Hermitian operator denoted by P) acts as a spatial reflection of a particle's position without affecting its intrinsic spin. That is,

  $$P\psi(t, \mathbf{x})P = \gamma^0 \psi(t, \mathbf{x}).$$

  When parity acts on a fermion-antifermion state, such as $a^{s\dagger}_{\mathbf{q}} b^{s\dagger}_{\mathbf{q}} |0\rangle$ we get an additional (-1), that is $P(a^{s\dagger}_{\mathbf{p}} b^{s'\dagger}_{\mathbf{q}} |0\rangle) = -(a^{s\dagger}_{-\mathbf{p}} b^{s'\dagger}_{-\mathbf{q}} |0\rangle)$.

- *Time reversal*: The application of time reversal (denoted by T) does not invert the spatial components of a particle, but rather time,

  $$T\psi(t, \mathbf{x}) = (-\gamma^1\gamma^3)\psi(-t, \mathbf{x}),$$

  with a relative minus "+"-sign occurring when dealing with anti-fermions. This effect not only reverses the momentum of a particle, but also its spin orientation. That is, $T a^s_{\mathbf{p}} T = a^{-s}_{-\mathbf{p}}$ and $T b^s_{\mathbf{p}} T = b^{-s}_{-\mathbf{p}}$.

- *Charge conjugation*: The operator representing charge conjugation (denoted by C) acts as a map between fields ψ and $\bar{\psi}$. That is, it represents the symmetry between particles and anti-particles:

  $$C\psi(x)C = -i(\bar{\psi}\gamma^0\gamma^2)^T, \text{ or } C a^s_{\mathbf{p}} C = b^s_{\mathbf{p}}$$
  $$C\bar{\psi}(x)C = (-i\gamma^0\gamma^2\psi)^T, \text{ or } C b^s_{\mathbf{p}} C = a^s_{\mathbf{p}}$$

One explicit property of the discrete symmetries is that a field theory may be invariant under a specific combination of said symmetries, such as CP[8], although it may violate the symmetries separately. However, in order for a quantum field theory to remain Lorentz invariant it must remain invariant under the combination CPT, which is regarded as a perfect symmetry of nature. This means that if CP is violated, so too must T be violated. Correspondingly, if CP is not violated, T must also not be violated.

Another useful concept is that of *chirality*, which is introduced when we are dealing with parity violations in weak interactions, discussed in subsection 1.1.3. Chiral projection operators allow us to decompose any Dirac spinor into so-called *left*- and *right*-handed chiral states, that is

$$P_L \equiv \frac{1}{2}(1-\gamma^5),\ P_R \equiv \frac{1}{2}(1+\gamma^5)$$
$$\psi(x) = \psi_L(x) + \psi_R(x) \equiv P_L\psi(x) + P_R\psi(x)$$

where the eigenvalues of the γ^5-matrix, with $\gamma^5 = i\gamma^0\gamma^1\gamma^2\gamma^3$, determine the *handedness* of particles. That is, left-handed (LH) chiral states have eigenvalue -1, while right-handed (RH) have $+1$.

1.1.3 Gauge invariance

A gauge transformation has the explicit property of transforming the fields themselves, and is known as an *internal symmetry* if it leaves the Lagrangian invariant. We distinguish between two types of transformations: a *global* transformation, which can act upon free, non-interacting fields as a whole by the use of an arbitrary phase factor χ, and a *local* transformation whose phase factor is dependent on spacetime variables, $\chi(x)$. A local gauge transformation introduces new degrees of freedom in the form of vector fields, i.e. gauge bosons, thus promoting the theory to one describing interacting fields. The conserved quantities associated with internal symmetries are related to the charges of distinct fundamental forces. We categorize the gauge groups related to internal symmetries according to the behaviour of the so-called *generators* of a group, which is briefly summarized below. Three examples of gauge transformations leading to the fundamental forces described in the Standard Model are included to demonstrate the wonders of gauge invariance[9].

Abelian gauge groups

When performing unitary transformations on N-dimensional vectors, we refer to the collective term $U(N)$ from *Lie algebra*. Such a transformation has the property of commuting with any other unitary transformation, and classifying them as *Abelian*. The $U(N)$ transformations are expressed in terms of a local phase rotation,

$$\psi(x) \to \psi'(x) = e^{ig\alpha(x)}\psi(x), \tag{1.19}$$

[8] An example of a CP-violating process is Kaon weak decay.

[9] For this reason, we will restrict ourselves to mainly include examples of unitary transformations, $U(N)$, and special unitary transformations, $SU(N)$.

with a scale factor g and an arbitrary phase factor $\alpha(x)$.

- *Quantum electrodynamics:* The unitary symmetry group U(1) can be expressed in terms of the local phase rotation shown in eq. (1.19) with the space-time phase factor $\alpha(x)$. Do note, however, that simply imposing this transformation on the free-particle Dirac equation from eq. (1.14) does not result in any invariance of the theory, but rather an additional term involving $\alpha(x)$[10]. Therefore, in order to ensure invariance we must introduce a new field A_μ. This leaves the Dirac equation as

$$i\gamma^\mu(\partial_\mu + iqA_\mu)\psi - m\psi = 0, \tag{1.20}$$

with the condition that A_μ transforms according to

$$A_\mu \to A'_\mu = A_\mu - \frac{1}{g}\partial_\mu\alpha(x),$$

thereby cancelling out the additional phase term. A_μ can be interpreted as the vector field for a massless gauge boson, that is the photon (γ), which carries an electromagnetic potential. The introduction of the field A_μ, by a local phase rotation of $\psi(x)$, leads to the field theory of *quantum electrodynamics* (QED), whose corresponding Lagrangian is expressed as

$$\begin{aligned}\mathcal{L}_{QED} &= \bar{\psi}(i\partial\!\!\!/ - m)\psi - \frac{1}{4}(F_{\mu\nu})^2 - g\bar{\psi}\gamma^\mu\psi A_\mu \\ &= \bar{\psi}(iD\!\!\!/ - m)\psi - \frac{1}{4}(F_{\mu\nu})^2,\end{aligned} \tag{1.21}$$

where $F_{\mu\nu} = \partial_\mu A_\nu - \partial_\nu A_\mu$ is the electromagnetic field tensor, and D_μ is the *gauge covariant derivative*

$$D_\mu \equiv \partial_\mu + igA_\mu(x),$$

which arises due to the invariance of the Lagrangian under local phase rotations. An interaction within QED can thereby be described by the vertex factor $-ig\gamma^\mu$, from the interaction term $\mathcal{L}_{QED} \supset g\bar{\psi}\gamma^\mu\psi A_\mu$, corresponding to the Feynman diagram in figure 1.1. The conserved charge of QED is the electric charge q.

Non-Abelian gauge groups

A subgroup of unitary transformations is the Lie group $SU(N)$, which consists of $N \times N$ unitary transformations with determinant 1. Furthermore, the transformations contain $N^2 - 1$ non-commuting Hermitian generators t^a. The transformations related to the $SU(N)$ group are expressed as

$$\psi(x) \to \psi'(x) = e^{ig\alpha^i(x)t^i}\psi(x) \tag{1.22}$$

[10]Generally speaking, imposing a local phase transformation on a free-particle (non-interacting) theory does not result in an invariance of the theory.

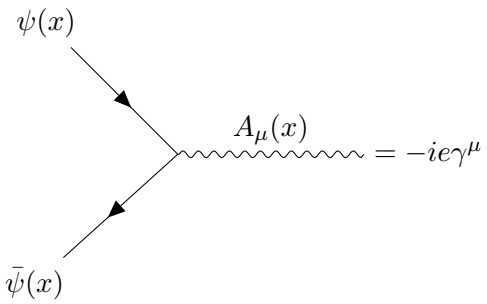

Figure 1.1: With time moving from left to right, this Feynman diagram of a basic QED vertex describes the interaction between a fermion and an anti-fermion field, ψ and $\bar{\psi}$ respectively, with coupling strength $g \equiv +|e|$, annihilating to a photon carrying an electromagnetic potential A_μ.

acting on an N-plet vector

$$\psi(x) \equiv \begin{pmatrix} \psi_1(x) \\ \vdots \\ \psi_N(x) \end{pmatrix}.$$

Due to the non-commuting property of the generators the $SU(N)$ symmetry falls under the category of a *non-Abelian* theory. In other words,

$$[t^i, t^j] = if^{ijk}t^k \tag{1.23}$$

where f^{ijk} are known as *structure constants*. In order to promote the global gauge transformation to a local one we must take into account the covariant derivative

$$D_\mu \equiv \partial_\mu - igA^i_\mu t^i, \tag{1.24}$$

where A^i_μ corresponds to the $N^2 - 1$ different gauge fields in the $SU(N)$ group. Furthermore, to ensure gauge invariance we must require the fields, A_μ, to transform as

$$A^i_\mu \to A'^i_\mu = A^i_\mu + \frac{1}{g}\partial_\mu \alpha^i + f^{ijk}A^j_\mu \alpha^k. \tag{1.25}$$

The corresponding Lagrangian for an $SU(N)$ symmetry is then

$$\mathcal{L} = -\frac{1}{4}(F^i_{\mu\nu})^2, \text{ where } F^i_{\mu\nu} = \partial_\mu A^i_\nu - \partial_\nu A^i_\mu + gf^{ijk}A^j_\mu A^k_\nu, \tag{1.26}$$

where the last term introduces self-interactions between the gauge bosons. Adding the Lagrangian for the gauge field into the Dirac Lagrangian and replacing the ordinary partial derivative with the covariant derivative we can promote the field theory into one interacting with fermions, that is

$$\mathcal{L}_{YM} = \bar{\psi}(i\not{D} - m)\psi - \frac{1}{4}(F^i_{\mu\nu})^2, \tag{1.27}$$

known as the Yang-Mills Lagrangian.

- *The weak interaction*: The special unitary symmetry group SU(2) corresponds to replacing the generators with Pauli spin matrices, that is $t^i \to \frac{1}{2}\sigma^i$. The covariant derivative thereby becomes

$$D_\mu \equiv \partial_\mu - ig\frac{\sigma^i}{2}W_\mu^i,$$

where W^i corresponds to three gauge fields of the $SU(2)$ group. Since the generators are functions of the 2×2 Pauli spin matrices, the wavefunction $\psi(x)$ must be expressed as a doublet, coined a *weak isospin doublet*, where the members of the doublet always differ by one unit in electric charge. The first generation of quarks, q, and leptons, l, are defined as

$$q(x) = \begin{pmatrix} u(x) \\ d(x) \end{pmatrix}, \quad l(x) = \begin{pmatrix} \nu_e(x) \\ e^-(x) \end{pmatrix}.$$

The conserved charge associated with the $SU(2)$ symmetry is that of *isospin* I, more specifically the third component of the isospin $I_W^{(3)}$. The upper member of the isospin doublet carries $I_W^3 = +1/2$, while the lower member carries $I_W^3 = -1/2$. As mentioned, in subsection 1.1.2, a spinor field can be projected into a left- and right-handed component. The $SU(2)$ gauge transformation affects only LH particles and RH antiparticles [4]. For this reason, any RH particles and LH antiparticles are placed in isospin singlet states with $I_W^3 = 0$, and we therefore refer to the symmetry as $SU(2)_L$. This is the gauge group which defines the second fundamental force of nature, namely the *weak force*. It should however be mentioned that the three gauge bosons do not correspond to the physical bosons observed in experiments, as is discussed in subsection 1.2.1. Figure 1.2 shows examples of weak interaction Feynman diagrams.

- *Quantum chromodynamics*: The generators of the $SU(3)$ group are $t^i \equiv \frac{1}{2}\lambda^i$, where λ^i is defined as the 3×3 Gell-Man matrices, such that the covariant derivative becomes

$$D_\mu \equiv \partial_\mu - ig\frac{1}{2}\lambda^i G_\mu^i, \tag{1.28}$$

where G_μ^i corresponds to the 8 gauge fields of the $SU(3)$ group, exciting the gauge bosons termed *gluons*. Following the logic of Noether's theorem, the Yang-Mills theory related to the $SU(3)$ group must have a conserved quantity. This conserved quantity is that of colour charge[11]. There are three colour charges (red, green and blue) which are mediated by the gluons, and correspond to the charges conserved within the third fundamental force, known as the *strong force*, described by the field theory of *quantum chromodynamics* (QCD). The only fermions carrying colour charge are quarks. It goes without saying that the wavefunction is described

[11] We thus also refer to the $SU(3)$ group as $SU(3)_C$.

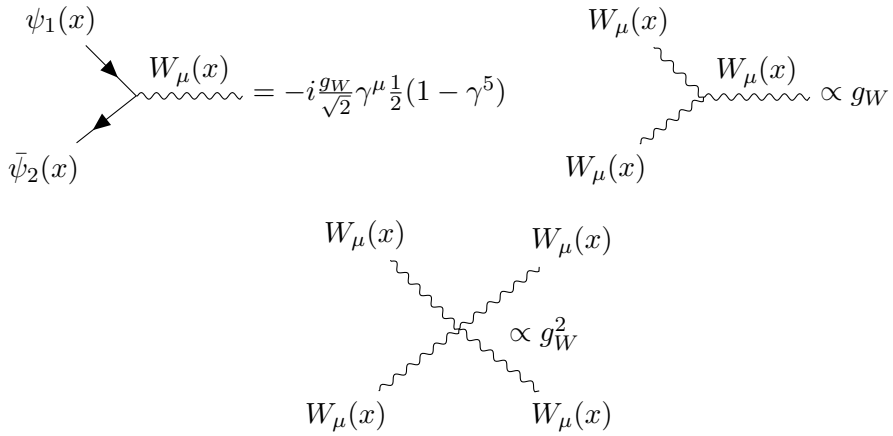

Figure 1.2: With time moving from left to right, the Feynman diagram to the top left describes a weak interaction vertex between two spinor elements of a weak isospin doublet and a gauge boson W, with coupling strength $g \equiv g_W$, while the diagrams to the top right and bottom describe the self-interactions of gauge bosons W.

as an $SU(3)_C$ triplet,

$$q_C(x) = \begin{pmatrix} q_r(x) \\ q_g(x) \\ q_b(x) \end{pmatrix},$$

for each quark flavour (six in total). Due to the self-interaction term in eq. (1.25) there will also be self-interactions between the gluons, as seen in figure 1.3.

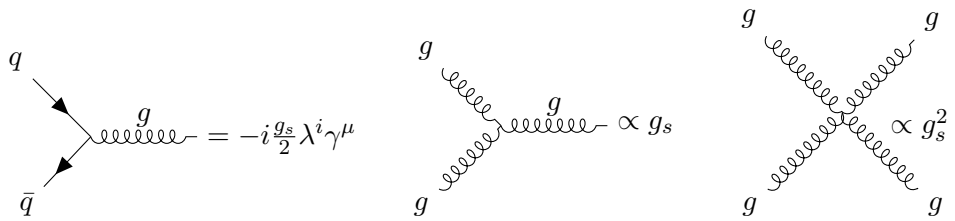

Figure 1.3: With time moving from left to right, the Feynman diagram to the left describes a QCD interaction vertex between two quarks and a gluon g, excited from the gauge field G^μ, with coupling strength g_s, while the diagrams from center to the right describe the self-interactions of gluons.

1.2 The Standard Model

The combination of the three gauge groups described in subsection 1.1.3, along with three generations of leptons and three generations of quarks, make up the gauge field theory

$$U(1)_Y \otimes SU(2)_L \otimes SU(3)_C,$$

also known as the Standard Model (SM) of particle physics [2, 5, 4, 6], seen in figure 1.4. Each subindex on the symmetries corresponds to the conserved quantities in the field theory. That is, $U(1)_Y$ conserves *hypercharge*, discussed further below, experienced by all leptons and quarks carrying an electric charge or non-zero $I_W^{(3)}$, $SU(2)_L$ ensures weak interaction couplings to only LH-particles and RH-antiparticles, while $SU(3)_C$ conserves colour charge, mediated only between quarks by gluons.

1.2.1 Experimental implications

What has not yet been addressed is the physical implications of the field theory, in other words the actual measurements made in the laboratory of elementary particles. One of which is the observation of massive weak gauge bosons. This stands in contrast to that of the prediction of massless gauge bosons in the $SU(2)_L$ field theory. The explanation of this phenomenon was proposed in the Glashow-Weinberg-Salam (GSW) model [7, 8, 9] through the unification of the weak and electromagnetic symmetries, coined the *electroweak* symmetry, combined with a non-zero vacuum expectation value.

Electroweak symmetry

There are as mentioned three generators of the $SU(2)_L$ field theory giving rise to three gauge bosons, $W_\mu^{(1)}, W_\mu^{(2)}$ and $W_\mu^{(3)}$. The charged gauge bosons can be expressed in terms of the linear combinations

$$W_\mu^{\pm} = \frac{1}{\sqrt{2}} \left(W_\mu^{(1)} \mp i W_\mu^{(2)} \right).$$

It is tempting to define $W_\mu^{(3)}$ as the neutral gauge boson Z^0 of $SU(2)_L$. This is however contradicted by experiments, implying that Z^0 couples to both left- and right-handed particles. By unifying QED and the weak interaction we are left with two neutral gauge fields, A_μ and Z_μ, along with the two charged gauge fields, W_μ^+ and W_μ^-. This unification asserts an additional constraint on the $U(1)$ symmetry, by demanding a new conserved quantity, known as *hypercharge*,

$$Y = 2(Q - I_W^{(3)})$$

where Q is the electric charge of a particle with third component isospin $I_W^{(3)}$. Thus, the gauge transformation of a fermionic field $\psi(x)$ is expressed as

$$\psi(x) \to \psi'(x) = e^{ig' \frac{Y}{2} \xi(x)} \psi(x),$$

thereby introducing a new gauge field B_μ to the interaction term

$$\mathcal{L} \supset g' \frac{Y}{2} \gamma^\mu B_\mu \psi,$$

with coupling strength g'. Under this transformation the gauge fields A_μ and Z_μ may now be expressed as the linear combinations

$$\begin{aligned} A_\mu &= B_\mu \cos\theta_W + W_\mu^{(3)} \sin\theta_W, \\ Z_\mu &= -B_\mu \sin\theta_W + W_\mu^{(3)} \cos\theta_W, \end{aligned}$$

with θ_W being the weak mixing angle. The linear combination of Z_μ entails the coupling of Z^0 to both LH and RH particles, but in an asymmetric way, as indicated by observations.

Higgs mechanism

The electroweak unification $U(1)_Y \otimes SU(2)_L$ does not, in itself, evoke the mass acquired by the gauge bosons. This occurs when embedding *spontaneous symmetry breaking* (SSB) into the field theory, in which one chooses a non-zero vacuum ground state[12] ϕ_0 of the system, thereby breaking its invariance. For example, if we consider a complex scalar field ϕ with the Lagrangian

$$\mathcal{L} = -\frac{1}{4}(F_{\mu\nu}^2) + |D_\mu \phi|^2 - V(\phi) \tag{1.29}$$

and potential

$$V(\phi) = -\mu^2 \phi^* \phi + \frac{\lambda}{2}(\phi^* \phi)^2, \tag{1.30}$$

then the Lagrangian (1.29) will remain invariant under the $U(1)$ transformations

$$\phi(x) \to e^{i\alpha(x)} \phi(x) \quad \text{and} \quad A_\mu(x) \to A_\mu(x) - \frac{1}{e}\partial_\mu \alpha(x). \tag{1.31}$$

If we choose $\mu^2 > 0$ then the $U(1)$ global symmetry will be spontaneously broken, as we obtain a non-zero expectation value

$$\langle \phi \rangle = \phi_0 = \left(\frac{\mu^2}{\lambda} \right)^{1/2}. \tag{1.32}$$

Inserting (1.32) back into the potential,

$$V(\phi) = -\frac{1}{2\lambda}\mu^4 + \frac{1}{2} \cdot 2\mu^2 \phi^4 + \mathcal{O}(\phi_i^3), \tag{1.33}$$

[12]The vacuum state is the lowest energy state of a field ϕ and is equivalent to the minimum of the field's potential.

we have now acquired a mass $m = \sqrt{2}\mu$ for the gauge field ϕ_1. In other words, it is a non-zero vacuum expectation value $\langle \phi^0 \rangle$ which allows gauge bosons like $W^{\pm}$, Z^0 to gain mass. This mechanism is known as the Brout-Englert-Higgs mechanism [6, 10], and was confirmed in 2012 by the experimental discovery of the Higgs boson [11], the gauge boson related to the Higgs field[13].

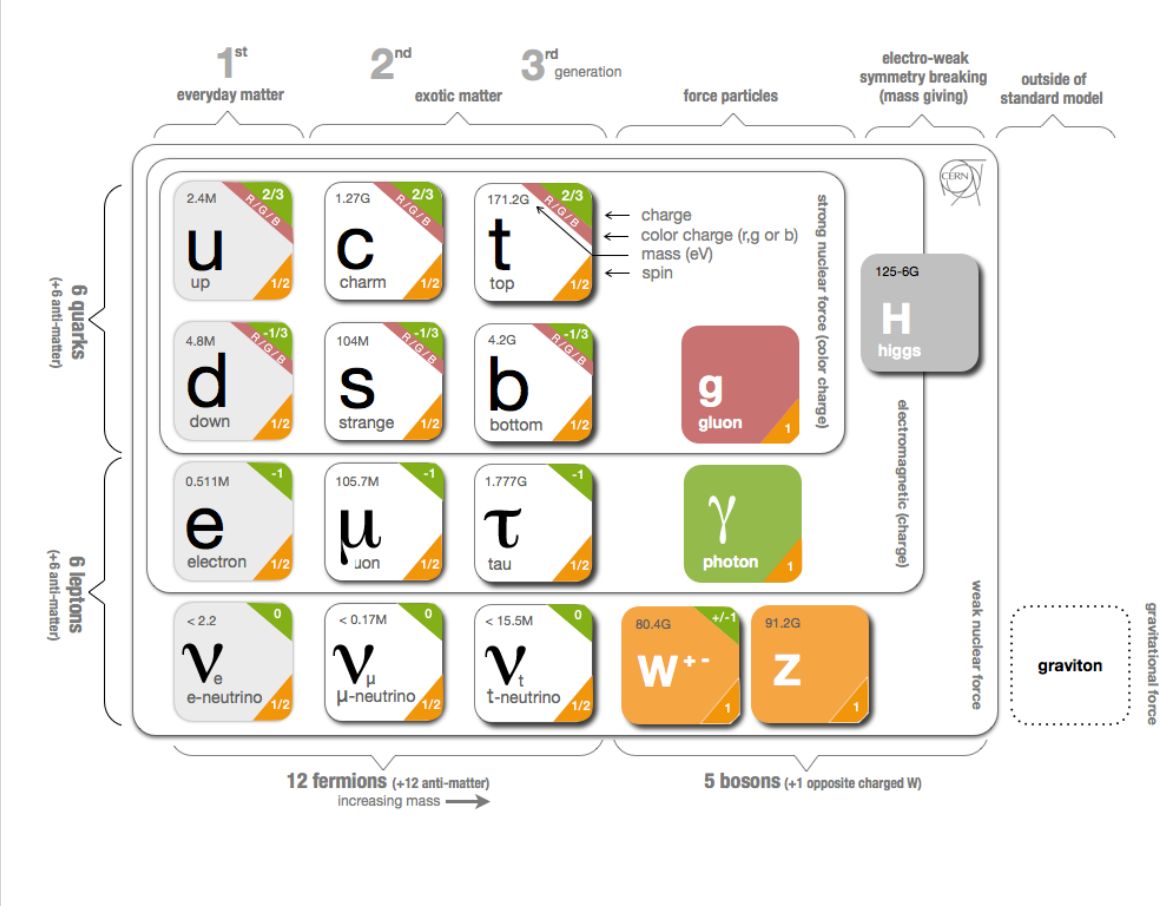

Figure 1.4: The Standard Model of elementary particles, consisting of three generations of leptons and three generations of quarks, along with corresponding antiparticles, as well as the gauge bosons contained within the field theories $[SU(2)_L \otimes U(1)_Y]$ and $SU(3)_C$ and the Higgs boson originating from the Higgs mechanism. Figure taken from [12].

1.2.2 Shortcomings

Despite the veracity of the Standard Model, withstanding the test of time throughout the past 50 years and perhaps being the most predictive theory in all of Physics, it still

[13] Also the latest contribution to the Standard Model.

remains a subject to unanswered questions. Some of which will be discussed in short below.

Experimental observations within high energy physics

- *Gauge couplings:* The coupling constants of the Standard Model are all of similar magnitude. This, in turn, provides a hypothesis of unification of the couplings at some higher energy scale where their corresponding magnitudes intersect, $\Lambda_{GUT} \sim 10^{16}\,\text{GeV}$. The Standard Model is believed to be the low-energy approximation of this hypothesis, providing *only* a unification of the weak and electromagnetic force. A theory which can render the unification of *all* fundamental forces, and the coupling constants of the corresponding gauge interactions, is known as a *grand unified theory* (GUT).

- *Dark matter and dark energy:* The necessity for dark matter first became a topic of discussion when attempting to explain the velocity distribution of stars within galaxies. It is believed to make up about 85% of all matter, and 27% of the mass-energy density, present in the Universe, while the Standard Model achieves to explain only about 5% of all mass-energy. There is no dark matter candidate in the Standard Model, nor does the Standard Model provide a description of dark energy. That is, the energy, which makes up about 68% of the mass-energy density, required to provide the observed acceleration in the expansion of the Universe.

- *Matter-antimatter asymmetry:* After the expansion and temperature decrease of the early Universe, the number of baryons and antibaryons remained approximately constant[14], $n_B - n_{\overline{B}} \approx$ constant. However, observations today imply that the Universe is dominated by matter. How can this be? In order for a matter-antimatter asymmetry to take place three conditions must be satisfied. The first of which is non-constant baryon number. The second is deviation from thermal equilibrium, and the third demands C and CP-violation to have taken place. The Standard Model includes CP-violation in weak interactions between quarks and leptons [4]. This alone, however, does not satisfy the sheer number of CP-violating processes which must have taken place resulting in the observed baryon-antibaryon asymmetry.

Theoretical aspects within high energy physics

- *Free parameters:* So far there are 25 free parameters within the Standard Model. These are the results of measurements made in experiments, and include parameters such as fermion masses, gauge bosons masses, Higgs mass, coupling constants and mixing angles of neutrinos and quarks. In other words, the values of these parameters are not derived from any greater theoretical models.

[14] Referred to as the *Big bang baryogenesis*.

- *Gravity:* The current description of gravity, the theory of General Relativity, does not have an equivalent nor compatible quantum description at the Planck scale, $\Lambda_{Pl} \sim 10^{19}\,\text{GeV}$, contained within the Standard Model.

- *Hierarchy problem:* If the Standard Model were to describe a grand unified theory, in other words, describing the interactions of particles approaching energy scales such as $\Lambda_{GUT} \sim 10^{16}\,\text{GeV}$, the required loop corrections to the Higgs boson increases in Λ^2. This implies that the Higgs mass too must increase beyond that of the electroweak scale. One of the theories postulating a solution to this problem is that of supersymmetry, cancelling the loop corrections by the introduction of *sparticles*, supersymmetric partners of particles.

1.3 Summary

Up until now we have taken a look at quantum field theory of which the Standard Model of particle physics is based on, and some unanswered questions which the Standard Model cannot account for. This motivates potential physics beyond the Standard Model. In the next chapter we will have a look at why we cannot use the quantum field theory description to incorporate quantum field theory into the Standard Model. In addition we will have a look at a theory which proposes a solution to the hierarchy problem and that of quantum gravity by the introduction of Kaluza-Klein partners of the graviton propagating in extra dimensions.

Chapter 2

Quantum Gravity and Extra Dimensions

Gravitational effects on a quantum level only become significant at the Planck scale $\sim 10^{-33}\,\text{cm}$, where gravity couples to other particles as strongly as the other gauge bosons do[1]. The length of the Planck scale is the equivalent wavelength a photon must have to reach the corresponding energy of the Planck scale at approximately $10^{19}\,\text{GeV}$. To probe anything at this energy already proves a challenge, requiring massive engineering feats not likely to happen in the nearby future. This is however not the only challenge to overcome, the primary one being to find a theory of quantum gravity. Section 2.1 takes a look at how simply quantizing gravity leads to a non-renormalizable theory, where the material from this section is based on Refs. [13] and [14]. Section 2.2 explores physics beyond the Standard Model in the search for a theory of quantum gravity, and is based on Refs. [15] [16], [17] and [18].

2.1 From the perspective of quantum field theory

In order to describe an appropriate quantum field theory we quantize the Lagrangian density $\mathcal{L}$ governing the dynamics of a classical field. The Lagrangian for gravity is incorporated in the Einstein-Hilbert action [13]

$$S_{EH} = \frac{1}{16\pi G_N}\int d^4x\sqrt{-g}\mathcal{R}[g] \equiv \frac{1}{2}\int d^4x\sqrt{-g}\mathcal{R}[g]\overline{M}_{Pl}^2, \tag{2.1}$$

[1]The value of $10^{-33}\,\text{cm}$ is quite a significant value, but perhaps difficult to envision. An example would be taking a dot with the width of a human hair ($\sim 0.1\,\text{mm}$) and scaling this up to the size of the observable universe (~ 93 billion light-years). The Planck length would then be the equivalent size of a human hair's width within that "dot-universe".

where G_N is the Newtonian gravitational constant, $g \equiv \det\{g^{\mu\nu}\}$ is the metric[2], $\mathcal{R}$ is the Ricci curvature scalar and $\overline{M}_{Pl} \equiv 1/\sqrt{8\pi G_N} \sim 2 \times 10^{18}$ GeV is the reduced Planck mass. A more detailed description of the metric and the Ricci scalar can be found in Appendix A.

Just like any other quantum field theory, we assume there exists a hypothetical gauge boson for gravity, just as the photon exists for electromagnetism. This hypothetical particle is coined the *graviton*, and is the massless spin-2 propagator[3] for our quantized gravitational theory, excited from a field $h^{\mu\nu}$. The graviton couples to anything carrying energy and momentum, and since the graviton itself also carries energy and momentum then $\overline{M}_{Pl}$ must also describe self-interactions.

We can incorporate the graviton into our gravitational field theory by perturbing the flat space (Minkowski) metric, $\eta^{\mu\nu}$, with the field exciting the graviton, i.e.

$$g^{\mu\nu} = \eta^{\mu\nu} + \frac{1}{\overline{M}_{Pl}} h^{\mu\nu}. \tag{2.2}$$

Expanding the action in terms of $h^{\mu\nu}$, we get

$$S_{EH} = \int d^4x [(\partial h)^2 + \frac{1}{\overline{M}_{Pl}} h(\partial h)^2 + \frac{1}{\overline{M}_{Pl}^2} h^2(\partial h)^2 + \ldots], \tag{2.3}$$

where the first term describes the kinetic term of the graviton, while the cubic and higher-order terms describe the self-interactions of the graviton. There are two remarks one can take away from this theory of quantum gravity:

i) The relevant coupling for gravity in the quantum theory is $\kappa \equiv 1/\overline{M}_{Pl}$, and the higher-order interaction terms are suppressed by powers of $\overline{M}_{Pl}$.

ii) Experiments today generally probe the electroweak scale, $\Lambda_{EW} \sim 10^3\,\text{GeV}$. The ratio of the electroweak scale and Planck scale is $\Lambda_{EW}/\Lambda_{Pl} \sim 10^{-15}$, i.e. the experience of quantum gravity on a daily basis is negligible.

When operating at low energies, gravity is weak. But, as we approach energies near the Planck scale, the strength of gravity becomes comparable to the other three forces in the SM. Couplings of this type are known as *irrelevant* [13]. Irrelevant couplings imply that the field theory does not behave well at high energies. These types of theories are known as *non-renormalizable*, due to the infinite number of counter-terms which are required to tackle the divergences that appear in higher-order Feynman diagrams. In comparison to

[2] $g^{\mu\nu}$ describes the geometry of the background spacetime. As an example, QFT is set in a Minkowski spacetime, i.e. a flat spacetime in four dimensions using the Minkowski metric $\eta_{\mu\nu}$. As opposed to the metric notation common to most particle physicists, $g^{\mu\nu} = (+,-,-,-)$, the sign notation used for $g^{\mu\nu}$ in this instance is $(-,+,+,+)$.

[3] A scalar (spin-0) field contradicts the equivalence principle, which states that the gravitational potential is independent on velocity. A vector (spin-1) field results in like charges repelling each other, which is not what we see in gravitation where positive masses attract each other. A tensor (spin-2) field not only allows positive masses to attract, but it also gives the gravitational inverse square-law and obeys the equivalence principle.

QED and QCD, whose coupling constants are dimensionless, the divergences that occur from the vertices in Feynman diagrams in quantum gravity cannot be renormalized away.

2.2 From the perspective of extra dimensions

The idea of extra dimensions was first motivated by Theodor Kaluza [19] in 1921 in an attempt to unify electromagnetism and gravitation by the introduction of a fifth dimension on a classical level. The theory of Kaluza was quantized by Swedish physicist Oscar Klein [20] who interpreted the fifth dimension as being microscopic and curled up as a circle with radius R, where R is the order of the Planck length. This solves the problem of not seeing the extra dimension in our day-to-day lives, but on the other hand complicates our search for the extra dimension as this radius is much too small to ever detect, at least with the experimental equipment available to us today. Additionally, the calculated electron mass in the Kaluza-Klein theory turns out to be 10^{22}(!) times heavier than the physical mass of the electron [18]. More modern theories, discussed in subsections 2.2.2 and 2.2.3, approach the subject of gravity contained in extra dimensions from a slightly different perspective; by using geometrical objects known as *branes*.

2.2.1 Branes

Branes are theoretical geometrical objects floating around in a higher-dimensional space-time. We distinguish between different branes by the p number of dimensions they represent, and the umbrella term for branes is thus p-branes. For example, a 0-brane is a point-like particle, a 1-brane is a string, and a 2-brane is a two-dimensional surface much like a *membrane*[4] [21].

2.2.2 ADD model

In the previous section it was assumed that Planck scale is the fundamental short-distance scale setting the strength of the gravitational interaction. But how can we ever probe gravity at distances $\sim 10^{-33}$ cm? What if we instead were to use the experimental certainty of the weak scale, m_{EW}, as the only fundamental short-distance scale in the Universe, thereby removing the premise of the Planck distance? But that also begs the question; how does the usual gravitational coupling strength arise in such an alternative theory?

The above question is what the ADD model [17, 22] attempts to answer, by localizing the Standard Model to a (3+1)–brane immersed by n large extra dimensions of radius R. In this $(4+n)$-dimensional theory, the Planck scale $M_{Pl(4+n)}$ is then approximated as m_{EW}. The gravitational potential $V(r)$ between two masses m_1, m_2 separated at a

[4]Perhaps a more intuitive example would be the ocean effectively acting as a 2-brane, being a part of the surface of the Earth, floating around in a (3+1)-dimensional Universe (as far as we know).

distance r then becomes

$$\begin{aligned} V(r) &\sim \frac{m_1 m_2}{M_{Pl(4+n)}^{n+2}} \frac{1}{r^{n+1}}, \quad r \ll R, \\ V(r) &\sim \frac{m_1 m_2}{M_{Pl(4+n)}^{n+2} R^n} \frac{1}{r}, \quad r \gg R. \end{aligned} \tag{2.4}$$

In the case $r \gg R$ we retrieve the usual $1/r$ dependence, as the gravitational flux lines do not continue to penetrate further into the extra dimensions [17], and thus $r^n \approx R^n$. By setting $M_{Pl(4+n)} \sim m_{EW}$, we can from the square of the 4-dimensional M_{Pl},

$$M_{Pl}^2 \sim M_{Pl(4+n)}^{2+n} R^n, \tag{2.5}$$

find the radius R of the n'th extra dimension,

$$R \sim 10^{\frac{30}{n}-17}\text{cm} \times \left(\frac{1\text{TeV}}{m_{EW}}\right)^{1+\frac{2}{n}}. \tag{2.6}$$

From eq. (2.6), the number of extra dimensions n must be greater or equal to two[5]. Thus, it is the *size* of the extra dimensions which introduces the hierarchy of the graviton coupling strength compared to other gauge couplings in our (3+1)-dimensional world.

As the graviton couples too weakly to be detected in a detector, one way to test the physical consequences of the ADD model is to search for excitations of gravitons in the form of *missing energy* $\not{E}_T$ from collider experiments[6].

2.2.3 Randall-Sundrum model

From the beginning, the ADD model in subsection 2.2.2 employs a metric which is independent of the coordinates of the extra dimensions. This strategy has two main rippling effects in the theory. The first being that the n extra dimensions must be compact in order to be consistent with the well-tested gravitational theory of Newton and that of General Relativity, whereas the (3+1) spacetime dimensions, confined to the brane where the SM resides, remain non-compact. The second consequence is that M_{Pl} depends on the size of the extra dimensions. The Randall-Sundrum (RS) model [15, 16] approaches quantum gravity from a different perspective, in which they do *not* assume the metric to be independent of the extra-dimensional coordinates. This again leaves behind two main consequences signifying the framework of the RS modell. That is, that the universe consists of $4 + n$ non-compact dimensions, and that M_{Pl} is no longer dependent on the size of the extra dimensions but rather curvature. The description of the Randall-Sundrum model is based on Refs. [15] and [16].

[5]When $n = 1$, $R \sim 10^{13}$cm, deviating from the predictions of Newtonian gravity over large distances. If $n = 2$ then $R \sim 100\,\mu\text{m} - 1\text{mm}$.

[6]When a graviton is emitted in a process it will propagate to higher dimensions, thereby leaving behind missing energy in the detector.

Framework of the RS model

The set-up for the Randall-Sundrum model is two flat (3+1)-branes embedded in a five-dimensional bulk spacetime, referred to as the "5D bulk". The SM particles and forces reside on one brane, also known as the TeV-brane[7]. The second brane, placed a certain distance from the TeV-brane, is known as the Planck brane and is where gravity is concentrated. The two branes thereby act as boundaries to the fifth dimension orthogonal to the branes.

The metric

The metric for this scenario is a function of the four-dimensional metric multiplied by an exponential "warp"-factor described by the fifth dimension,

$$ds^2 = e^{-2kr_c\phi}\eta_{\mu\nu}dx^\mu dx^\nu + r_c^2 d\phi^2, \tag{2.7}$$

where k is on the order of the Planck scale[8], $\phi \in [0, \pi]$ is the extra-dimensional coordinate whose interval size is set by r_c, with r_c interpreted as the curvature of the fifth dimension, and x^μ are the usual four-dimensional coordinates. $\eta_{\mu\nu} = diag(1, -1, -1, -1)$ is the flat-space metric. The Planck-brane is placed at $\phi = 0$ while the TeV-brane is placed at $\phi = \pi$. There are different variations of the RS model. The first of which is that one assumes the fifth dimension to be confined to a finite volume, where the branes thereby act as the boundaries for the fifth dimension, also known as the *RS1 model*. The second is where we assume the fifth dimension to have an infinitely large volume and that the TeV-brane is put somewhere inside this volume. This infinitely large volume model is coined the *RS2 model*. A natural consequence arising from warped geometry is a scaling dependency, expressed in terms of the factor $e^{-2kr_c\phi}$. I.e. at any point along $r_c\phi$ between the Planck and the TeV-brane the scaling decreases exponentially, thereby suppressing the gravitational force as it fluctuates across the bulk towards the TeV-brane. In addition, due to the warping of spacetime, the physical masses m observed in our (3+1)-dimensional world positioned at $\phi = \pi$ is due to the scaling of some fundamental mass scale m_0, that is

$$m = e^{-2kr_c\phi}m_0, \tag{2.8}$$

where $kr_c \approx 10$ [15].

Kaluza-Klein modes

The gravitational fluctuations within the RS model satisfy the wave equation

$$(\partial_\mu\partial^\mu - \partial_j\partial^j + V(z_j))\hat{h}(x^\mu, z_j) = 0 \tag{2.9}$$

[7] An anlaog for particles being "stuck" to a lower dimensional brane in a 5D bulk, can be water droplets being "stuck" on a 2D shower curtain in a 3D world.

[8] k is related to the energy on the branes and in the bulk.

with $\mu \in [0,3]$ and j labelling the additional dimensions. Arising from the curvature is the so-called "volcano-potential" $V(z_j)$,

$$V(z_j) = \frac{15k^2}{8(k|z_j|+1)^2} - \frac{3k}{2}\delta(z_j) \tag{2.10}$$

which describes a decreasing quantum mechanical potential away from the Planck brane. The shape of this potential is seen in figure 2.1. We may rewrite the higher-dimensional

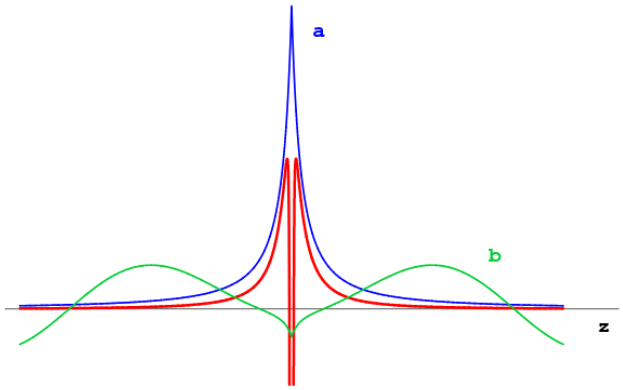

Figure 2.1: Quantum mechanical potential for the continuous KK-modes, dubbed the "volcano-potential" in red, from Ref. [23]. The volcano-potential is made up by (a) a δ-function at the Planck brane representing a single bound state, being the zero-mode graviton (particle that communicates the force of gravity), and (b) the potential for the KK-modes.

gravitational fluctuations $\hat{h}(x^\mu, z_j)$ in terms of four-dimensional Kaluza-Klein modes (KK-modes), i.e. $\hat{h}(x^\mu, z_j) = e^{ip\hat{x}}\hat{\psi}(z_j)$. These modes describe the KK-partners of the graviton, particles which carry momentum in the extra dimension[9]. From the δ-function there exists a single bound state on the Planck brane, which is described as the zero-mode associated with the massless graviton, communicating the force of gravity. The wavefunction in the fifth dimension is defined as

$$\left[\frac{-m^2}{2}e^{-2ky} - \frac{1}{2}\partial_y^2 - 2k\delta(y) + 2k^2\right]\psi(y) = 0, \tag{2.11}$$

with m being the four-dimensional mass of the KK-excitation, and $y \equiv r_c\phi$ representing the coordinate in the fifth dimension. The continuum KK-modes all have $m^2 > 0$, and will be quantized according to the fundamental unit of energy on the TeV-brane. Thus, in theory, there can exist multiple graviton excitations with mass at the TeV scale[10], as

[9] KK-modes are particles which move in the bulk. Being the manifestation of spacetime itself, gravity (mediated by the graviton) propagates in all dimensions and must be the only force propagating in the bulk as forces described by the SM are confined to the TeV-brane. Thus, the KK-modes must be partners of the graviton.

[10] I.e. there may exist a 1 TeV graviton, 2 TeV, 3 TeV and so on.

determined by the coupling $k/\overline{M}_{Pl}$. The reason the KK-modes are interesting is their coupling strength, which is proportional to TeV^{-1} compared to the massless graviton whose coupling strength is proportional to $\overline{M}_{Pl}^{-1}$. That is, the KK-particles couple approximately 10^{15} times more strongly than the graviton. This brings about another important point, the motivation for this thesis; a KK-particle interacts like a weak-scale particle, and can therefore decay in the detector. This allows us to detect it as a resonance via its decay products. The width of these resonances is proportional to $(k/\overline{M}_{Pl})^2$, and we can thus expect narrow resonances for $k/\overline{M}_{Pl} \leq 1$. The most probable KK-mode we can detect in a detector, given the current energy range in collider experiments, is the lightest KK-mode denoted G^*. One can search for graviton excitations in pp collisions via processes such as $q\bar{q} \to G^* \to l^+l^-$ and $gg \to G^* \to l^+l^-$, visualised by the Feynman diagrams in figure 2.2.

Graviton spin signature

When demonstrating that a resonance in the data indeed belongs to the graviton, and not some other exotic object, we can utilize the angular distribution. Since a spin-2 intermediate state is unique to the graviton we can use statistics to differentiate between the angular distributions in collisions, and exclude any particles which may exhibit a spin-1 or spin-0 signature. The angular decay distribution for a graviton, a vector and a scalar boson decaying to a fermion-antifermion pair is shown in table 2.1.

Table 2.1: Angular distributions for a graviton (G), a vector (V) and a scalar (S) boson, with θ^* being the angle between a final state fermion and the beam direction in the centre-of-mass frame of colliding protons. The angular distribution for the graviton is found in Ref. [24].

Process	Distribution
$q\bar{q} \to G \to f\bar{f}$	$1 - 3\cos^2\theta^* + 4\cos^4\theta^*$
$gg \to G \to f\bar{f}$	$1 - \cos^4\theta$
$gg, q\bar{q} \to V \to f\bar{f}$	$1 + \alpha\cos^2\theta^*$
$gg, q\bar{q} \to S \to f\bar{f}$	1

Gravitational potential

The non-relativistic gravitational potential between two particles, m_1 and m_2, on the TeV-brane is expressed as

$$V(r) \sim G_N \frac{m_1 m_2}{r} + \int_0^\infty dm \frac{G_N}{k} \frac{m_1 m_2 e^{-mr}}{r} \frac{m}{k}, \tag{2.12}$$

which, when integrating over dm, is written as

$$V(r) = G_N \frac{m_1 m_2}{r} \left(1 + \frac{1}{r^2 k^2}\right). \tag{2.13}$$

The leading term describes the familiar Newtonian potential, and arises from the zero-mode. The correction term stems from the continuous KK-modes and is considered to be extremely suppressed. Even in the relativistic limit, all proper relativistic corrections are found [16]. One can therefore consider the Randall-Sundrum model to be an effective four-dimensional theory of gravity.

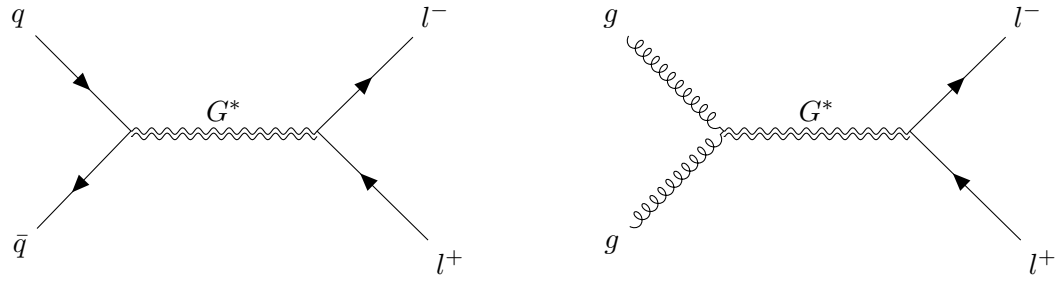

Figure 2.2: With time moving from left to right, these Feynman diagrams describes the processes of (left) $q\bar{q} \to G^* \to l^+l^-$ and (right) $gg \to G^* \to l^+l^-$.

2.3 Summary

In this chapter we have taken a look at the behaviour of quantum gravity as a field theory, and how extra-dimensional models attempt at describing quantum gravity.. The ADD and RS models attempt at resolving the hierarchy problem by specifically confining the Standard Model to a (3+1)-brane floating around in a higher dimensional space, while gravity propagates either in n large, extra dimensions (ADD), or constricting gravity to another brane, acting as a boundary to a fifth dimension (RS). For the remainder of this thesis we will explore the manifestation of gravity at the microscopic scale in presence of extra dimensions using the predictions of the Randall-Sundrum model, in which we will search for potential graviton mass resonances in pp collisions.

Part II

Production and Detection

Chapter 3

Production

In the previous chapter we had a look at the theoretics of the Standard Model, and the phenomena it could not account for. In this and the next chapter we take a look at practical applications and the tools available to us in the search for new physics. The material in this chapter is based on Refs. [2] and [25].

3.1 Kinematics of particles

The motion of a particle is described by its four-momentum, which, to better account for the geometry of the detector, is expressed in terms of polar angle θ and azimuthal angle ϕ,

$$p^\mu = (E, p_x, p_y, p_z) = (E, p_T \cos\phi, p_T \sin\phi, |\mathbf{p}| \cos\theta), \tag{3.1}$$

where the transverse momentum is expressed as $p_T \equiv \sqrt{p_x^2 + p_y^2} = |\mathbf{p}| \sin\theta$. Both the energy and the momentum vector can be expressed as relativistic quantities, that is $E = \gamma m$ and $\mathbf{p} = \gamma m \boldsymbol{\beta}$, where $\gamma = 1/\sqrt{1-\beta^2}$ and $\boldsymbol{\beta} = \mathbf{v}/c$. The four-momentum squared results in the Lorentz-invariant quantity

$$m^2 = p^\mu p_\mu = E^2 - |\mathbf{p}|^2, \tag{3.2}$$

known as the square of the *invariant mass*. For a system containing n particles, m^2 is expressed as

$$m^2 = p^\mu p_\mu = \left(\sum_{i=1}^{n} E_i\right)^2 - \left(\sum_{i=1}^{n} \mathbf{p}_i\right)^2. \tag{3.3}$$

In this analysis, an interaction of the type $2 \to 2$ collision is of interest[1]. The invariant mass of two final state leptons will be denoted as m_{ll}. The total energy in the centre-of-mass (CM) frame, denoted $\sqrt{s}$, is equivalent to the square-root of the quantity in eq. (3.3).

In collisions between hadrons, the CM-frame is not between the partons[2] but rather

[1] See figure 2.2 for the exact Feynman diagrams.

[2] The constituent quarks and gluons which make up a hadron.

the hadrons themselves, where the net longitudinal momentum is given as a function of the energy of the hadron. Thus, the final state particles of a process such as $pp \to l^+l^-$ are boosted along the beam axis. We introduce a kinematic property known as the *rapidity*, y, used to express the lepton angles. The differences in rapidity between particles remain Lorentz invariant under boosts along the beam axis. In the high-energy limit where lepton masses can be neglected we use the property of *pseudorapidity*, η, where $p_z \approx E\cos\theta$,

$$y \equiv \frac{1}{2}\ln\left(\frac{E+p_z}{E-p_z}\right), \quad \eta = -\ln\left(\tan\frac{\theta}{2}\right), \tag{3.4}$$

where the measurable quantities E and p_z represent the energy and momentum z-component of a lepton. The smaller the scattering angle from the beam axis is, the greater $|\eta|$ becomes. If there is a backwards scattering the pseudorapidity turns negative. Additionally, to describe the amount of "activity" around a lepton, we can define a circle of radius ΔR in (η, ϕ)-space surrounding the lepton,

$$\Delta R = \sqrt{(\Delta\eta)^2 + (\Delta\phi)^2}. \tag{3.5}$$

The centre of the circle carries the majority of the momentum, while further out towards ΔRR we find particles carrying lower energies. ΔR is also used to characterise the distance between two particles in (η, ϕ) space.

3.2 Proton-proton collisions

An important parameter in collider physics is the instantaneous luminosity $\mathcal{L}(t)$ which, along with the cross-section σ, determines the number of interactions N taking place in a collider,

$$N = \sigma \int \mathcal{L}(t)dt, \quad \text{where } \mathcal{L} = f\frac{n_1 n_2}{4\pi\sigma_x\sigma_y}, \tag{3.6}$$

where $\sigma_{x,y}$ denotes the beam size, f the frequency of bunch crossings, and $n_{1,2}$ the number of particles in two colliding bunches. The cross-section is expressed as

$$\sigma = \int \frac{d\sigma}{d\Omega}d\Omega, \quad \text{where } \frac{d\sigma}{d\Omega} = \frac{1}{F}\frac{dN}{d\Omega}, \tag{3.7}$$

and describes the probability for an interaction to occur. The differential cross-section $d\sigma/d\Omega$ describes the N number particles scattered into a solid angle $d\Omega$ per unit time per unit flux F (with F being equivalent to the instantaneous luminosity).

3.2.1 Parton distribution functions

At high energies the cross-section for inelastic scattering dominates. As the proton is a mixture of three quarks, denoted *valence* quarks, the quarks are viewed as free

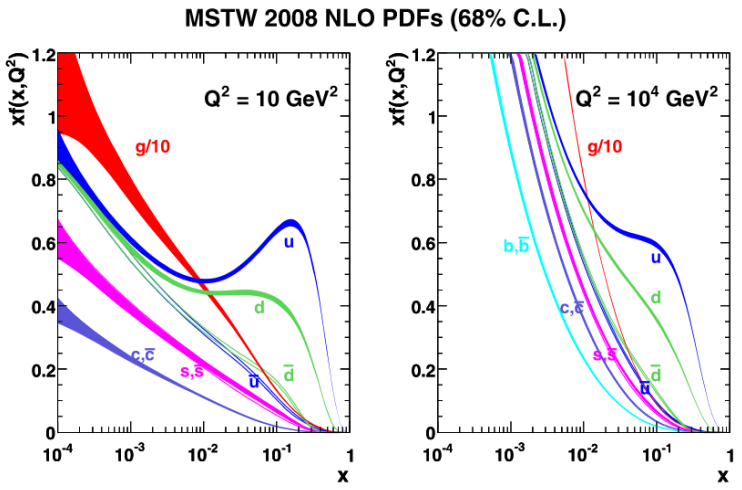

Figure 3.1: Product of proton momentum fraction, x, and parton distribution function, $f(x, Q^2)$, calculated at next-to-leading order (NLO) for two different values of the momentum transfer ($Q^2 = 10\,\mathrm{Gev}^2$ and $Q^2 = 10^4\,\mathrm{GeV}^2$). Taken from Ref. [26].

particles and interact *elastically* in deep inelastic collisions[3]. Each quark carries a certain momentum fraction x, known as Bjorken x, of the proton momentum. In high-energy collisions where the proton mass can be neglected, the invariant mass of two colliding partons q_1 and q_2, with momentum fractions x_1 and x_2 from protons p_1 and p_2 respectively, is expressed as

$$m^2 = x_1 x_2 s, \tag{3.8}$$

where s is the centre-of-mass energy squared of the proton-proton system. The valence quarks within a proton do not only interact with one another by the exchange of virtual gluons, they also emit gluons which decay into $q\bar{q}$-pairs, giving rise to a "sea" of gluons and quarks surrounding the valence quarks. The momenta of partons is dependent on the momentum transfer Q^2 and is represented by an experimentally determined momentum distribution, known as a *parton distribution function* (PDF)[4] $f(x, Q^2)$. That is, the PDF gives the probability for a parton to go into a collision process with momentum fraction x. Examples of PDFs multiplied with the momentum fraction, $xf(x)$, at two different energy scales of Q^2 is shown in figure 3.1. At high Bjorken x the PDFs decrease rapidly. The PDFs at low Bjorken x manifest themselves in what is commonly referred to as *parton-luminosity tails* [27], whose size increases with the resonance width (explained in subsection 3.2.2).

Figure 3.2 shows the schematics of the process $pp \to l^+l^- + X$. The two protons each carry a total momentum p_1 and p_2 along the beam line, respectively. If a quark from $p(p_2)$ emits a gluon, and the gluon in turn produces a quark-antiquark pair, then the

[3]When approaching high enough energies, the collisions between two protons causes each proton to "break apart". The interactions then occur between the partons themselves in the form of elastic collisions.

[4]The contribution of sea quarks is mostly noticeable at low x, due to the suppression of gluon production from $\frac{1}{q^2}$.

antiquark (carrying momentum x_2p_2) could collide with another valence quark (carrying momentum x_1p_1) from proton $p(p_1)$ giving a lepton pair in the final state. The cross-

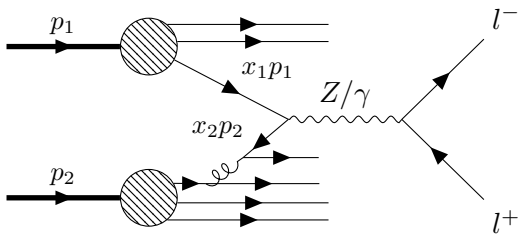

Figure 3.2: Feynman diagram (with time moving from left to right) for the process $pp \to l^+l^- + X$, where X denotes any hadrons formed by the remaining quarks not taking part in the s-channel collision between the $q\bar{q}$-pair carrying momentum fractions x_1 and x_2 from protons $p(p_1)$ and $p(p_2)$, respectively.

section for the process $pp \to l^+l^- + X$ is [1]

$$\sigma(p(p_1) + p(p_2) \to l^+l^- + X) = \int_0^1 dx_1 \int_0^1 dx_2 \sum_f f_f(x_1) f_{\bar{f}}(x_2) \cdot \sigma(q_f(x_1p_1) + \bar{q}_f(x_2p_2) \to l^+l^-), \tag{3.9}$$

where $\sigma(q_f(x_1p_1) + \bar{q}_f(x_2p_2) \to l^+l^-)$ is calculated at the lowest order according to the Feynman diagram drawn at tree-level in figure 3.2.

3.2.2 Breit-Wigner resonance

For an unstable particle, such as the Z boson, the total decay rate (the inverse of the mean particle lifetime τ) is included in its wavefunction, $\psi \propto e^{-imt}e^{-\Gamma t/2} = e^{-it(m-i\Gamma/2)}$. The finite lifetime is also included in the propagator, such that

$$\sigma \propto \left| \frac{1}{q^2 - m_Z^2 + im_Z\Gamma_Z} \right|^2 = \frac{1}{(s - m_Z^2)^2 + m_Z^2\Gamma_Z^2}. \tag{3.10}$$

As the centre-of-mass energy approaches m_Z a peaked resonance at the invariant mass of the unstable particle, referred to as a *Breit-Wigner resonance*, can be seen in the distribution of cross-section vs. $\sqrt{s}$. The decay width Γ is the equivalent of the full width at half-maximum (FWHM) of the corresponding resonance. According to Heisenberg's uncertainty principle, $\Delta E \Delta t \geq \hbar/2$, the smaller the particle lifetime is the greater the uncertainty in its energy becomes.

3.3 Summary

Using the kinematic properties of particles and the knowledge of how they interact in proton-proton collisions we can try and detect them in the real world, by initiating

a reaction from the particles using matter. The next chapter looks into the different interactions particles have in matter and how these reactions can be used to detect and identify the particles in a closed environment.

Chapter 4

Particle Detection and Identification

In order to test a theory we must know how to detect particles in the real world. In this chapter, we will distinguish between the interactions of light particles, such as electrons, from the interactions of heavier particles, such as muons and hadrons. We will make use of Refs. [25] and [28] to describe the interactions of particles in matter, and Ref. [29] when describing the detector setup used in the identification of particles. The detector setup will be supplemented by Refs. [30] and [31] to characterise the reconstruction and identification techniques used.

4.1 Interactions of particles in matter

The passage of particles through matter is characterised by two distinct features; (*i*) the energy loss of a particle and (*ii*) the deflection of a particle from its initial trajectory. All charged particles interact via electromagnetism due to the range of the Coulomb force. The electrons and nuclei within an atom contained in the absorbing material, which the particles are travelling through, deflect the particles from their incident direction by exerting either a repulsive or attractive force. The amount of deflection depends on the mass of the particle, i.e. the greater the mass of passing particles the smaller the deflections. We distinguish between the interactions of light particles (electrons/positrons) and heavier particles (particles with mass heavier than the electron).

4.1.1 Interactions of heavier particles

Most particles interact via inelastic collisions, where parts of the kinetic energy is transferred from the deflected particle to the atom contained in the material, either *exciting* or *ionizing* it. The energy loss from one such interaction is quite small, but the cumulative energy loss from a consecutive number of such interactions[1] leads to a continuous decrease in the particle's energy. The decrease in energy per unit length for a particle,

[1] Which can be described as a stochastic process.

with charge ze and velocity v, traversing a material, with number density N and atomic number Z, is described by the *Bethe-Bloch formula* [28],

$$\left\langle -\frac{dE}{dx} \right\rangle = \frac{4\pi e^4 z^2}{m_0 v^2} NB, \tag{4.1}$$

where

$$B \equiv Z \left[\ln \frac{2m_0 v^2}{I} - \ln \left(1 - \frac{v^2}{c^2} \right) - \frac{v^2}{c^2} \right],$$

with m_0 being the particle rest mass, e the electron charge and c the speed of light. The relative parameter I is determined experimentally and describes the average excitation and ionization potential of the material. In essence, as the particles are slowed down their energy loss increases approximately logarithmically, such that the energy loss per unit length is greater towards the end of its path. This can be explained by the time the particle spends next to an electron; as the velocity of a particle decreases the amount of interaction time increases, thus allowing for a greater amount of energy to be transferred. The potential for energy loss increases for particles with a higher charge, as described by the z^2-dependence in eq. (4.1).

4.1.2 Interactions of electrons and photons

Electrons predominantly lose energy by scattering[2] at low energies. Due to the small mass of the electron we can no longer assume that the incident particle remains undeflected during a collision process. In addition, the collisions now take place between identical particles. These two considerations must be taken into account as corrections to the Bethe-Bloch formula[3].

As the electron/positron approaches higher energies, the main source for energy loss will stem from *bremsstrahlung*, meaning braking radiation in German. Bremsstrahlung occurs when an electron is decelerated by the Coulomb force exerted by a nucleus. The change in kinetic energy manifests itself in the form of a photon, emitted from the electron. The emission probability σ for bremsstrahlung to occur is inversely proportional to the particle's mass squared, $\sigma \propto (e^4/m^2)$ [28]. The emission probability for radiation by muons, the next lightest particle, is on the other hand some 40 000 times smaller than that for electrons.

The energy at which the energy loss from radiation is equal to that from collisions,

$$\left(\frac{dE}{dx} \right)_{\text{rad}} = \left(\frac{dE}{dx} \right)_{\text{col}}, E \equiv E_c, \tag{4.2}$$

coined the *critical energy* E_c, is related to the charge Z of the nucleus and is $E_c \approx 800 m_e/(Z + 1.2)$ [28]. The critical energy acts, in essence, as the lower limit for when

[2]The term scattering can here mean processes such as excitation or ionization of atoms from interactions between electrons, $e^- e^- \to e^- e^-$.

[3]The reader is referred to eq. (2.63) on p. 35 in Ref. [28] for the exact expression.

bremsstrahlung dominates completely. We thus decompose the energy loss for an electron into a radiation term (rad) and a collision term (col),

$$\frac{dE}{dx} = \left(\frac{dE}{dx}\right)_{\text{rad}} + \left(\frac{dE}{dx}\right)_{\text{col}}. \tag{4.3}$$

Photons interact with matter via (*i*) photoelectric effect[4] ($E \sim$ keV), (*ii*) Compton scattering[5] ($E \sim$ MeV) and (*iii*) pair-production[6] ($E > 1.022\,\text{MeV}$). Final state electrons interacting with nearby nuclei might emit photons via bremsstrahlung which yet again could undergo pair-production. This cascade of electrons, positrons and photons is known as an *electromagnetic shower*, and is illustrated in figure 4.1. The shower continues until the energy of the pair-produced electrons and positrons drop below the critical energy E_c determined by eq. (4.2).

The average length over which the energy of an electron is reduced by a factor $1/e$ is known as the *radiation length* X_0,

$$X_0 \approx \frac{1}{4\alpha n Z^2 r_e^2 \ln\left(287/Z^{1/2}\right)}, \quad \text{with } r_e = \frac{e^2}{4\pi\epsilon_0 m_e c^2}, \tag{4.4}$$

where r_e is the classical radius of the electron and n is the number density of nuclei. The mean energy $\langle E \rangle$ of the radiated particles in the shower decreases rapidly from the energy E of the initial particle as a function of the number of radiation lengths x, that is

$$\langle E \rangle \approx \frac{E}{2^x}. \tag{4.5}$$

The maximum number of radiation lengths, x_{max}, is reached when $\langle E \rangle \approx E_c$. From eq. (4.5) then,

$$x_{max} = \frac{\ln(E/E_c)}{\ln 2}. \tag{4.6}$$

The critical energy varies from material to material. For example in a high-Z material, such as lead, a 100 GeV shower reaches a maximum length of $x_{max} \sim 13\,X_0$.

4.1.3 Hadronisation

Particles consisting of partons, that is hadrons such as protons and pions, are the colour singlet bound states of quarks/antiquarks which carry zero colour in total. This is a part of the *colour confinement* hypothesis in which only colour singlet states can be observed

[4]When a photon transfers all its energy to a bound electron. In order for momentum to be conserved, any recoil momentum is absorbed by the nucleus.

[5]Scattering of photons on free electrons. Although electrons in matter are bound, they act free if the photon energy is sufficiently high compared to the binding energy.

[6]Occurs when a photon is near a nucleus of charge Z, $\gamma + Z \to Z + e^+ + e^-$. The energy must be higher than 1.022 MeV, the combined rest mass of an electron and positron.

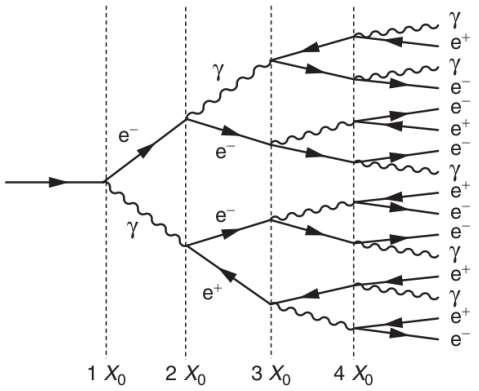

Figure 4.1: Illustration of an electromagnetic shower. An incoming electron radiates a photon at radiation length $1X_0$. At radiation length $2X_0$ the emitted photon undergoes pair production, and the cascade continues until the energy is no longer sufficient for a pair-production, or bremsstrahlung becomes suppressed compared to other processes such as ionization. X_0 is not a fixed length, as the processes which determine X_0, i.e. bremsstrahlung and pair-production, are stochastic processes by nature. Figure taken from Ref. [2], p. 19.

in Nature, putting the restriction on colour wavefunctions, ψ^c, to be anti-symmetric. Due to colour confinement we never observe a free quark or gluon in Nature. Quarks can be indirectly observed within colourless hadrons contained within *jets* formed by *hadronisation*. This process occurs when quarks within bound states begin to separate from one another at high energies. This causes the gluon field between them to reach energies sufficient to create a new $q\bar{q}$-pair, due to the strong field lines narrowing as the quarks continue to separate. An exception to hadronisation is the top quark which decays before hadronisation can occur due to its short lifetime.

4.2 The ATLAS detector

The ATLAS (A Toroidal LHC ApparatuS) detector is a general multi-purpose detector, located at the LHC (Large Hadron Collider), which provides us with the necessary information regarding decay products from colliding pp beams. The ATLAS detector provides nearly full solid-angle coverage around the interaction point (IP) in a collision[7]. Figure 4.2 visualises the four main sub-detectors of ATLAS; (*i*) the inner detector (ID), (*ii*) electromagnetic calorimetry (ECal), (*iii*) hadronic calorimetry (HCal) and (*iv*) the muon spectrometer (MS). These are described in short throughout subsections 4.2.1–4.2.3, which are in large part based on the information provided in Ref. [29]. The

[7]The ATLAS detector operates with cylindrical coordinates. That is, (r, ϕ) used in the transverse plane, with ϕ being the azimuthal angle around the z-axis, and the polar angle θ, often expressed in terms of $\eta = -\ln\tan(\theta/2)$. The z-axis points longitudinally along the beam line, the y-axis points upward in the transverse plane, and the x-axis points toward the center of the LHC ring from the IP.

performance of the detectors are characterised in terms of their momentum and energy resolutions [25] (σ_{p_T}/p_T and σ_E/E respectively)

$$\frac{\sigma_E}{E} = a/\sqrt{E} \oplus b, \qquad \frac{\sigma_{p_T}}{p_T} = cp_T \oplus d, \tag{4.7}$$

where $x \oplus y$ is shorthand notation for $\sqrt{x^2 + y^2}$. a describes stochastic fluctuations in the energy and b the non-uniformity in a medium. The tracking term c takes into account the finite accuracy when measuring deflection angles of particles in a magnetic field, while d takes into account multiple scattering. Table 4.1 shows the energy and momentum resolutions for the different sub-detectors.

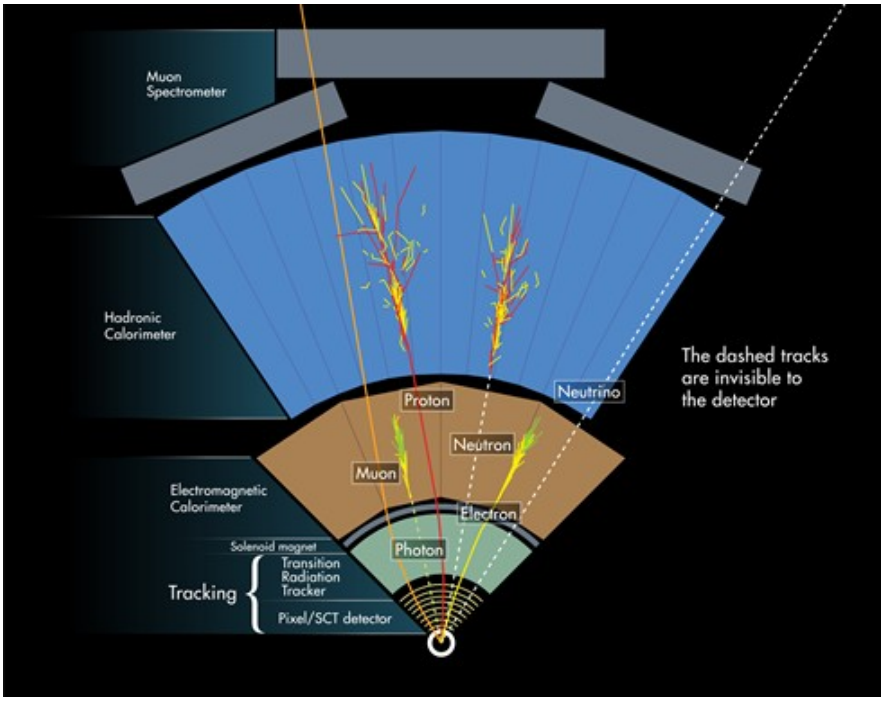

Figure 4.2: Illustration of the ATLAS detector layers, taken from Ref. [32].

Table 4.1: Momentum and energy resolutions for each sub-detector with corresponding pseudo-rapidity coverage η. The units for p_T and E are given in GeV. Values are taken from Ref. [29].

Sub-detector	**Resolution**	η **coverage**
Inner detector	$\sigma_{p_T}/p_T = 0.05\% p_T \oplus 1\%$	± 2.5
EM calorimetry	$\sigma_E/E = 10\%/\sqrt{E} \oplus 0.7\%$	± 3.2
Hadronic calorimetry (jets)	$\sigma_E/E = 50\%/\sqrt{E} \oplus 3\%$ $\sigma_E/E = 100\%/\sqrt{E} \oplus 10\%$	± 3.2 $3.1 < \lvert\eta\rvert < 4.9$
Muon spectrometer	$\sigma_{p_T}/p_T = 10\%$ at $p_T = 1\,\text{TeV}$	± 2.7

4.2.1 Inner detector

Immersed in a 2 T magnetic field and , covering a total region of $|\eta| < 2.5$, the inner detector provides first measurements of the momenta and the identification of particles carrying an electric charge. It is made up of three independent systems; the pixel detector, the semiconductor tracker (SCT) and the transition radiation tracker (TRT). The pixel detector, the innermost part of the ID, consists of silicon-strip electronic modules[8] providing tracking and momentum measurements. The SCT provides precision tracking in which a track passes by eight layers consisting of silicon modules.

The outermost part of the ID, the TRT, provides both tracking and identification of particles with $|\eta| < 2.0$ by the use of multiple straw tubes surrounded by gas contained within either polymer fibres or foils[9]. The fibres/foils act as a boundary between two different media that the relativistic particles pass through, thereby emitting *transition radiation*. The TRT discriminates between electrons and hadrons, such as pions, by the Lorentz factor, $\gamma = \frac{E}{m}$, of the particle. If both particles were to carry the same energy E, a high Lorentz factor would indicate the detection of an electron due to its lower mass m compared to a heavier hadron. This is the same as looking at the ratio p/E. If $p/E \sim 1$ then the mass of the particle must be light, whereas if $p/E \ll 1$ we must be looking at a heavier hadron.

4.2.2 Calorimetry

The ECal is made up of a barrel and two end-cap components. It contains liquid-argon (LAr) electromagnetic (EM) calorimeters which measure the energy deposits of charged particles within a range $|\eta| < 3.2$. It measures the energy deposit of particles in energy clusters and determines the corresponding energy loss.

The emission probability of bremsstrahlung is as mentioned proportional to the inverse mass squared, which was the reason why hadrons primarily lose energy via inelastic collisions and not radiation. For this reason, most hadrons are detected in the HCal. The HCal consists of alternating iron plates and scintillating tiles providing energy measurements of jets.[10] The HCal covers $|\eta| < 1.7$. Combined, the total calorimetry covers $|\eta| < 4.9$.

4.2.3 Muon spectrometer

Any charged particles, such as the minimum-ionising muons, making it past both the ECal and the HCal are measured in the MS. The MS holds a strong magnetic field

[8] As a charged particle moves through one of the modules it ionises the atoms within the silicon strip. The emitted electrons form an electric current which is then read out signalling the position of where the particle passed by.

[9] Charged particles moving through the gas ionise the atoms within. The distance of the liberated electrons to the tubes is determined by the electrons' drift time (at most 40 ns), and one can thereby infer the track of particles moving through the multiple drift tubes.

[10] The scintillating tiles emit light when a charged particle passes through. This light is then converted to an electric current by photo-multiplier tubes, providing information on the total energy deposit of hadrons.

bending the muons, providing optimised muon momentum resolution from the measurements of the sagittae of the track curvatures. It covers $|\eta| < 2.7$, and consists of three main components, each providing magnetic deflection; a barrel ($|\eta| < 1.4$) and two-end cap components ($1.6 < |\eta| < 2.7$) inserted at the end of the barrel. The magnetic bending in the transition region ($1.4 < |\eta| < 1.6$) is provided by both barrel and the end-caps and is lower than in the other pseudorapidity regions. The MS consists of four separate chambers, the first of which is the Monitored Drift Tubes (MDTs) providing precision measurements of track coordinates covering most of the pseudorapidity-range. The Cathode Strip Chambers (CSC) contribute towards larger $|\eta|$ ($2.0 < |\eta| < 2.7$) providing a higher granularity. Furthermore, the gaseous Resistive Plate Chambers (RPCs) situated in the barrel, and Thin Gap Chambers (TGCs) which are used in the end-cap regions, make up the trigger system used to characterise the trigger levels for low- and high-p_T muons.

Muon momentum resolution

From Ref. [33], the muon momentum resolution in the MS is expressed as

$$\frac{\sigma_{p_T}}{p_T} = \frac{p_0^{\mathrm{MS}}}{p_T} \oplus p_1^{\mathrm{MS}} \oplus p_2^{\mathrm{MS}} \cdot p_T, \tag{4.8}$$

where p_0^{MS} is related to the energy loss, p_1^{MS} to multiple scattering[11], and p_2^{MS} to the position resolution. The muon momentum resolution in the ID is expressed as

$$\begin{aligned} \frac{\sigma_{p_T}}{p_T} &= p_1^{\mathrm{ID}} \oplus p_2^{\mathrm{ID}} \cdot p_T, \quad \text{for } |\eta| < 1.9, \\ \frac{\sigma_{p_T}}{p_T} &= p_1^{\mathrm{ID}} \oplus p_2^{\mathrm{ID}} \cdot \frac{p_T}{\tan^2\theta}, \quad \text{for } |\eta| > 1.9, \end{aligned} \tag{4.9}$$

where p_1^{ID} represents multiple scattering, and p_2^{ID} the intrinsic resolution terms. The $\tan^2\theta$-term accounts for curvature measurement when the track length of a muon is reduced, as is the case close to the boundary of the TRT, i.e. $|\eta| \leq 1.9$. From eqs. (4.8) and (4.9) the p_1-term dominates the momentum resolution at low p_T. However, at high p_T it is the p_2-term that will dominate. From table 4.2 we see that the ID provides a better tracking resolution for high-p_T muons with $2.0 < |\eta| < 2.5$. However, for $|\eta| < 2.0$ it is the MS which clearly comes out on top for high-p_T muons.

4.2.4 Triggering system

From 40 MHz data available, that is a bunch crossing occurring every 25 ns, ATLAS has the capability of storing about 1 kHz data. Because of the restricted storage capacity, we need to filter out the events which are worth storing from those that are not. The triggering system is therefore significant in determining the amount of statistics that contain interesting events, and are made available to an analysis. The triggering system

[11] This coefficient is mostly relevant when extrapolating tracks from the MS to the ID.

Table 4.2: Muon momentum resolutions in the ID and MS. A coefficient is denoted N/A if it is not used as a parameter in eqs. (4.8) or (4.9). These values are obtained from Ref. [33].

η region	p_0^{MS} [Tev]	p_1^{MS}[%]	p_2^{MS} [TeV^{-1}]
$\lvert\eta\rvert < 1.05$	0.25 ± 0.01	3.27 ± 0.05	0.168 ± 0.016
$1.05 < \lvert\eta\rvert < 1.7$	0	6.49 ± 0.26	0.336 ± 0.072
$1.7 < \lvert\eta\rvert < 2.0$	0	3.79 ± 0.11	0.196 ± 0.069
$2.0 < \lvert\eta\rvert < 2.5$	0.15 ± 0.01	2.82 ± 0.58	0.469 ± 0.028
η region	p_0^{ID} [Tev]	p_1^{ID}[%]	p_2^{ID} [TeV^{-1}]
$\lvert\eta\rvert < 1.05$	N/A	1.55 ± 0.01	0.417 ± 0.011
$1.05 < \lvert\eta\rvert < 1.7$	N/A	2.55 ± 0.01	0.801 ± 0.567
$1.7 < \lvert\eta\rvert < 2.0$	N/A	3.32 ± 0.02	0.985 ± 0.019
$2.0 < \lvert\eta\rvert < 2.5$	N/A	4.86 ± 0.22	0.069 ± 0.003

consists of a hardware-based first-level trigger (L1) and a software-based high-level trigger (HLT). The L1 trigger is the primary module deciding which events to keep or not, within a time-slot of 25 ns before the next bunch crossing arrives. Events accepted by the L1 trigger is then passed on to the Read-Out System (ROS) and the HLT. The HLT puts additional constraints on the kinematic properties of particles. Events passing both the L1-trigger and the HLT are then passed on to "offline" selections for further analysis.[12]

4.2.5 Object definitions

In the reconstruction of particles in the ATLAS detector there are two parameters proving quite useful to get familiar with:

- d_0: The transverse impact parameter, i.e. the shortest distance from the reconstructed particle to the interaction point in the transverse direction.

- z_0: The longitudinal impact parameter, i.e. the shortest distance from the reconstructed particle to the interaction point along the longitudinal direction (along the beam line).

The particles which originate from the primary vertex are denoted *signal* or *prompt*. Selection cuts are made to distinguish between prompt leptons and uninteresting *background* leptons which may originate from hadrons misidentified as leptons and semileptonic decays of hadrons in the ID[13].

[12] An "online" selection refers to the kinematic constraints put on events during data-taking, and is performed by the triggers. An "offline" selection refers to any further requirements put on the events by a user once data have been stored.

[13] See Section 6.1 for the different types of processes yielding either prompt or non-prompt leptons considered in this thesis.

4.3 Reconstruction and identification of leptons

In the search for new physics in pp collisions, it is essential to reconstruct and identify particles from prompt decays of e.g. weak gauge bosons $W^{\pm}$ and Z, and distinguish them from particles originating from misidentified hadrons, photon conversions, and leptons produced from heavy-flavour decay. The capability of doing so is restricted by the peak luminosity achieved and pile-up (overlapping collisions) in the detector. This necessitates improved reconstruction techniques to achieve higher efficiencies in the identification of leptons. As electrons and muons are treated differently in the detector, due to their differences in mass, they require different reconstruction and identification methods. These methods and their corresponding efficiencies are what will be discussed throughout this section.

4.3.1 Reconstruction

There are three main components contributing to an electron's reconstruction; (*i*) localized cluster energy deposits in the ECal, (*ii*) tracks in the ID and (*iii*) close matching of the cluster and the track in (η, ϕ)-space [30]. The reconstruction of an electron track is based on hits in the ID tracking layers, and is defined according to the distance $\Delta R = \sqrt{(\Delta\eta)^2 + (\Delta\phi)^2}$ in (η, ϕ)-space from other reconstructed tracks, and whether it is associated to a cluster in the ECal. As the electron traverses the layers of the ECal it deposits energy in the calorimeter cells. The energy within each cell is then summed to a total deposited energy within a cluster using the *sliding-window* seed-cluster algorithm [34] and calibrated to account for energy deposited outside the cluster. The sliding-window algorithm provides a high efficiency, $\varepsilon_{\text{clus}}$, in reconstructing electron clusters, with $\varepsilon_{\text{clus}} = 65$–$96\%$ for $E_T = 4.5$–$7\,\text{GeV}$ and $\varepsilon_{\text{clus}} \sim 99\%$ for $E_T > 15\,\text{GeV}$ [30]. If the measurements show at least four hits in the silicon layers with no indication of stemming from a photon conversion vertex, the charged particle is considered an electron candidate if it is associated to a cluster.

Muons require a different approach as they are minimum-ionising in the calorimetry. Their reconstruction is performed independently in the ID, where muons are treated in the same manner as any other charged particle, and the MS [31]. There exists four classifications of a muon; *combined*[14] (CB), *segment-tagged*[15] (ST), *calorimeter-tagged*[16] (CT), and *extrapolated*[17] (ME). CB track reconstruction yields the highest accuracy for high-p_T muons, followed by ME muons. As the ID only covers $|\eta| < 2.5$, any muons reconstructed at $|\eta| \geq 2.5$ are extrapolated muons.

[14] A combined track of reconstructed tracks in the ID and the MS is made using a global refit.

[15] When a track reconstructed in the ID is associated with at least one hit in the (MDT) or CSC in the MS. Used for low p_T muons, which cross only one layer in the MS.

[16] When a track in the ID is associated with a minimum-ionising charged particle in the calorimeters.

[17] Also known as stand-alone muons, extrapolated muons have the requirement of traversing at least two layers in the MS. The muon track is then reconstructed using only hits in the MS.

4.3.2 Identification

Electrons

The selection of prompt electrons in the region $|\eta| < 2.47$ is based on the likelihood L_S for signal and L_B for background,

$$L_{S(B)}(\mathbf{x}) = \prod_{i=1}^{n} P_{S(B),i}(x_i) \tag{4.10}$$

where the vector $\mathbf{x}$ contains the n discriminating variables (DV) used in the electron identification, such as E/p and shower profile variables (see Ref. [30] for further details). $P_{S(B)}(x_i)$ is the signal (background) probability density for an electron candidate at point x_i for DV i. Here, the signal corresponds to prompt electrons originating from the interaction point (primary vertex), while the background is made up of non-prompt electrons, such as jets displaying similar signatures like prompt electrons, electrons produced in pair production from photons passing the detector material and decay of heavy flavour hadrons. In addition, there exists a discriminant d_L for each electron candidate,

$$d_L = \frac{L_S}{L_S + L_B} \sim \begin{cases} 1, \text{ signal electron} \\ 0, \text{ background electron} \end{cases},$$

and a transformed discriminant d'_L, written as the inverse sigmoid function of d_L,

$$d'_L = -\tau^{-1} \ln\left(d_L^{-1} - 1\right) \tag{4.11}$$

where $\tau = 15$. The transformed discriminant gives a range of values which can be used to define four operating points. If an electron candidate within the working point has a value larger than d'_L it is considered a prompt electron, otherwise non-prompt. The four operating points, in increasing order of background rejection, are

- *VeryLoose*: Requires only one hit in the pixel detector, and is thus most relevant for background studies.
- *Loose*: Requires a combination of seven hits total from the pixel and silicon-strip detectors, two of which must stem from the pixel detector.
- *Medium*: Same selection criteria as for *Loose*, but one of the seven hits must also occur in the innermost pixel layer reducing background from photon conversions.
- *Tight*: Same selection criteria as *Medium* but tighter requirements on the DVs.

The corresponding identification efficiencies are summarised in table 4.3. Each working point is a subset of working points with a lower background rejection, i.e. *Tight*$\subset$ *Medium* $\subset$ *Loose* $\subset$ *VeryLoose*.

One can find the electric charge of an electron using its track curvature. However, there still exists a chance of misidentifying electron charges, either due to a mismatch

Table 4.3: Identification efficiencies (ε_{id}) for each identification working point in the electron [30] and muon channel [31]. The electron efficiencies are given for the threshold $E_T = 40\,\text{GeV}$ (100 GeV), while the muon efficiencies are quoted using $5 < p_T < 20\,\text{GeV}$ ($p_T > 100\,\text{GeV}$).

	Loose[%]	*Medium*[%]	*Tight*[%]	*High-p_T*[%]
Electron	93(96)	88(94)	80(90)	–
Muon	98(98)	97(97)	90(93)	79(80)

of the reconstructed track to an electron candidate, or inaccurate measurements of the track curvature. High-energy electrons lose energy by bremsstrahlung. If the photon emitted undergoes photon-conversion, $\gamma \to e^- e^+$, then three tracks are now associated to the primary electron, two of which with the correct charge, thereby making it harder to identify the correct charge of the primary track. Charge misidentification may also occur when the curvature of the tracks is ill-defined, which is most probable for high pseudorapidities. In ATLAS, charge misidentification and a mismatch of track to the primary electron is most probable in the pseudorapidity-region $1.5 < |\eta| < 2.2$ [30].

Muons

There are also four main categories to identify muons, each with a subset of requirements tailored for specific physics analyses and each yielding different efficiencies in the low-p_T region ($5 < p_T < 20\,\text{GeV}$) and the high-p_T region ($p_T > 100\,\text{GeV}$). These efficiencies are summarised in table 4.3.

- *Loose*: Maximises reconstruction efficiency. All muon types are used, although the majority of muon candidates are CB muons for $|\eta| < 2.5$.
- *Medium*: Includes same selection criteria as for the loose selection, but with the aim of minimising systematic uncertainties. Only CB and ME muons are used in the selection.
- *Tight*: Maximises purity of muons at the expense of lower efficiency. Only CB muons are considered.
- *High-p_T*: Ideal for searches at higher resonant masses, with the aim of maximising the momentum resolution for $p_T > 100\text{GeV}$, but at the expense of identification efficiency. By requiring at least three hits in three precision layers of the MS thereby, decreasing the reconstruction efficiency by $\sim 20\%$, the momentum resolution increases by about 30% for muons with $p_T > 1.5\text{TeV}$.

4.3.3 Isolation

In physics searches it is highly desirable to separate between prompt electrons, muons and photons in signal processes from those originating from background processes such

as misidentified hadrons and photon conversions in the detector material. A prompt lepton could be surrounded by a lot of activity, especially if it is in near vicinity of a jet. By checking if the lepton is isolated we can distinguish between the non-prompt leptons, occurring from the inside of a jet, and prompt leptons.

The isolation of a particle can be divided into two categories; calorimeter-based and track-based isolation. Calorimeter-based isolation looks at the sum of transverse energies in an area $\Delta R < X$, with X being an arbitrary distance, around a candidate. Variables used in track-based isolation aim to select tracks which originated from the interaction point. Among multiple vertices, it is the vertex which displays the greatest sum of transverse momenta squared that can be considered the primary vertex. Track-based isolation variables thereby look at the sum of p_T within a cone of radius ΔR around a candidate. For electrons we have three isolation categories; *Loose*,[18], *Gradient*[19] and *Fix*[20]. The criteria imposed on the discriminating variables $p_T^{\text{varcone30}}$ (scalar sum of transverse momenta around the candidate within $\Delta R = \min(10\text{GeV}/p_T^{\mu}, 0.3)$ and $E_T^{\text{topcone20}}$ (sum of transverse energy around the candidate within $\Delta R = 0.2$) define the seven operating points used for muons. The cone size in the track-based isolation variable is dependent on the lepton candidate's transverse momentum in order to improve the performance for muons originating from the decay of high-p_T particles.

4.4 Systematic uncertainties

Errors which do not happen at random, but which can be replicated upon repetition of an experiment, and propagating throughout the results, are known as *systematic* errors. Such uncertainties may arise from external factors, like poor knowledge of the detector acceptance or trigger efficiencies, and has the potential to cloud one's judgement when performing an analysis. That is, systematic effects lead to a larger overlap between the null and alternative hypotheses, giving a larger probability that potential new physics is overlooked and disregarded as being expected from the background, or worse: a false discovery of new physics is made. How to include such systematics in the calculation of the probability is further detailed in Chapter 5. The general definition, from Ref. [35], of systematic uncertainties is

> "Systematic uncertainties are measurement errors which are not due to statistical fluctuations in real or simulated data samples."

An accounting of such errors is crucial in order to gain an accurate picture of a dataset, before any statistical inference is made. The treatment of the systematics depends on whether or not there exists potential correlations between sources i and j, in which the correlation is represented by the coefficient ρ_{ij}. Assuming the systematic errors to be

[18] Aims at a fixed value of the isolation efficiency, ε_{iso}, uniform in E_T and η.
[19] Aims at a fixed value of the isolation efficiency uniform in η but dependent on E_T.
[20] Fixed requirements on value of the isolation variable.

independent of one another, the total uncertainty from n systematic errors is

$$\sigma_{\text{tot}}^2 = \sigma_1^2 + \sigma_2^2 + \ldots + \sigma_n^2 = \sum_{i=1}^{n} \sigma_i^2. \tag{4.12}$$

If there however does exist a correlation between sources i and j then

$$\sigma_{\text{tot}}^2 = \sigma_1^2 + \sigma_2^2 + \ldots + 2\rho_{12}\sigma_1\sigma_2 + \ldots = \sum_{i=1}^{n} \sigma_i^2 + 2 \sum_{\substack{i,j=1 \\ i<j}}^{n} \rho_{ij}\sigma_i\sigma_j. \tag{4.13}$$

Systematic uncertainties is divided into two categories; experimental and theoretical systematics.

4.4.1 Experimental systematics

Experimental systematics are related to errors originating from modelling of the measurement apparatus itself. Examples are poor knowledge of detector resolutions and uncertainties related to the reconstruction, isolation and identification efficiencies.

For an electron, uncertainties are calculated by varying for example the mass window around the Z-boson peak or the identification criteria for tag electrons. Methods for estimating the systematic uncertainties related to electron efficiencies are described in further detail in Ref. [30]. In this analysis we include a nuisance parameter for the energy resolution measured in the calorimeters. Additional nuisance parameters arise for instance from uncertainties related to the energy scale, the identification of an electron in the ID and calorimeters, and the estimation of misidentified electrons[21].

For a muon, the calculation of efficiency uncertainties follow the methodology described in Ref. [31]. A nuisance parameter describing the uncertainty of a *bad muon*[22] veto is applied. The momentum is measured in the ID and MS, and thus uncertainties related to these two sub-detectors should also be taken into account. Additionally, the muon momentum resolution can be affected by a *sagitta bias*[23], that is a bias occurring due to the rotation of detector layers.

4.4.2 Theoretical systematics

Theoretical systematics can arise from the estimation of parameters used in the Standard Model. An example being the experimental estimation of the strong coupling parameter α_s. Furthermore, parton distribution functions include non-perturbative parameters and depend on α_s. The contribution of uncertainties related to PDFs are estimated from PDF-scale and eigenvector variations. Any applications of theoretical

[21] See Section 6.5

[22] Muons with poorly reconstructed momentum. The definition of good muons is based on the quantity $\sigma(q/p)/|q/p|$, where q is the muon charge and p the momentum. The bad muon veto is dependent on η and p_T [36].

[23] A sagitta is the distance from the center of a circular arc to the center of a line between the two ends of the corresponding arc. The smaller the sagitta, the greater the particle momentum is.

uncertainties will in this analysis be done for the Drell-Yan background as this is the most dominating background in the dilepton channel. The nuisance parameters for the theoretical uncertainties also include photon-induced (PI) corrections and electroweak (EW) corrections.

4.5 Summary

In this chapter we have taken a look at how particles interact with matter depending on their sizes and which forces they abide by. We have taken a look at the ATLAS multi-purpose detector, and how each sub-detector is dedicated to the optimisation of either the energy or tracking resolutions, and the minimisation of possible systematic uncertainty sources which could affect our measurements. Furthermore, we have reviewed the identification and detection techniques used when identifying prompt leptons from background leptons. Once data have been gathered from a detector, we must know how to extract and interpret the information they hold. The next chapter provides us with some of the tools allowing us to do exactly so.

Chapter 5

Statistical Inference

In particle physics, experiments are restricted by the stochastic nature of particles. As we cannot predict an outcome with absolute certainty, we ascribe probabilities for certain outcomes to occur. When assigning probabilities related to interactions taking place within particle collisions the outcomes, although difficult to reconstruct[1], are already known and accounted for by prior knowledge provided by a theory. The greater complexity of particle collisions is assigning the cause for the observed outcome. E.g. if there is a deviation between experimental observations and our prior knowledge, does that indicate our theory to be flawed, and if so could it bring to light new physics? We will use Refs. [35] and [37] to find the tools in answering such questions.

5.1 Statistical framework

Within a high energy physics experiment the quantity of interest is the presence of a new physics signal, provided by the observed number of events in an experiment. A reconstructed particle in the detector has a certain probability of passing a given set of selection criteria. The more stringent the criteria, the smaller the probability. The cut-and-count procedure entails a binomial, discrete distribution for a given mass range, based on the recording of stochastic events from an arbitrary mass bin l. As the number of bunch crossings increases, the number of events within a mass bin can be approximated by a Poisson distribution. The Poisson probability mass function (pmf) gives the probability of observing n events within a mass bin l for a given channel k, given the expected number of events ν_{kl} prior to any data-taking,

$$P(n|\nu_{kl}) = e^{-\nu_{kl}} \frac{\nu_{kl}^n}{n!}. \tag{5.1}$$

The value of ν_{kl} is estimated from either the *null hypothesis* (H_0), which in this analysis is any process associated with the Standard Model, or the *alternative hypothesis* (H_1), which is taken to be any Beyond Standard Model process plus background. The

[1] As was discussed in the previous chapter.

expected number of events is dependent on the number of background, b_{kl}, and signal, s_{kl}, events within a mass bin, that is

$$\nu_{kl}(\sigma, \boldsymbol{\theta}) = \begin{cases} b_{kl}(\boldsymbol{\theta}), & (H_0) \\ s_{kl}(\sigma, \boldsymbol{\theta}) + b_{kl}(\boldsymbol{\theta}), & (H_1) \end{cases} \tag{5.2}$$

where the parameter of interest σ is the cross-section for the production of a G^* decaying to dielectrons or dimuons, and $\boldsymbol{\theta}$ is an array of nuisance parameters taken to be any systematic uncertainties associated with the experiment and theoretical calculations[2]. Explicitly, the number of expected signal events in bin l for channel k, subject to N_{sys} nuisance parameters, under the H_1 hypothesis is expressed as[3]

$$s_{kl}(\sigma, \boldsymbol{\theta}) = \overline{s_{kl}}(\sigma) \left(1 + \sum_{i=1}^{N_{\text{sys}}} \theta_i \frac{(\delta s_{kl})_i}{\overline{s_{kl}}} \right), \quad \overline{s_{kl}} = L_{\text{int}} \sigma A_k \varepsilon_{kl} \tag{5.3}$$

with an integrated luminosity L_{int}. The variable A_k, referred to as "acceptance×efficiency", is the ratio of number signal events passing a given selection criteria over the initial number of signal events produced, while ε_{kl} is the fraction of events within the signal invariant mass histogram that goes into bin l. The term $(\delta s_{kl})_i/\overline{s_{kl}}$ takes into account any possible shift in s_{kl} due to a nuisance parameter θ_i. Likewise, the number of background events b_{kl} in bin l for channel k is expressed as

$$b_{kl}(\boldsymbol{\theta}) = \overline{b_{kl}} \left(1 + \sum_{i=1}^{N_{\text{sys}}} \theta_i \frac{(\delta b_{kl})_i}{\overline{b_{kl}}} \right), \tag{5.4}$$

where $\overline{b_{kl}}(\boldsymbol{\theta})$ is the central value extracted from Monte Carlo simulations, and $(\delta b_{kl})_i/\overline{b_{kl}}$ is the variation in the number of background events due to any systematic uncertainties represented by θ_i.

The likelihood

$$\mathcal{L}(\sigma, \boldsymbol{\theta}) = P(\mathbf{n}|\sigma, \boldsymbol{\theta}) = \prod_{k=1}^{N_{\text{chan}}} \prod_{l=1}^{N_{\text{bin}}} \frac{\nu_{kl}(\sigma, \boldsymbol{\theta}) e^{-\nu_{kl}(\sigma, \boldsymbol{\theta})}}{n_{kl}!} \tag{5.5}$$

is a product of the probability distribution function (pdf) relevant for this analysis (5.1) over N_{chan} number channels[4] and N_{bin} number bins. $\mathbf{n}$ represents a set of the n_{kl} observations within bin l given channel k.

[2] See Section 6.7 for the relevant nuisance parameters applied in this analysis.

[3] When the nuisance parameters are modelled with a Gaussian prior distribution, then $s_{kl}(\sigma, \boldsymbol{\theta})$ is described by a log-normal distribution. The log-normal distribution confines the signal distribution to its allowed range $[0, \infty)$, and additionally provides a mathematically consistent limit setting when signal systematics are included in the posterior. The exact expression for the log-normal function is expressed in eq. (5.3) from [37].

[4] N_{chan} is equal to 1 when analyzing the dielectron or dimuon channels separately, and 2 when analyzing the dilepton channel.

5.1.1 Discovery statistics

When interested in the significance of a deviation between observed data and a hypothesis, we can use the p-value prescription from *frequentist* statistics [35]. The p-value tells us the probability of observing the same number of data events, or more, in an experiment *given* the null-hypothesis to be true. The smaller the p-value is, the closer we are to rejecting the H_0-hypothesis. The probability

$$p_i = \int_{t_{obs}}^{+\infty} g(t|H_i)dt, \quad i = 0 \text{ or } 1, \tag{5.6}$$

to observe test-statistic values[5], t_{obs}, greater than or equal to the one observed, given either H_0, also referred to as the *background-only* hypothesis, or H_1, referred to as the *signal-plus-background* hypothesis, to be true. The p-value is expressed as the area under the Poisson pdf, $g(t|H_i)$, where $t > t_{obs}$,

The p-value is related to the *significance level* of a hypothesis via the inverse of the cumulative distribution function of the unit Gaussian, Φ^{-1}, that is

$$p = \int_{Z}^{+\infty} \frac{e^{-t^2/2}}{\sqrt{2\pi}} dt \implies Z = \Phi^{-1}(1-p). \tag{5.7}$$

A discovery within particle physics is claimed if the observed significance is $Z \geq 5\sigma$, i.e. $p \leq 2.87 \cdot 10^{-7}$, such that the probability of claiming a discovery if the background hypothesis is true is $2.87 \cdot 10^{-7}$.

5.1.2 Exclusion limits

By the use of frequentist inference we can calculate the probability for some observed data under a given hypothesis. By the use of *Bayesian* inference the quantity of interest is the probability for the hypothesis to be true given the data, as expressed by *Bayes' theorem*,

$$P(X|Y,I) = \frac{P(Y|X,I)P(X|I)}{P(Y|I)}. \tag{5.8}$$

The probability of our hypothesis X being true given the data Y is expressed by the term $P(X|Y,I)$ also known as the *posterior*. The posterior is dependent on our *degree-of-belief*, $P(X|I)$, or rather our prior knowledge about the system based on any background information I available to us. This degree-of-belief is based on results from previous experiments and is modified the more experiments we perform by the *likelihood*, $P(Y|X,I)$, of the data given our hypothesis to be true. $P(Y|I)$ is the probability

[5]These are often taken to be either the number of observed events counted or the log-likelihood ratio.

for the observed data and acts as a normalisation constant. Explicitly, eq. (5.8) can be written as

$$P(\sigma, \boldsymbol{\theta}|\mathbf{n}) = \frac{\mathcal{L}(\sigma, \boldsymbol{\theta}) P_0(\sigma, \boldsymbol{\theta})}{P(\mathbf{n})}, \tag{5.9}$$

where $\mathbf{n}$ is a set containing the number of observed events in all bins for an experiment, σ is the parameter of interest and $\boldsymbol{\theta}$ represents N_{sys} nuisance parameters. The likelihood is represented as $\mathcal{L}(\sigma, \boldsymbol{\theta})$. The sub-index on P_0 denotes our prior knowledge of the system, where $P_0(\sigma, \boldsymbol{\theta})$ is expressed as

$$P_0(\sigma, \boldsymbol{\theta}) = P_0(\sigma) \prod_{i=1}^{N_{\text{sys}}} \phi(\theta_i), \tag{5.10}$$

with a standard normal prior pdf ϕ for the nuisance parameters and the cross-section prior $P_0(\sigma)$ which is taken to be flat. The probability for a hypothesis to be true given the observed data is then expressed by a marginalisation integral

$$P(\sigma|\mathbf{n}) = \int P(\sigma, \boldsymbol{\theta}|\mathbf{n}) d\boldsymbol{\theta} = N \int \prod_{k=1}^{N_{\text{chan}}} \prod_{l=1}^{N_{\text{bin}}} \frac{\nu_{kl}(\sigma, \boldsymbol{\theta})^{n_{kl}} e^{-\nu_{kl}(\sigma, \boldsymbol{\theta})}}{n_{kl}!} \prod_{i=1}^{N_{\text{sys}}} \phi(\theta_i) d\boldsymbol{\theta}, \tag{5.11}$$

where N is a normalisation constant determined by

$$\int_0^\infty P(\sigma|\mathbf{n}) d\sigma = 1.$$

We can express the upper limit on the signal cross-section, σ_{up}, within a certain credibility level (CL) $1 - \delta$, such that any signal models containing a σ exceeding this limit is excluded. This is expressed as

$$\int_{\sigma_{\text{up}}}^\infty P(\sigma|\mathbf{n}) d\sigma = \delta, \tag{5.12}$$

where δ is usually taken to be 0.05 such that we obtain a CL of 95%.

5.1.3 Covariance and correlation

The covariance $\text{cov}[x_1, x_2]$ relates two random variables, x_1 and x_2, by their joint variation[6]. The covariance between n variables is expressed in terms of a covariance matrix V,

$$V_{ij} = \text{cov}[x_i, x_j] = E[x_i x_j] - E[x_i]E[x_j], \quad \rho_{ij} = \frac{V_{ij}}{\sigma_i \sigma_j}, \tag{5.13}$$

[6]I.e. how much the variation of one variable affects the variation of another. If $\text{cov}[x_1, x_2] > 0$ the increase in variations of one parameter increases the variations of the other. If $\text{cov}[x_1, x_2] < 0$ the increase in variations of one parameter decreases the variations of the other. If $\text{cov}[x_1, x_2] = 0$ the variables do not affect each other in any way.

where $E[x_i]$ is the mean of variable x_i and σ_i is the variance of x_i. ρ is the dimensionless variable of the covariance and varies between 0 and 1, with 0 being no correlation, and 1 being completely correlated.

5.2 Markov Chain Monte Carlo

The computation of the marginalisation integral in eq. (5.11) can quickly become quite intricate and tedious to perform when dealing with a large number of nuisance parameters. However, the integration can be achieved numerically by the use of *Markov Chain Monte Carlo*[7] (MCMC). By using a Monte Carlo method we can grow a Markov Chain containing values of the posterior, such that any new knowledge of a system $P_i(\sigma, \boldsymbol{\theta})$ is dependent on our previous knowledge of the system $P_{i-1}(\sigma, \boldsymbol{\theta})$ after performing an experiment. We will in this analysis use the *Bayesian Analysis Toolkit*[8] (BAT) [38] to produce the MCMC and extract exclusion limits on the mass of G^* for each coupling strength, along with the 68% and 95% quantiles. It does so by using the simple MCMC method of Metropolis sampling [39][9].

5.2.1 Metropolis method

By not assigning a specific distribution to the posterior, we let the posterior probability distribution be governed by the likelihood and a prior. By proposing a new state $P(\sigma^*, \boldsymbol{\theta}^*)$, with σ^* drawn from a uniform prior and $\boldsymbol{\theta}^*$ drawn from Gaussian proposal distributions, we can calculate a probability ratio r of accepting the move to a new state based on the previous posterior, that is

$$r = \frac{P(\sigma^*, \boldsymbol{\theta}^*|\mathbf{n})}{P_{i-1}(\sigma, \boldsymbol{\theta}|\mathbf{n})} = \frac{\mathcal{L}(\sigma^*, \boldsymbol{\theta}^*)P_0(\sigma^*, \boldsymbol{\theta}^*)}{\mathcal{L}(\sigma, \boldsymbol{\theta})P_0(\sigma, \boldsymbol{\theta})}. \tag{5.14}$$

If $r \geq 1$ we accept the new state. If however the previous posterior probability is greater than the one proposed we treat the ratio as an *acceptance probability*. By comparing r to a random number U, generated between $[0, 1]$ from a uniform distribution, there is a certain probability of rejecting the new state ($r < U$) or accepting the new state ($r \geq U$). A chart of the workflow for the Metropolis algorithm is seen in figure 5.1.

5.3 Summary

We can gain important insight in a dataset by the use of statistical inference. Using discovery statistics we can find the probability for some observed data given a hypothesis to be true, P(data|theory), while Bayesian analysis allows us to test the probability for

[7] Monte Carlo refers to methods used when generating random numbers. A Markov Chain is a sequence of numbers in which any number is dependent on the number prior to it in the sequence.

[8] BAT is a program centered around Bayes' theorem. It is implemented in C++ and interfaced with ROOT.

[9] To be more precise, it uses the Metropolis-Hastings algorithm (i.e. importance sampling), but the principle remains the same.

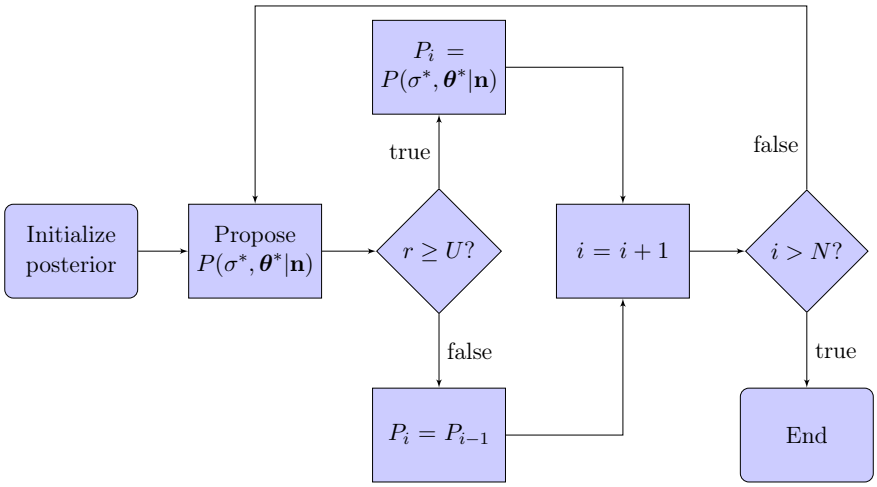

Figure 5.1: Workflow of the standard Metropolis algorithm. N is the total number of iterations used in the generation of the Markov Chain, r the ratio of the proposed posterior $P(\sigma^*, \boldsymbol{\theta}^*|\mathbf{n})$ over the previous accepted posterior $P_{i-1}(\sigma, \boldsymbol{\theta}|\mathbf{n})$ and U is a random number generated from a uniform distribution.

a hypothesis to be true given some observed data, $P(\text{theory}|\text{data})$. In this thesis we will make use of Bayesian analysis to set exclusion limits on the mass of G^*.

Part III

Analysis

Chapter 6

Analysis Procedure

Observed data, being the blueprint of Nature, is what we aspire to describe. Monte Carlo points us in the direction of where to look. The observed data in this analysis is based on data from pp collisions collected at the LHC during Run 2 (2015-2018) at $\sqrt{s} = 13\,\text{TeV}$. The total integrated luminosity is $139\,\text{fb}^{-1}$, a combination of three different subperiods, labelled a (2015–2016), d (2017) and e (2018), each with an integrated luminosity of $36.2\,\text{fb}^{-1}$, $44.3\,\text{fb}^{-1}$ and $58.5\,\text{fb}^{-1}$, respectively. The Monte Carlo simulations are of Standard Model background processes. Additionally, the simulation process of the RS signals of G^* is modelled and compared with the background hypothesis (SM) and the observed data using statistical analysis.

6.1 Standard Model background

As we are simulating signals of the type $q\bar{q} \to G^* \to l^+l^-$ in pp collisions, we must consider any possible contribution of SM processes which could also produce dileptons in the final state. Any such background should be accounted for in order to gain an accurate picture when comparing the observed data to that which can be accounted for by the background, before performing any statistical inference.

6.1.1 Prompt leptons

Dibosons

A Standard Model process which produces either two Z/W bosons or a W and a Z boson in the final state is known as a *diboson* process (ZZ, WZ, WW). A Z^0 can decay leptonically to l^+ and l^-, whereas a $W^\pm$ can decay as $W^- \to l^-\bar{\nu}_l$ and $W^+ \to l^+\nu_l$. Thus, a diboson process may contribute to both same-sign and opposite-sign dilepton pairs in the final state. An overview of the Feynman diagrams describing such processes is seen in figure 6.1.

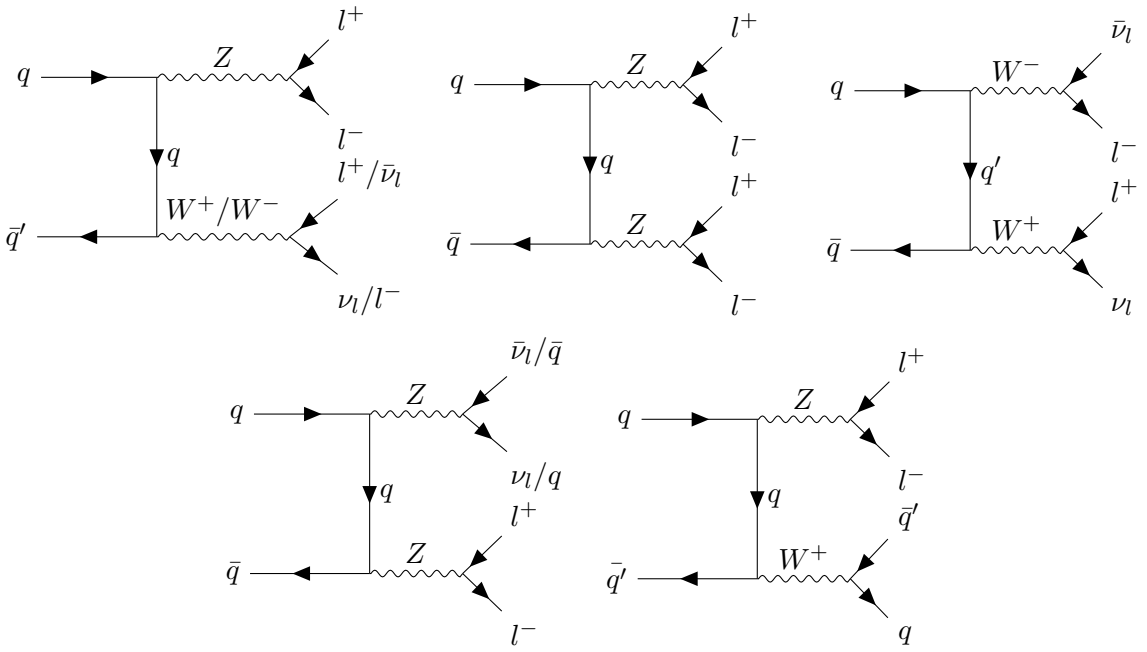

Figure 6.1: Feynman diagrams of diboson processes included in the SM background with dilepton pairs in the final state.

Top processes

Another significant background to take into consideration involving leptons is top processes. The top quark, carrying a mass of 173 GeV [40], is heavier than the W-boson and is the only quark which can be indirectly studied in isolation through its decay, with the most dominating process being $t \to bW^+$, as no hadronisation has time to occur due to its short lifetime. The W bosons may in turn decay to either quarks or leptons in the final state, $W^+ \to q\bar{q}', \nu_l l^+$, which in turn means that the final state of a $t\bar{t}$ collision contain contain either exclusively jets of hadrons, lepton+jets or dileptons. In addition, there are processes which result in the production of a single top-quark accompanied by a W-boson, thereby potentially giving two leptons in the final state. Examples of $t\bar{t}$ and single-top processes are seen in figure 6.2, and the decay scheme of top quarks in figure 6.3.

Drell-Yan

The annihilation of a quark-antiquark pair to a lepton-antilepton pair via the production of either a virtual photon or Z is known as a Drell-Yan (DY) process, schematically shown as a Feynman diagram at tree-level in figure 6.4. This process constitutes one of the biggest backgrounds in the dilepton channel, as we will see in this analysis.

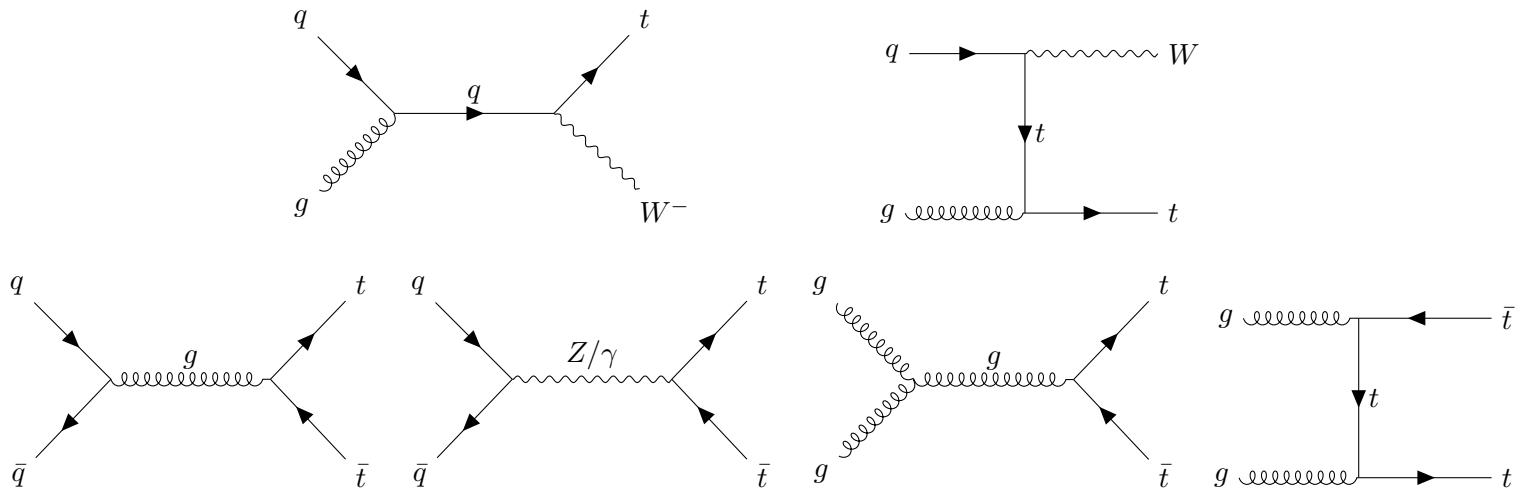

Figure 6.2: Feynman diagrams of a $t\bar{t}$ process (bottom) and single-top production (top). The decay of the final state top quarks is shown in figure 6.3.

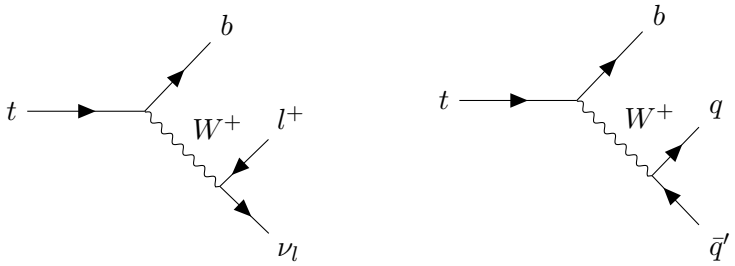

Figure 6.3: Decay scheme of a top quark into b and W^+, leading to a final state containing a b-quark accompanied by either a lepton and a neutrino or two quarks. For an anti-top quark the leptonic decay would consist of a $\bar{b}$ and $W^- \to \bar{\nu}_l l^-/\bar{q}'q$.

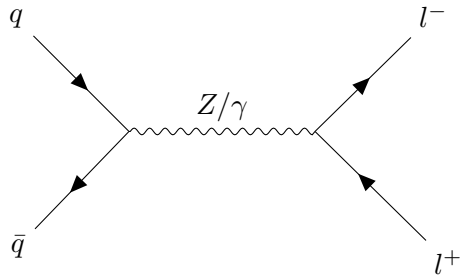

Figure 6.4: With time moving from left to right, this Feynman diagram describes the s-channel Drell-Yan process $q\bar{q} \to Z/\gamma \to l^+l^-$ to first order.

6.1.2 Fakes

"Fakes" is a collective term describing two categories of leptons; (*i*) leptons considered to be "real" but not of the kind we are interested in, i.e. non-prompt leptons, and (*ii*) mis-identified leptons, i.e. reconstructed particles which are not physically present in the detector. In essence, fakes describe any reconstructed lepton not occurring from a prompt dileptonic background process.

In the first category, non-prompt leptons are typically leptons originating from other sources than the decay of Z and W bosons, with the exception of the top quark decay to a W which in turn decays leptonically. The non-prompt leptons are very much real, but the term "fake" is used when the non-prompt leptons "mimic" the signal of prompt isolated leptons. These fake leptons can occur from decays of hadrons within jets, or the decay of c- and b-quarks before they hadronise. An additional source of non-prompt leptons are those occurring from photon conversions. An electron, or much less probable a muon, can radiate a photon which in turn pair-produces an e^+e^--pair[1]. If one of the pair-produced leptons is combined with an otherwise single-lepton process, e.g. from a semi-leptonic W-decay, then it could pass as a dilepton event. Additionally, compared to a prompt DY process, pair-production processes could also result in same-sign (SS) lepton pairs [41]. These fake leptons are an important contribution to the SS background. Prompt leptons are expected to be isolated, as they do not originate from within a jet. The use of isolation criteria helps us in better separating the prompt from the non-prompt leptons. In some cases, however, non-prompt leptons can "sneak" past the isolation selection criteria, and must be taken into account in the analysis.

Leptons in the second category are referred to as "true fake" leptons, and we will here separate between the sources of true fake electrons and true fake muons. Because both photons and electrons deposit their energy in the ECal, a photon can be mis-identified as an electron if it by chance is matched to the track of a charged particle. There are two sources of such a mis-identification – the first being hadronic jets and the second being high-energy muons. If a photon is created in the jet before hitting the ECal, and happens to be closely accompanied by a charged hadron, then the combination of the deposited energy in the calorimeter and the hadron track in the ID could mimic the signal of an electron. Similarly, high-energy muons emitting a photon (due to bremsstrahlung) in the ID, leave behind energy deposits in the ECal similar to an electron. If a high-energetic hadron makes it across the HCal to the MS, leaving behind a track both in the ID and the MS, it could in principle be falsely identified as a muon. However, most muons originating from jet activity are real muons.

An example of a process which leads to a dilepton final state with one true fake lepton is W+jets, seen in figure 6.5. If the W-boson decays leptonically, $W^- \to \bar{\nu}_l l^-$, and a jet was mis-identified as a lepton, the observed final state would be a dilepton pair. Additionally, single top and other QCD processes can also contribute to the fake background, as a fake lepton can be reconstructed from the decay of a quark alongside a real lepton. Figure 6.3 shows an example of the top-quark decay $t \to bW^+$. If the

[1]The pair-production of a $\mu^+\mu^-$-pair can also occur, but the probability for this conversion is much less likely to occur due to the higher muon mass.

W^+ decays leptonically and the jet is mis-identified as a lepton, then the end result would be a dilepton pair. The estimation of fakes present in a dataset is determined by a data-driven technique, elaborated on in Section 6.5.

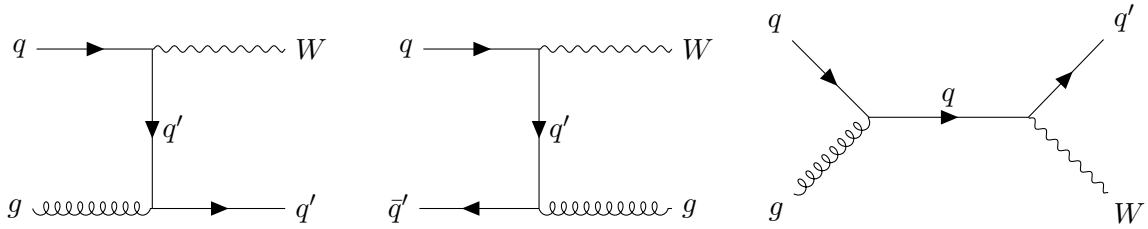

Figure 6.5: t-channel and s-channel Feynman diagrams of W+jets processes to first order. The leptonic decay of the W-boson and the mis-identification of the accompanying jet (q) as a lepton could pass the selection criteria disguised as a dilepton pair.

6.2 Simulation process

The modelling of Standard Model backgrounds and signal samples are done using Monte Carlo (MC) event generators. The events in each MC sample undergoes a reweighting in order to simulate the background processes as close as possible to observed data collected in the ATLAS detector (see subsection 6.2.3). Examples of reweightings are the lepton and trigger efficiency scale factor, cross-section weight and pile-up weight.

6.2.1 Background estimation

The dominating background contribution is the Drell-Yan background, generated at next-to-leading order (NLO) using the POWHEG generator [42] used alongside PYTHIA 8 [43] for the modelling of parton showering and hadronisation. Any DY processes giving a tau pair in the final state are simulated using the SHERPA 2.2.1 generator [44]. The second highest contributing background process is the production of dileptons from top-quark processes simulated using POWHEG and PYTHIA 8. Furthermore, diboson processes (WW, WZ, ZZ) were simulated using both SHERPA 2.2.1 and SHERPA 2.2.2. A summary of the generators used for each process and order in the PDFs are given in table 6.1. Passage of MC generated particles from background and signal processes traversing matter in the ATLAS detector were simulated using GEANT4 [45].

6.2.2 Signal samples

The signal samples of the lightest Kaluza-Klein graviton mode G^*, i.e. the first graviton excitation, were generated using PYTHIA 8 to leading order (LO) in the Feynman diagrams. In the RS model there are two free parameters, (i) the mass of the graviton excitation and (ii) the coupling strength $k/\overline{M}_{Pl}$ of the graviton to SM particles, where k is the warp factor, as mentioned in subsection 2.2.3, and $\overline{M}_{Pl}$ is the reduced Planck

Table 6.1: Summary of the MC samples used in the analysis. From left to right: SM processes and signal process, the generator used, order of differential cross-section calculation, generator used for the simulation of parton showers, and the parton distribution function (PDF).

Process	Generator	Order	Parton shower	PDF
WW, WZ, ZZ$\rightarrow lX/l\nu/ll$	SHERPA 2.2.1-2	NNLO	SHERPA 2.2.1-2	NNPDF3.0NNLO
$q\bar{q} \rightarrow Z/\gamma \rightarrow \tau\tau$	SHERPA 2.2.1	NNLO	SHERPA 2.2.1	NNPDF3.0NNLO
$q\bar{q} \rightarrow Z/\gamma \rightarrow ee, \mu\mu$	POWHEG	NLO	PYTHIA 8	CT10
$t\bar{t}$	POWHEG	NLO	PYTHIA 8	NNPDF3.0NLO
Single Top, $Wt \rightarrow X$	POWHEG	NLO	PYTHIA 8	NNPDF3.0NLO
RS $G^* \rightarrow ll$	PYTHIA 8	LO	PYTHIA 8	NNPDF23LO

mass. The masses of G^* range from $m_{G^*} = 0.75$–$5\,\text{TeV}$. There are three coupling strengths for each m_{G^*}, $k/\overline{M}_{Pl} = 0.1, 0.2, 0.3$. As we are dealing with three separate subperiods of data-taking during Run 2 of the LHC, each with a corresponding integrated luminosity, we similarly have three separate signal samples comparable to each subperiod just as we do too for the background. Some couplings were not available to this project due to the deletion of datasets. Generating new MC samples was not part of this thesis. An overview of the available signal samples are summarized in table 6.2. Any missing coupling strengths of m_{G^*} from a subperiod will be accounted for by scaling accordingly[2], to the total integrated luminosity $L_{\text{tot}} = 139\,\text{fb}^{-1}$ in order to obtain an accurate picture of the signal resonances.

Table 6.2: Available signal masses, m_{G^*}, for the RS G^* and coupling strengths, $k/\overline{M}_{Pl}$, per subperiod of Run 2 of the LHC, generated by PYTHIA 8 to LO.

		750 GeV	1000 GeV	2000 GeV	3000 GeV	4000 GeV	5000 GeV
$G^* \rightarrow ee$	run a	0.1, 0.3	0.1, 0.2	0.1, 0.2	0.1, 0.2, 0.3	0.1, 0.2, 0.3	0.1, 0.2, 0.3
	run d	0.1, 0.2, 0.3	0.2, 0.3	0.2	0.1, 0.2, 0.3	0.2	0.1, 0.2
	run e	0.1, 0.2, 0.3	0.1, 0.2, 0.3	0.1, 0.2, 0.3	0.1, 0.2, 0.3	0.1, 0.2	0.1, 0.2, 0.3
$G^* \rightarrow \mu\mu$	run a	0.1, 0.2, 0.3	0.1, 0.2, 0.3	0.2	0.1, 0.3	0.1, 0.2	0.1, 0.2, 0.3
	run d	0.1, 0.2, 0.3	0.1, 0.2, 0.3	0.1	0.2, 0.3	0.1, 0.3	0.1, 0.2, 0.3
	run e	0.1, 0.2, 0.3	0.1, 0.2, 0.3	0.1, 0.2, 0.3	0.1, 0.2, 0.3	0.1, 0.3	0.1, 0.2, 0.3

6.2.3 Reweighting and scaling

Each MC sample undergoes a reweighting on an event-by-event basis in order to better describe the data. Furthermore, each MC sample also undergoes a scaling in order to account for the difference in the expected number of events and simulated number of

[2]That is if we disregard potential changes between runs a, d and e in detector conditions and pile-up, which in turn could affect the efficiencies and resolutions.

events. The reweighting and scaling of simulated events are two important steps used in obtaining the correct background estimation.

Event weights

The different event weights used in this analysis is listed below:

- *Pile-up weight*: Each MC sample is produced with an average number of interactions per bunch crossing modelled on the data. Since the data is produced either after or simultaneously with the simulation process of the MC samples, we have no way of obtaining the true pile-up conditions during the simulations. Thus, each event from a simulation process passing the offline selection is corrected with a pile-up weight to better match the data.

- *Lepton and trigger weight*: In order to account for differences in the efficiencies in the data and MC related to the lepton reconstruction we apply two weights, each separately describing one lepton channel (electron and muon).

- *K-factor weight*: Not to be confused with the warp factor k in the graviton coupling, the K-factor takes into account higher-order corrections to the cross-section. It is defined as the ratio of a higher order differential cross-section (e.g. NNLO) over the differential cross-section of the MC sample in question (e.g. NLO).

- *Filter efficiency weight*: The filters on a generator level has a certain efficiency of disregarding uninteresting events. If a filter has a 50% efficiency, and a cut of say $m_{ll} > 100\,\text{GeV}$ is applied, then only half the amount of interesting events is considered. The cross-section used in a MC sample is the *total* cross-section for a process. In order to correctly reflect the efficiency of the triggers we scale the cross-section by the generator filter efficiency.

- $t\bar{t}$ *weight*: This weight applies to $t\bar{t}$-processes and, similarly to the k-factor, is meant as a correction for higher-order estimations of the cross-section.

- *MC weight*: The MC weight is related to the simulation of an event, and is most relevant for processes produced using Sherpa. In other cases it is set very close to one.

Scaling

Each MC sample is simulated using a specific cross-section corresponding to the process in question. The total number of expected events, N_{exp}, for a given integrated luminosity L is found by multiplying the two variables together. The number of events produced in a MC sample is thereby scaled up to correspond with the number of expected events using the scale factor

$$\text{sf} = \frac{N_{\text{exp}}}{N_{\text{sim}}} = \frac{\sigma L}{N_{\text{sim}}}. \tag{6.1}$$

6.3 Event selection

6.3.1 Object definitions and pre-selection

Before delving into the dilepton final state with all criteria imposed, we shall first look at the object definitions set at the primary stage when producing dilepton ntuples from final states of pp collisions.

Baseline selection

The samples were produced with a set of baseline requirements. The baseline selection helps reduce the vast amount of data to events which may be interesting for an analysis. Among the requirements we impose electrons to pass a variation of the *Loose* identification working point, known as *LooseAndBLayer*. This criterion uses the same transformed discriminant d'_L threshold (4.11) as the *Loose* working point, but with the additional requirement of a hit in the innermost pixel layer. Furthermore, we require muons to pass the *high-p_T* identification working point [3]. An event in either channel is required to have at least one reconstructed primary vertex.

Electron channel

An electron candidate is required to have $|\eta| < 2.47$, i.e. be in the precision region of the ATLAS detector, excluding the calorimeter crack region $1.37 < |\eta| < 1.52$, and have $E_T > 20\,\text{GeV}$. The pre-selection contains an identification criterion of *Medium*, thereby reducing background from e.g. jets, at the cost of a small decrease in the efficiency.

To distinguish signal electrons from background electrons, that is prompt electrons vs. electrons originating from non-prompt processes such as jets or bremsstrahlung, we look at the amount of activity in the vicinity of an electron. The track of background electrons are often surrounded by other particles, in contrast to signal electrons which appear isolated. The isolation requirement follow the criteria imposed in the category *Gradient*, i.e. the isolation efficiency is dependent on E_T and uniform in $|\eta|$.

Furthermore, electrons are required to pass the recommended ID track requirements $|d_0/\,\sigma(d_0)| < 5$ and $|\Delta z_0 \sin\theta| < 0.5\,\text{mm}$. The criteria listed here are summarised in table 6.3.

Muon channel

A muon candidate is required to have $|\eta| < 2.5$, i.e. be within the region measurable to the ID, and have $p_T > 20\,\text{GeV}$. Furthermore, a muon is identified using the *high-p_T* criterion. That is, selecting only CB muons with at least three hits in the MS trigger system chambers in order to optimise the muon momentum resolution in the MS[4] and improve the reconstruction of a track's curvature. This requirement in turn reduces the identification efficiency by $\sim 20\%$ due to requiring a greater number of hits.

[3] See subsection 4.3.2.

[4] See table 4.2 in subsection 4.2.3.

A muon must also pass the *TightTrackOnly* isolation working point. That is, a muon must have $p_T^{\text{varcone30}}/p_T^{\mu} < 0.06$, meaning the scalar sum of transverse momenta in a cone of radius $\Delta R = \min(10\,\text{GeV}/p_T^{\mu}, 0.3)$ must be less than 6% of the transverse momentum p_T^{μ} of the muon candidate. Keeping a maximum size on the cone for high-p_T leptons we suppress the probability of mis-reconstructed muons.

Lastly, the muons must pass the recommended ID track requirements $|d_0/\,\sigma(d_0)| < 3$ and $|\Delta z_0\,\sin\theta| < 0.5\,\text{mm}$. The criteria listed here are summarised in table 6.3.

Table 6.3: Object definitions and pre-selection in the dielectron and dimuon channels.

Channel	Electron (e)	Muon (μ)
Identification	Medium	High-p_T
Isolation	Gradient	TightTrackOnly
$\lvert\eta\rvert$	< 2.47 and $1.37 \not< \lvert\eta\rvert \not< 1.52$	< 2.5
E_T, p_T	$E_T > 20\,\text{GeV}$	$p_T > 20\,\text{GeV}$
$\lvert d_0/\sigma(d_0)\rvert$	< 5	< 3
$\lvert\Delta z_0 \sin\theta\rvert$	$< 0.5\,\text{mm}$	$< 0.5\,\text{mm}$

6.3.2 Triggering and offline selection

After the baseline selection and object definitions, we further look at the triggering criteria used for our selection of dilepton pairs. The triggering on lepton pairs is referred to as an *online* selection, while the *offline* selection are any cuts imposed after the triggers.

Electron channel

Since we are working with high-mass resonances it is desirable to maintain a high efficiency at large E_T, thus we trigger on two electrons with $E_T > 12\,\text{GeV}$ passing the electron working point *Loose*[5]. Furthermore, two electrons passing the electron working point *VeryLoose* with $E_T > 17\,\text{GeV}$ or $E_T > 24\,\text{GeV}$ are also selected for the analysis[6]. The loosest possible criteria are imposed in order to be able to obtain a fair estimation on the fakes contribution to the background.

As we are interested in electron pairs in the final state we must require two isolated electrons. Both electrons are required to have $p_T > 30\,\text{GeV}$ and an invariant mass $m_{ee} > 70\,\text{GeV}$. Lastly, we do not impose any charge requirements on the electron pairs due to possible charge misidentification, whose probability increases for higher E_T, and the possibility of overlooking non-negligible signal events, further discussed in subsection 6.4.1. Table 6.4 shows a summary of the offline selection criteria for electrons.

[5]These two criteria combined are contained in the HLT_2e12_lhloose_L12EM10VH.
[6]Described by triggers HLT_2e17_lhvloose_nod0 and HLT_2e24_lhvloose_nod0.

Muon channel

A high muon efficiency at high-p_T is desirable. We either trigger on a muon if it has $p_T > 26\,\text{GeV}$, which is the lowest p_T trigger threshold available[7], or if it has $p_T > 50\,\text{GeV}$ as the trigger efficiency drops at very high-p_T when combined with the muon criterion in the first p_T trigger case.[8]

In the muon channel we are interested in final states involving two isolated muons. Both muons passing the above triggers are further required to have $p_T > 30\,\text{GeV}$ and have an invariant mass $m_{\mu\mu} > 70\,\text{GeV}$. Although the probability for an event to contain a "bad" muon, described in subsection 4.4.1, is quite small, we still impose a veto on such events due to their significantly worse momentum resolution [46]. Finally, we impose an opposite-charge requirement on muons, as any contributions from charge-misidentifications are near negligible throughout the p_T-spectrum. This requirement reduces background contributions from diboson-processes. Table 6.4 shows a summary of the offline selection criteria for muons.

Table 6.4: Offline selection in the dielectron and dimuon channels.

Offline selection	
Electron (e)	Muon (μ)
Two isolated electrons	Two isolated muons
No charge requirement	Opposite charge requirement
$p_T > 30\,\text{GeV}$	$p_T > 30\,\text{GeV}$
$m_{ee} > 70\,\text{GeV}$	$m_{\mu\mu} > 70\,\text{GeV}$

6.4 First look at background and signal

To begin with we look at simulated prompt background and signal lepton pairs passing the pre-selection in table 6.3 and the offline selection in table 6.4, using an integrated luminosity $L_{\text{tot}} = 139\,\text{fb}^{-1}$. Unless stated otherwise, L_{tot} will be the standard choice of integrated luminosity for distributions shown throughout this analysis. The weights and scaling mentioned in subsection 6.2.3 are also applied to all data in these next sections.

6.4.1 Motivation for charge selection

Figure 6.6 shows the invariant mass distributions for various combinations of charged leptons. An example of the signal $m_{G^*} = 2\,\text{TeV}$ (shown as fully drawn lines) shows increasing decay width at increasing coupling strengths $k/\overline{M}_{Pl} = 0.1$–$0.3$. The lower plots show the expected significance Z under the signal+background hypothesis H_1. The significance for each bin was calculated following eq. (5.7) in subsection 5.1.1. The p-value, that is the probability of observing at least $N_{bkg} + N_{sig}$ events in a bin given

[7] Described by triggers HLT_mu26_imedium and HLT_mu26_ivarmedium.
[8] Described by the HLT_mu50.

the expected number of events under H_0, N_{bkg}, was calculated by eq. (5.6) where t is set as $N_{bkg} + N_{sig}$ number events and the integral is the sum over Poisson terms.

The distribution of total number $e^{\pm}e^{\pm}$–pairs (6.6(a)) differs from the number of $e^{\pm}e^{\mp}$–pairs (6.6(c)) by only about 2 orders of magnitude, compared to the two dimuon channels which differ by about 5 orders of magnitude. Diboson processes are the dominating background in the $\mu^{\pm}\mu^{\pm}$ channel (6.6(b)) as Drell-Yan and top processes mostly contribute in the opposite–sign channel. Therefore, due to low probability of muon charge mis-identification, the Drell-Yan and top processes combined contribute less than 13% in the $\mu^{\pm}\mu^{\pm}$ channel, but dominate in the $\mu^{\pm}\mu^{\mp}$ channel (6.6(d)). Thus, the muon same sign–channel can be neglected, and we will refer to dimuon pairs as "$\mu^+\mu^-$" from now on.

Electrons[9] are prone to charge mis-identification at high $|\eta|$, as seen in figure 6.7 around $1.5 < |\eta| < 2.2$. This is a consequence of photon conversions, bremsstrahlung and decreasing sagitta of the track curvature due to higher p_T. Figure 6.6 reflects the impact of charge mis-identifications at high m_{ll}, where the total background contributions in the opposite (6.6(a)) and same-sign (6.6(c)) channels become nearly indistinguishable. Furthermore, the ratio of events between the opposite-sign channel over the same-sign channel at the 2 TeV signal resonance with coupling 0.1 is 9.3 for the background while for the signal it is 10.7. In other words, the scaling for both the background and signal is reduced by a factor ~ 10 when moving from the $e^{\pm}e^{\mp}$-channel to the $e^{\pm}e^{\pm}$-channel. Looking at the expected significance in the lower subplots, the equivalent ratio between the two channels is ~ 3.3. So, in contrast to the significance in the muon channel, the expected significance in the electron same-sign channel cannot be neglected, and the dielectron pair will thus be referred to as "ee" from now on.

6.4.2 Signal invariant mass distributions

Figure 6.8 shows the invariant mass distribution for each graviton mass between 0.75 TeV and 5 TeV with couplings between 0.1–0.3. Each signal exhibits a small parton-luminosity tail in the lower m_{ll} regions. The tails are not very prominent in the invariant mass distributions for the G^*, but the decay width for each coupling is quite distinct, in which it increases for increasing couplings. This reflects in turn how the lifetime τ of the G^* decreases for increasing coupling strengths.

6.4.3 Signal acceptance × efficiency

Using the selection criteria in tables 6.3 and 6.4 we can now calculate the product of signal acceptance and efficiency as a function of mass in the signal region[10] (SR) $m_{ll} \geq 120\,\text{GeV}$. By vetoing the Z-peak we reduce the charge-flip background in the same-sign channel. The acceptance×efficiency ($A \times \varepsilon$) for signal events with a theoretical

[9] Which is here used as the collective term describing both electrons and positrons.

[10] This is the same SR used in the ATLAS paper [27].

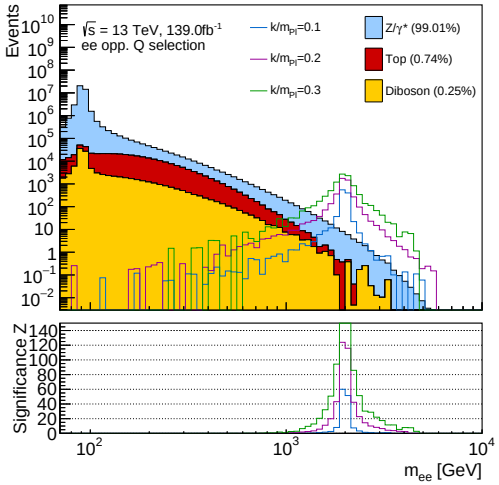

(a) $e^{\pm}e^{\mp}$

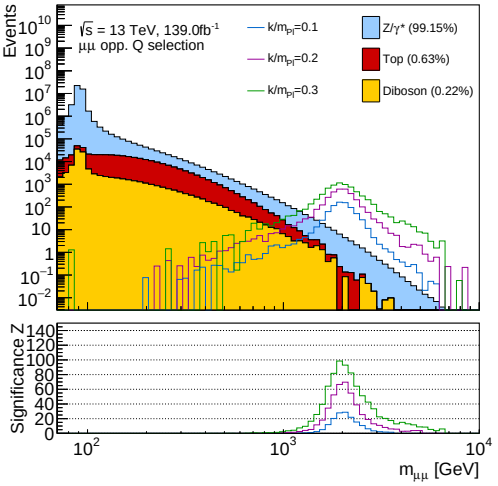

(b) $\mu^{\pm}\mu^{\mp}$

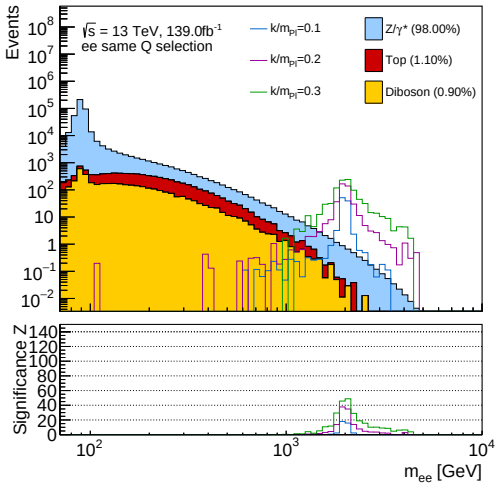

(c) $e^{\pm}e^{\pm}$

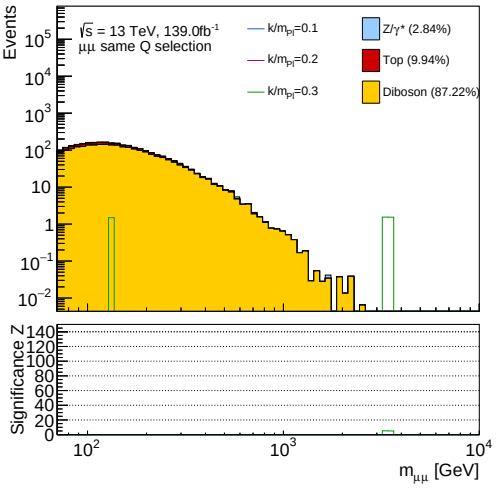

(d) $\mu^{\pm}\mu^{\pm}$

Figure 6.6: Invariant mass distribution m_{ll} of (a) oppositely charged electrons, (b) oppositely charged muons, (c) same charged electrons and (d) same charged muons. The signal used is $m_{G^*} = 2\,\text{TeV}$. Each signal corresponds to a unique coupling parameter k/m_{Pl}, with $m_{Pl} \equiv \overline{M}_{Pl}$. The lower plots show the expected significance of $N_{bkg,i} + N_{sig,i}$ for bin i under the background hypothesis H_0. The bin widths follow a logarithmic x-axis, thus the bin widths gradually increase for increasing m_{ll}.

cross-section σ is defined as

$$A \times \varepsilon = \frac{N_{sig,f}}{N_{sig,i}}, \qquad N_{sig,i} \equiv \sigma L, \tag{6.2}$$

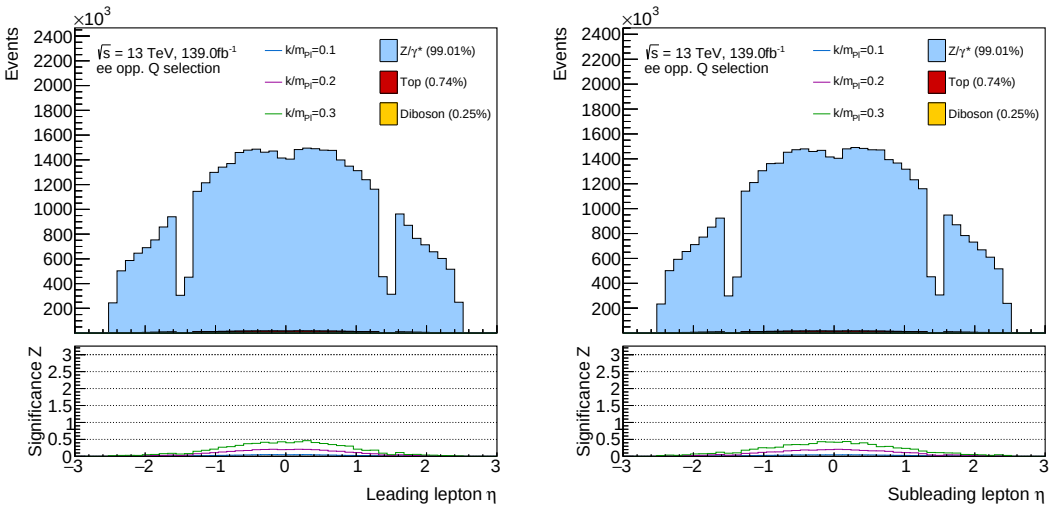

(a) $e^{\pm}e^{\mp}$

(b) $e^{\pm}e^{\mp}$

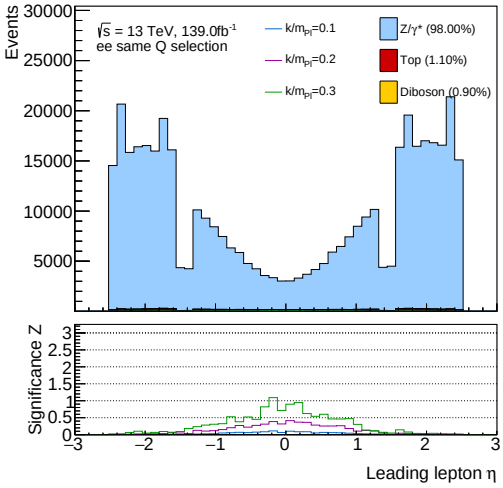

(c) $e^{\pm}e^{\pm}$

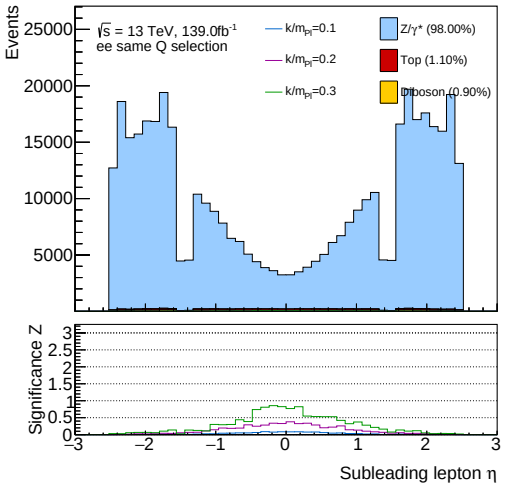

(d) $e^{\pm}e^{\pm}$

Figure 6.7: Pseudorapidity distribution η of (a) leading electron from an opposite-sign channel, (b) subleading electron from an opposite-sign channel, (c) leading electron from a same-sign channel and (d) subleading electron from a same-sign channel. The signal used is $m_{G^*} = 2\,\text{TeV}$, as shown in the upper plots. Each signal corresponds to a unique coupling parameter k/m_{Pl}, where $m_{Pl} \equiv \overline{M}_{Pl}$. The lower plots show the expected significance of $N_{bkg,i} + N_{sig,i}$ for bin i under the background hypothesis H_0.

where $N_{sig,i}$ is the number of initial simulated signal events before imposing any selection criteria, $N_{sig,f}$ is the number of simulated signal events (scaled according to the total luminosity) within the SR making it past all selection criteria, and L is the integrated luminosity.

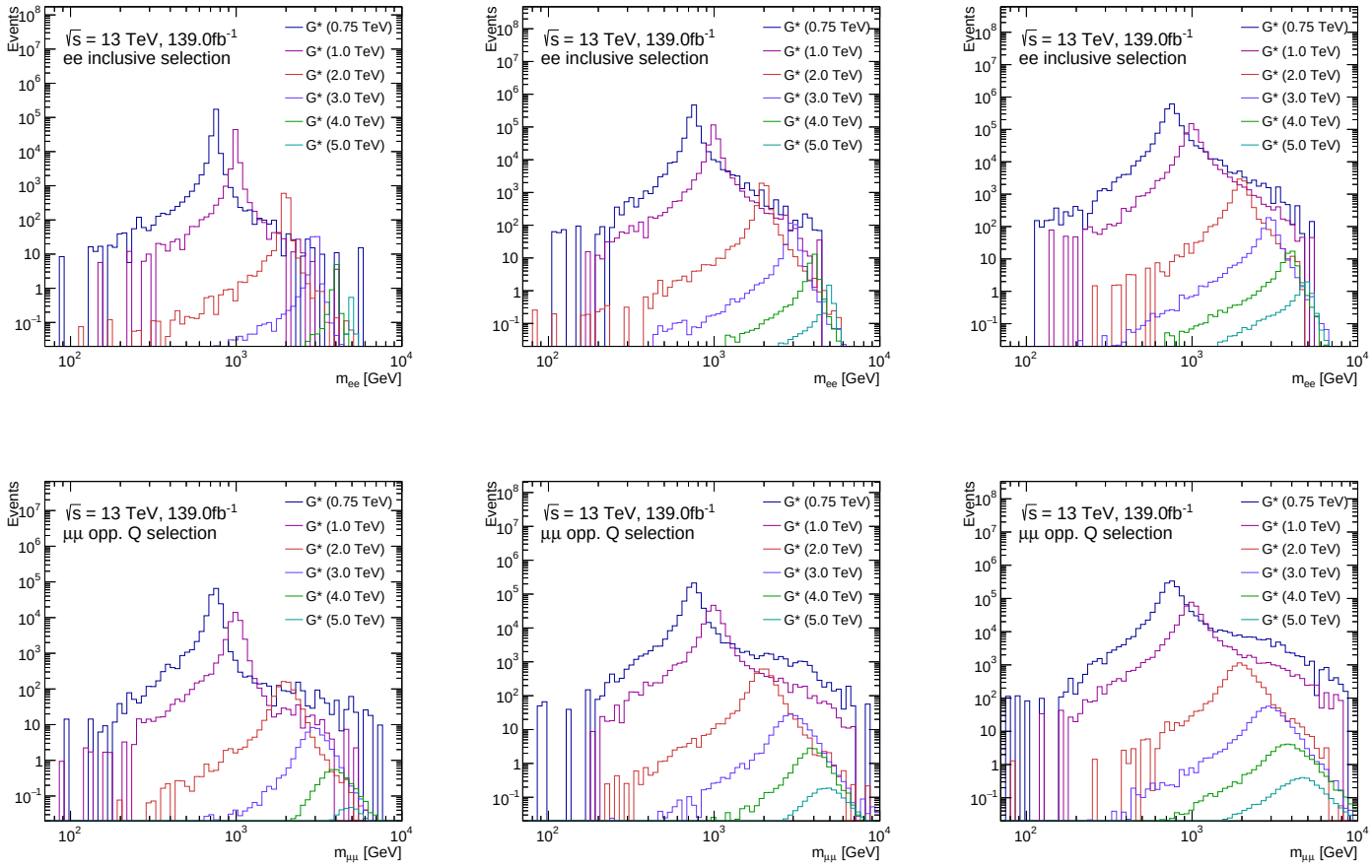

Figure 6.8: Signal invariant mass distributions for masses $m_{G^*} \in [0.75, 5.00]$ TeV with (from left to right) couplings 0.1, 0.2 and 0.3 in the (top) dielectron channel and (bottom) dimuon channel.

As seen in figure 6.9, the $A \times \varepsilon$ for all couplings in the dimuon channel decreases in relation to increasing momenta, whereas the acceptance for dielectrons increases accordingly to increasing energies. This follows the expected behaviour reflected in the momentum and energy resolutions from eq. (4.7). Electrons are characterised according to the energy resolution as they deposit their energy in the calorimeters. Since muons are minimum-ionising they will not be registered in the calorimeters on the same level as electrons, and will instead make it to the muon spectrometer where they are categorised according to the momentum resolution. Furthermore, the $A \times \varepsilon$ for dimuons lie approximately 20% below dielectrons. This could be due to the more stringent selection criteria in the pre-selection for optimised momentum resolution at the expense of a decreased efficiency. The $A \times \varepsilon$ drops again at high invariant masses which could be due to the strongly decreasing parton luminosity at high momentum transfers. It should

also be noted that due to missing signal MC-samples (in both channels) the values for the acceptance might deviate slightly from the case where all couplings are available. An example here is the couplings for mass $m_{G^*} = 2\,\text{TeV}$ in the ee-channel. Coupling 0.2 has signal samples from all subperiods available, compared to the lower-lying $A \times \varepsilon$ for coupling 0.1, where run d is missing, and coupling 0.3 where both runs a and d are missing. In the case of $m_{G^*} = 2\,\text{TeV}$ it is then run e which provides the lowest $A \times \varepsilon$.

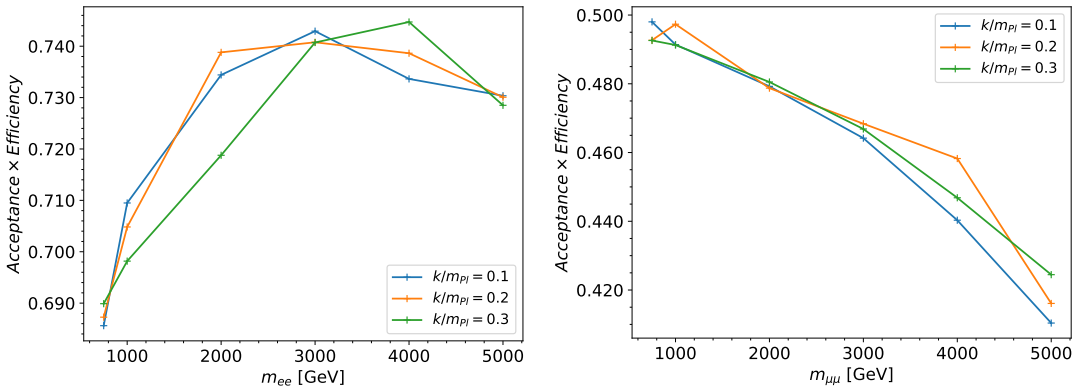

Figure 6.9: Product of acceptance and efficiency, $A \times \varepsilon$, for all three coupling strengths of the G^* in the (left) dielectron and (right) dimuon channels for six graviton mass points in the range 750–5000 GeV in the signal region $m_{ll} \geq 120\,\text{GeV}$. The reduced Planck mass $\overline{M}_{Pl}$ is denoted as m_{Pl}.

6.5 Fake lepton background

An additional background contributing to the observed data stems from signatures of jets passing the lepton selection criteria, i.e. true fakes. Other sources of fake leptons include photon conversions and semi-leptonic decays of b- and c-quarks. Contributions from fake leptons are expected to be negligible in the dimuon channel [27], and we will thus restrict the inclusion of fake leptons to the dielectron channel. The summary of the data-driven technique used to estimate the amount of fake leptons is largely based on Refs. [41, 47, 48].

6.5.1 Matrix method

Fake leptons are accounted for using a data-driven technique known as the *matrix method*. We first separate between two classes of leptons:

- A "real" lepton, defined as a prompt isolated lepton not originating from a jet.
- A "fake" lepton, defined as a non-isolated, non-prompt lepton.

The matrix method is based on two separate working points; (*i*) *loose* and (*ii*) *tight*. The number of leptons passing the loose selection, also known as *inclusive loose*, is denoted N_L while the number leptons passing the tight selection is denoted N_T. The number of leptons which pass only the loose selection criteria but not tight are known as *exclusive loose* and are denoted as $N_{L'}$. In essence, $N_L \supset N_{L'}$ and $N_L \supset N_T$. Sample events containing lepton pairs are thereby split into four measurable quantities, N_{TT}, $N_{TL'}$, $N_{L'T}$ and $N_{L'L'}$, with subscripts from left to right denoting the leading and subleading lepton candidates.

The efficiency r of a real lepton (superscript R) passing the tight selection given that it passes the loose criteria, and the corresponding efficiency f for a fake lepton (superscript F), is defined as

$$f = \frac{N_T^F}{N_L^F} \text{ and } r = \frac{N_T^R}{N_L^R}. \tag{6.3}$$

We assign such probabilities to each lepton included in the final state. The number of leptons originating from lepton pairs passing either the loose (L - inclusive, L' - exclusive) or tight (T) selection criteria and the number of real and fake leptons passing the loose criteria is related by

$$\begin{bmatrix} N_{TT} \\ N_{TL'} \\ N_{L'T} \\ N_{L'L'} \end{bmatrix} = \mathbf{M} \begin{bmatrix} N_{LL}^{RR} \\ N_{LL}^{RF} \\ N_{LL}^{FR} \\ N_{LL}^{FF} \end{bmatrix}, \tag{6.4}$$

where $\mathbf{M}$ is a 4×4 matrix

$$\mathbf{M} = \begin{bmatrix} r_1 r_2 & r_1 f_2 & f_1 r_2 & f_1 f_2 \\ r_1(1-r_2) & r_1(1-f_2) & f_1(1-r_2) & f_1(1-f_2) \\ (1-r_1)r_2 & (1-r_1)f_2 & (1-f_1)r_2 & (1-f_1)f_2 \\ (1-r_1)(1-r_2) & (1-r_1)(1-f_2) & (1-f_1)(1-r_2) & (1-f_1)(1-f_2) \end{bmatrix}. \tag{6.5}$$

The elements contained in the vector on the left hand side of eq. (6.4) are exclusive, meaning that the elements are not subsets of one another. The number of real and fake leptons passing the tight selection (N_{TT}), thus reconstructed as being signal-like electrons, is found by multiplying out the components of the first row from the matrix multiplication above,

$$\begin{aligned} N_{TT}^{l+l} &= r_1 r_2 N_{LL}^{RR} \\ N_{TT}^{l+jets} &= r_1 f_2 N_{LL}^{RF} + f_1 r_2 N_{LL}^{FR} \\ N_{TT}^{di\text{-}jet} &= f_1 f_2 N_{LL}^{FF}. \end{aligned} \tag{6.6}$$

Finally, the total number of fake lepton pairs reconstructed as signal-like lepton candidates are defined as lepton pairs containing at least one fake originating from a jet,

$$N_{TT}^{\text{fakes}} = N_{TT}^{l+jets} + N_{TT}^{di\text{-}jet}. \tag{6.7}$$

The estimation of the efficiencies is measured from control regions which contain a high purity[11] of either real of fake leptons depending on which efficiency parameter is of interest. A high purity in this context means the amount of "real" leptons contaminating the fake control region, and vice versa.

The real efficiency is measured from control regions which contain a high purity of real leptons. The region around the Z-peak contains a high purity of real leptons, and this is thus a typical choice to calculate r.

The fake efficiency is estimated by calculating the ratio of number of objects passing the tight selection over the number of objects passing the loose selection. Real leptons have a greater probability passing the tight selection than fakes do, which in turn falsely increases the efficiency f. The estimation of the fakes purity in a fake control region is found by "lepton subtraction". That is, since we have no way of actually *observing* the amount of real and fake leptons in a detector, we subtract all leptons originating from SM backgrounds using MC,

$$\text{purity}_{fake} = \frac{N_{\text{data}}^{\text{leptons}} - N_{\text{MC real}}^{\text{leptons}}}{N_{\text{data}}^{\text{leptons}}} = \frac{N_{\text{fake}}^{\text{leptons}}}{N_{\text{data}}^{\text{leptons}}}, \tag{6.8}$$

to find the purity of fakes in the fake control region. The subtraction of leptons originating from SM backgrounds using MC also applies to the fake efficiency from eq. (6.3), that is

$$f = \frac{N_T^l - N_T^{MC}}{N_{loose}^l - N_{loose}^{MC}}. \tag{6.9}$$

6.5.2 Misidentified electrons in the signal region

Due to poor estimation results of the real efficiency r in the region around the Z-peak[12], the contribution of fakes is only taken into account for invariant masses above the Z-peak, that is $m_{ll} \geq 130\,\text{GeV}$. Figure 6.10 shows the effect of excluding vs. including fakes in the SR. Despite its low contribution in lower m_{ll} regions, the relative contribution of the fakes background to the total background increases in importance at higher invariant masses, due to e.g. increasing probability for bremsstrahlung and decreasing track sagittae.

6.6 Data/MC distribution comparisons

Figure 6.11 shows the invariant mass distributions in the mass range $120 < m_{ll} < 10\,000\,\text{GeV}$ for the dielectron and dimuon channel. Figures 6.13 and 6.14 show the distributions for transverse momenta and pseudorapidity, respectively. The grey bands

[11] "Purity" refers to the relative amount of real (fake) leptons contained in a fake (real) control region.

[12] The number of estimated fake background events around the Z-peak is highly sensitive to small deviations in the real efficiency.

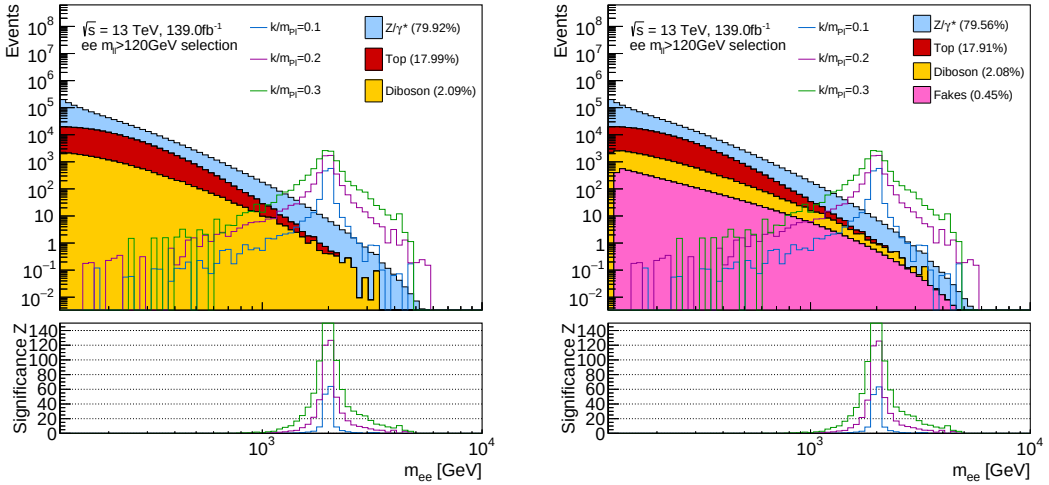

Figure 6.10: Invariant mass distribution when (left) excluding misidentified electrons, i.e. fakes, and (right) including fakes in the SR. The distribution of fakes was estimated using the matrix method for an integrated luminosity $L = 139\,\text{fb}^{-1}$ in the signal region (SR) $m_{ll} \geq 120\,\text{GeV}$. The signal included is $m_{G^*} = 2\,\text{TeV}$.

show the systematic uncertainties (see Section 6.7) associated with the simulated background, while the red arrows indicate bins containing a data over background ratio which exceeds the limits in the lower subplots.

6.6.1 Dielectron channel

The maximum dielectron invariant mass observed during Run 2 is 4.06 TeV. In addition, the maximum observed p_T for the leading and subleading electrons is 2.02 TeV and 1.93 TeV, respectively. From figure 6.11 the amount of observed data and MC background is approximately equal, with the ratio steadily remaining around 1, in the lower regions in the dielectron channel with minor statistical uncertainties related to the data points. The differences between data and simulations become more apparent as we approach yet higher invariant mass regions, $m_{ee} > 500\,\text{GeV}$, where the number of data events is restricted by statistics. Table 6.5 shows the total contribution of each background with corresponding systematic uncertainties.

Towards the tail at high invariant masses we see a slight deviation in the observed data from the simulated background. Specifically, the two bins after the 2 TeV mark contains 7 and 8 observed events, whereas the number of background events in the same bins are 3.36 and 2.54. Summing the contents in these two bins we find an observed significance of $Z_{obs} = 3.13\sigma$. These data points could also be mere statistical fluctuations, although the error bars on the data points lie outside the region of the background expectation. Figure 6.12 shows the relative contribution to the background and observed data from each sub-run in Run 2. The outliers are visible in each sub-run

Table 6.5: Expected background yields and observed data in the dielectron channel for a given mass range (left-most column). The quoted uncertainties have been calculated from a combination of theoretical (DY only) and experimental systematics. A 100% uncertainty is assigned to the fakes background. A "−" corresponds to no events being found.

m_{ee} range [GeV]	Observed yield	Total SM	DY	Top	Dibosons	Jet mis-identification
70–120	43 645 657	41 858 080±219 3175	41 649 562±2 193 172	122 631±1 378	85 887±3 563	–
120–400	1 105 825	1 083 526±38 303	864 617±37 783	192 458± 4027	21 853±1 487	4 598±4 598
400–600	20 565	20 106±1 272	13 682±1 066	5 315±564	853±316	256±256
600–900	4 744	4 596±460	3 480±310	816±275	206±178	94.51±94.51
900–1 300	919	893±151	729±90	87.40±82.75	47.77±85.32	29.00±29.00
1 300–1 800	166	170±27	144±22	8.36±3.31	9.44±14.14	8.25±8.25
1 800–3 000	38	38.02±6.04	32.37±5.35	0.82±0.21	2.12±0.75	2.70±2.70
>3 000	2	1.57±0.39	1.28±0.34	–	0.11±0.02	0.19±0.19

for the same mass bins. However, the error bars on these mass points are within the background expectation, thus implying that they could indeed be statistical fluctuations.

Distributions of the leading and subleading electron transverse momenta are seen in figure 6.13. The majority of both observed and simulated events lie in the lower p_T-regions, which is consistent with the distributions of the invariant mass. The data points which exceed the limits of the lower subplot lie in the higher transverse momentum region ($p_T \geq 500\,\text{GeV}$), where the statistics are less than 100 events per bin thereby leading to a more unstable ratio. Furthermore, it should be mentioned that the data-driven background used in this analysis was applied to the invariant mass only, however, this should not affect the statistical analysis later on. The fluctuations in the systematics for leading electrons compared to subleading electrons could be due to contributions from theoretical systematics from the DY background. For instance, the DY background and single events from the diboson background contribute to the total background for leading electrons towards the tail (between 1 500 and 2 000 GeV), whereas the DY background dominates when $p_T \gtrsim 1\,500\,\text{GeV}$ for the subleading electrons.

6.6.2 Dimuon channel

The maximum dimuon invariant mass observed during Run 2 is 2.75 TeV. Additionally, maximum observed p_T for the leading and subleading muons is 2.60 TeV and 1.04 TeV, respectively. Similarly to the dielectron channel the ratio remains steadily around 1 in the lower mass regions, as can be seen from figure 6.11. Fluctuations begin to occur as the number of observed events drops below 10^4, i.e. $m_{\mu\mu} \gtrsim 0.5\,\text{TeV}$. In the higher mass regions, where the ratio is restricted by statistics, there is a greater uncertainty related to the observed data. The contributions of each background is approximately the same as that for the dielectron channel. The total contribution of each background with corresponding systematic uncertainties is found in table 6.6.

The transverse momenta distributions for the leading and subleading muon candid-

Table 6.6: Observed and expected background yields in the dimuon channel for a given mass range (left-most column). The quoted uncertainties have been calculated from a combination of theoretical (DY only) and experimental systematics. A "−" corresponds to no events being found.

$m_{\mu\mu}$ range [GeV]	Observed yield	Total SM	DY	Top	Dibosons
70–120	46 966 911	45 240 347±2 550 357	45 040 986±2 550 355	115 354±2 007	84 007±2 690
120–400	1 017 542	1 001 638±36 795	811 725±36 539	171 450±4 088	18 463±1 457
400–600	16 156	16 175±936	10 865±655	4 652±587	658±322
600–900	3 476	3 503±401	2 640±196	709±303	154±177
900–1 300	613	638±132	528±66	76.42±92.56	34.43±68.88
1 300–1 800	105	115±23	24.66±8.26	6.76±2.77	8.16±13.53
1 800–3 000	18	25.21±5.64	23.39±5.61	0.68±0.06	1.14±0.57
>3 000	−	1.29±2.65	1.27±2.65	−	0.02±0.00

ates are seen in figure 6.13. The contributions of the uncertainties related to different backgrounds lead to fluctuations in the systematics, as was discussed in the dielectron channel. Furthermore, the distributions of the leading and subleading muons differ by the p_T range. That is, leading muons reach a higher p_T than subleading muons (as per definition of leading muons) resulting in a wider p_T range.

6.7 Systematic uncertainties

Any uncertainties which are regarded to have a non-negligible impact on the cross-section limits are seen as nuisance parameters. The systematic uncertainties displayed in the plots are calculated using the description in eq. (4.12), in which we assume no correlations between the nuisance parameters. For each systematics source a variety of up/down errors are calculated as

$$\Delta_{\text{up}} = \frac{y_{\text{up}} - y_{\text{nominal}}}{y_{\text{nominal}}}, \tag{6.10}$$

where each $\Delta_{\text{up}} = -\Delta_{\text{down}}$. The contributions of each non-negligible nuisance parameter, as a function of the invariant mass, to the total background uncertainty are shown in figure 6.15, while the up- and down variations for each nuisance parameter are shown individually in appendix B. Additionally, any theoretical uncertainties included in this analysis arise from the dominating DY background. The nuisance parameters included are EW and photon-induced corrections, the strong coupling constant (α_s), choice of PDF, and variations of PDF scales. There are seven PDF variations, each treated as a separate nuisance parameter.

The uncertainty on the energy resolution in the electron channel is relatively small compared to the experimental uncertainties arising from the energy scale and beam energy. By assigning a 100% uncertainty on the fakes background we include an additional uncertainty in the electron channel which increases as a function of m_{ll}. This

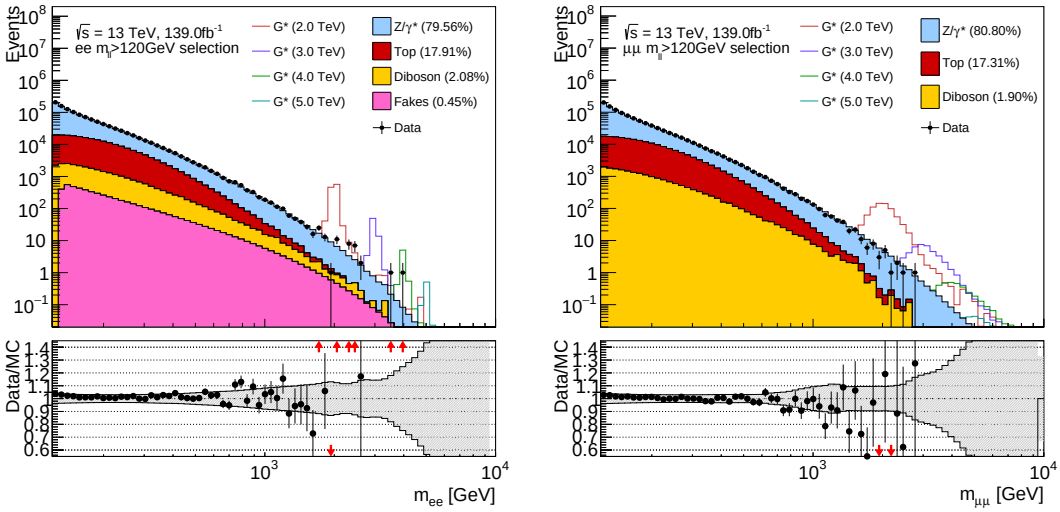

(a) ee (b) $\mu^{\pm}\mu^{\mp}$

Figure 6.11: Comparison of invariant mass distributions provided by background and observed data in mass range $120 \leq m_{ll} \leq 10\,000$ GeV for (a) dielectron channel and (b) dimuon channel in the upper subplot, and corresponding ratio of data over background for a given bin in the lower subplot. Signals $m_{G^*} = 2, 3,$ 4 and 5 TeV with coupling 0.1 are also shown. The systematics in the grey shaded bands were "smoothed" prior to plotting.

also reflects the increasing contribution of fakes compared to the total background at high m_{ll}. The theoretical uncertainties represent the largest background uncertainties in the dielectron channel, with the "PDFReducedChoiceNNPDF" and the 2nd and 5th PDF variations being the top contributors towards the tail.

The momentum resolution for muons is determined both from the MS and the ID. The uncertainty on these momentum resolutions are among the top contributors to the total uncertainty in the muon channel. In addition there is a charge-dependent contribution from the sagitta residual bias[13] whose contribution is relatively small. The uncertainty on the reconstruction efficiency is the fourth highest contributor among the experimental uncertainties. Despite the large uncertainties related to the muon momentum resolutions, it is in fact uncertainties related to the bad muon veto which pose as the greatest uncertainty in the higher m_{ll} regions. Among theoretical uncertainties it is the "PDFReducedChoiceNNPDF" which contribute the most, followed by the 2nd PDF variation. The uncertainty on the reconstruction efficiency exceeds 30% at high invariant masses in the muon channel, while it is nearly negligible in the electron channel.

[13] Abbreviated as "RESBIAS".

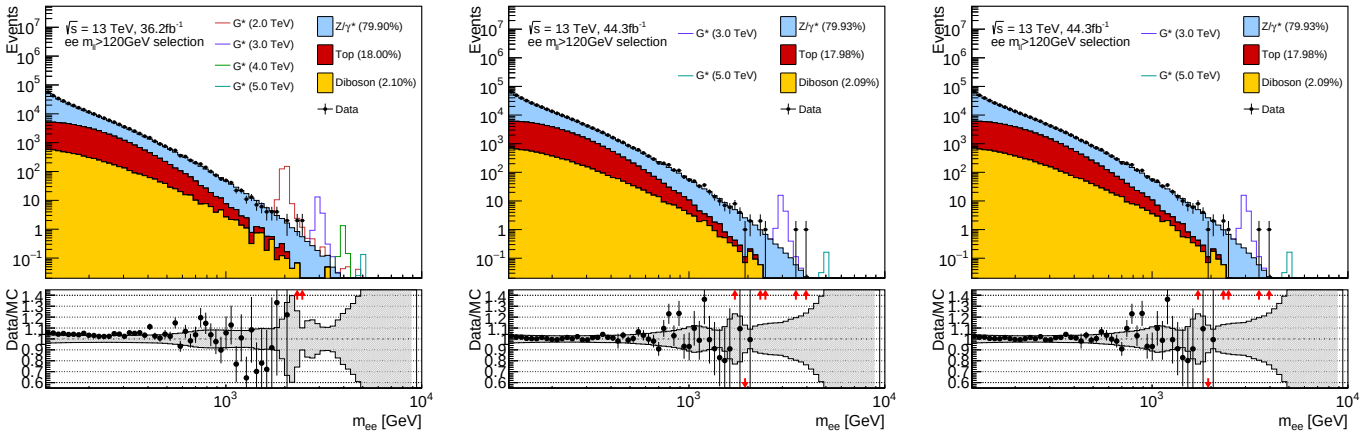

(a) run a (b) run d (c) run e

Figure 6.12: Data/MC invariant mass distributions for subruns a, d and e in the mass range $120 \leq m_{ll} \leq 10\,000\,\text{GeV}$ for the dielectron channel. Signals $m_{G^*} = 2, 3, 4$ and 5 TeV with coupling 0.1 are also shown.

6.8 Statistical analysis

In this section we have a look at the expected and observed upper cross-section limits. Other parameters of interest are the 68% and 95% quantiles[14] extracted from pseudo-experiments generated under the background hypothesis. We will distinguish between two different scenarios: (i) limits without systematic uncertainties, discussed in subsection 6.8.1, and (ii) limits with systematic uncertainties, discussed in subsection 6.8.2, and the production of central limits and quantiles. We also look into the accuracy of the analysis compared to the limits produced for another hypothetical, heavy gauge boson Z'_χ [49].

6.8.1 Exclusion limits - without systematic uncertainties

The BAT program operates with a parameter range $[0, \sigma_{\text{sig,max}}]$, where the maximum upper-cross section, $\sigma_{\text{sig,max}}$, is adjusted manually[15] and is estimated from the upper limit on the number of signal events, $N_{\text{sig,max}}$. Table 6.7 shows the expected limits for the dielectron, dimuon and combined channels when using $L = 139\,\text{fb}^{-1}$.

[14] Also denoted as the 1σ and 2σ bands.

[15] The $N_{\text{sig,max}}$ is estimated from the ratio r of $\sigma_{sig,max} = N_{\text{sig,max}}/[L(A \times \varepsilon)]$ over the expected limit produced, and is adjusted to the point where $r \sim 4$ in order to not lose any interesting insight regarding the production of the exclusion limits. If $\sigma_{sig,max}$ is set too low we could miss out on upper cross-section limits which could have a significance for the analysis.

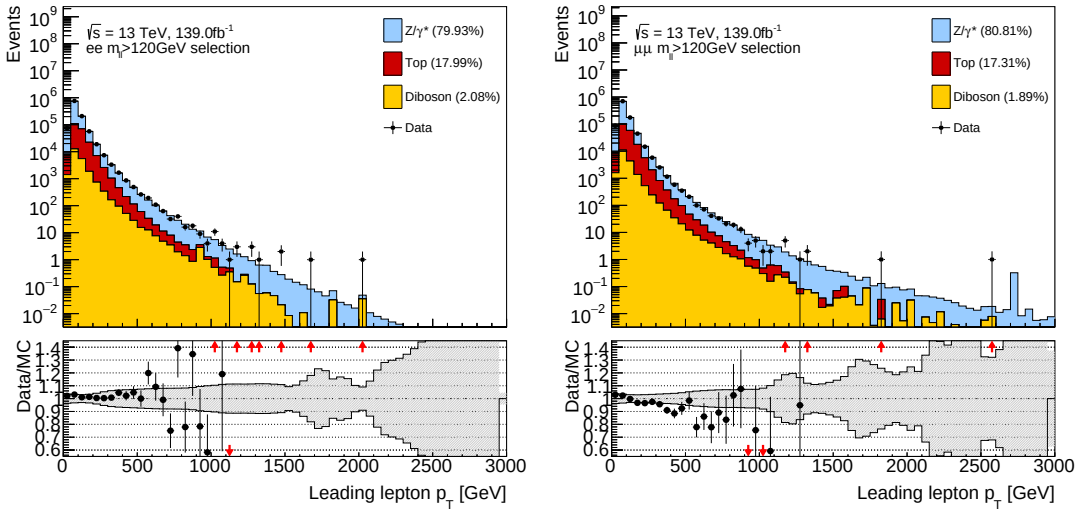

(a) ee

(b) $\mu^{\pm}\mu^{\mp}$

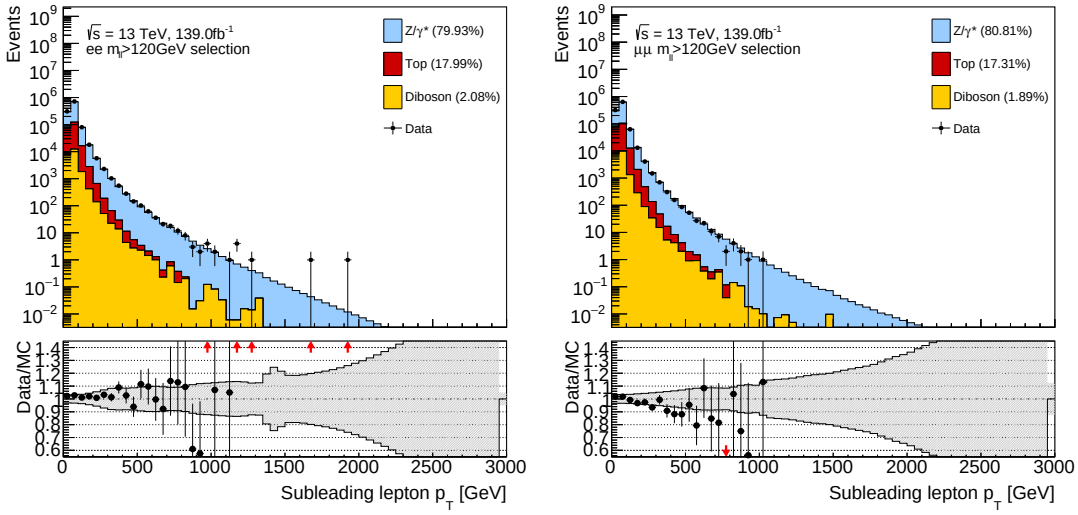

(c) ee

(d) $\mu^{\pm}\mu^{\mp}$

Figure 6.13: Comparison of p_T provided by background and observed data in the SR for leading (a) and subleading (c) lepton in the dielectron channel and leading (b) and subleading (d) lepton in the dimuon channel. The lower subplots show the ratio of data and MC along with systematic uncertainties, shown as grey shaded bands, related to the background.

6.8.2 Exclusion limits - with systematic uncertainties

The inclusion of systematic uncertainties results in more relaxed expected limits, as is seen in table 6.8 and figure 6.17. The effect of background systematics is more notice-

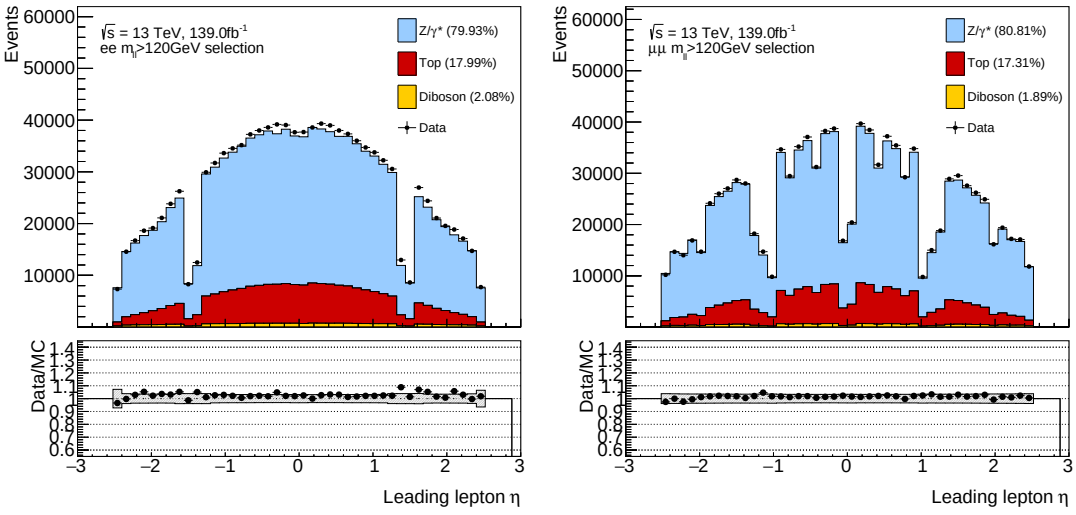

(a) ee

(b) $\mu^{\pm}\mu^{\mp}$

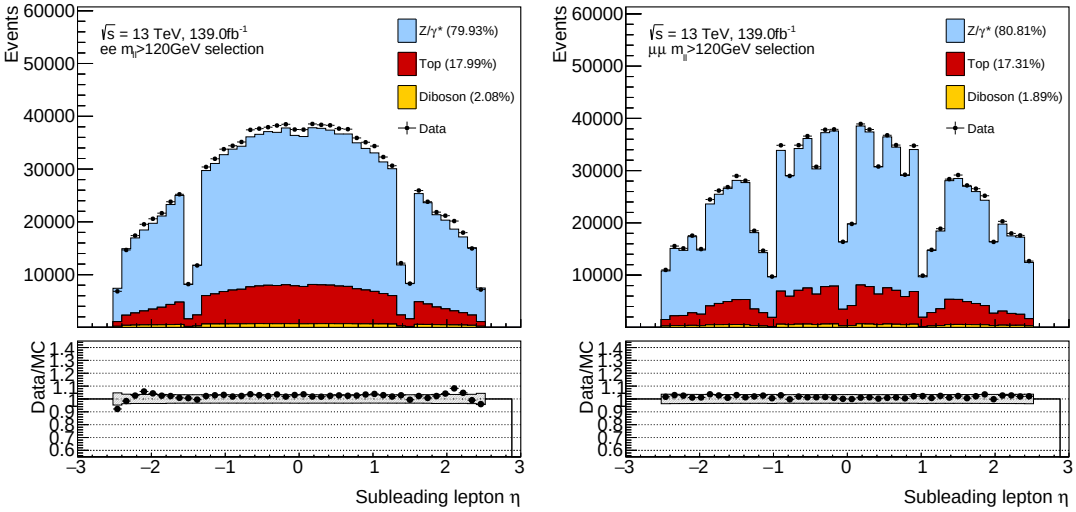

(c) ee

(d) $\mu^{\pm}\mu^{\mp}$

Figure 6.14: Comparison of η provided by background and observed data in the SR for leading (a) and subleading (c) lepton in the dielectron channel and leading (b) and subleading (d) lepton in the dimuon channel. The lower subplots show the ratio of data and MC along with systematic uncertainties related to the background.

able where there is a large background, i.e. in the lower mass regions, which certainly holds in both channels. For example, the ratio of limits when including systematics over the limits when excluding systematics (here referred to as the nominal limits) for a mass of 1 TeV is 6.3% in the electron channel and 17.5% in the muon channel for $k\overline{M}_{Pl}$. In the muon channel, however, the effect of systematics is seen throughout the whole mass

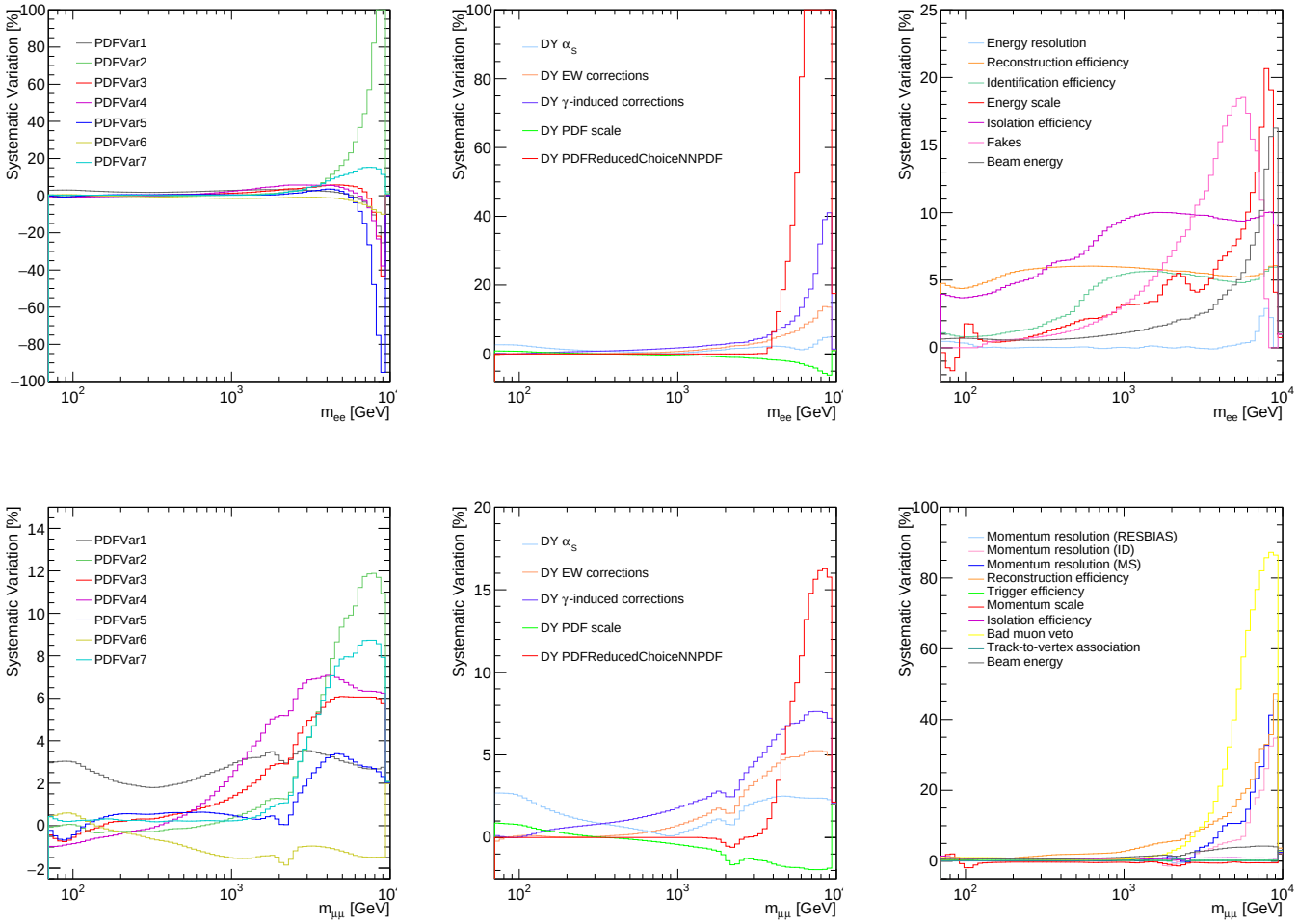

Figure 6.15: Systematic uncertainties on the total background as a function of invariant mass from different uncertainty sources in the (top) dielectron channel and (bottom) dimuon channel. The two left-most plots represent theoretical uncertainties while the right-most plot shows the experimental uncertainties.

range. This would imply that the signal systematics play a bigger role in the muon channel where the background is small. Figure 6.16 displays the difference in signal systematic contributions between the electron and muon channel for signal masses 2 and 4 TeV. For instance, when excluding only signal systematics for $m_{G^*} = 4\,\text{TeV}$ with coupling 0.1 the limit increases by 9% from not including any at all. Meanwhile, the limits decrease by 1.9% when including *only* background systematics from the nominal limits. Specifically, it is the uncertainty on the bad muon veto and efficiency uncertainties which are the biggest contributors in the high-m_{ll} regions. Although uncertainties related to the resolution are non-zero they do not alter the amount of signal events in

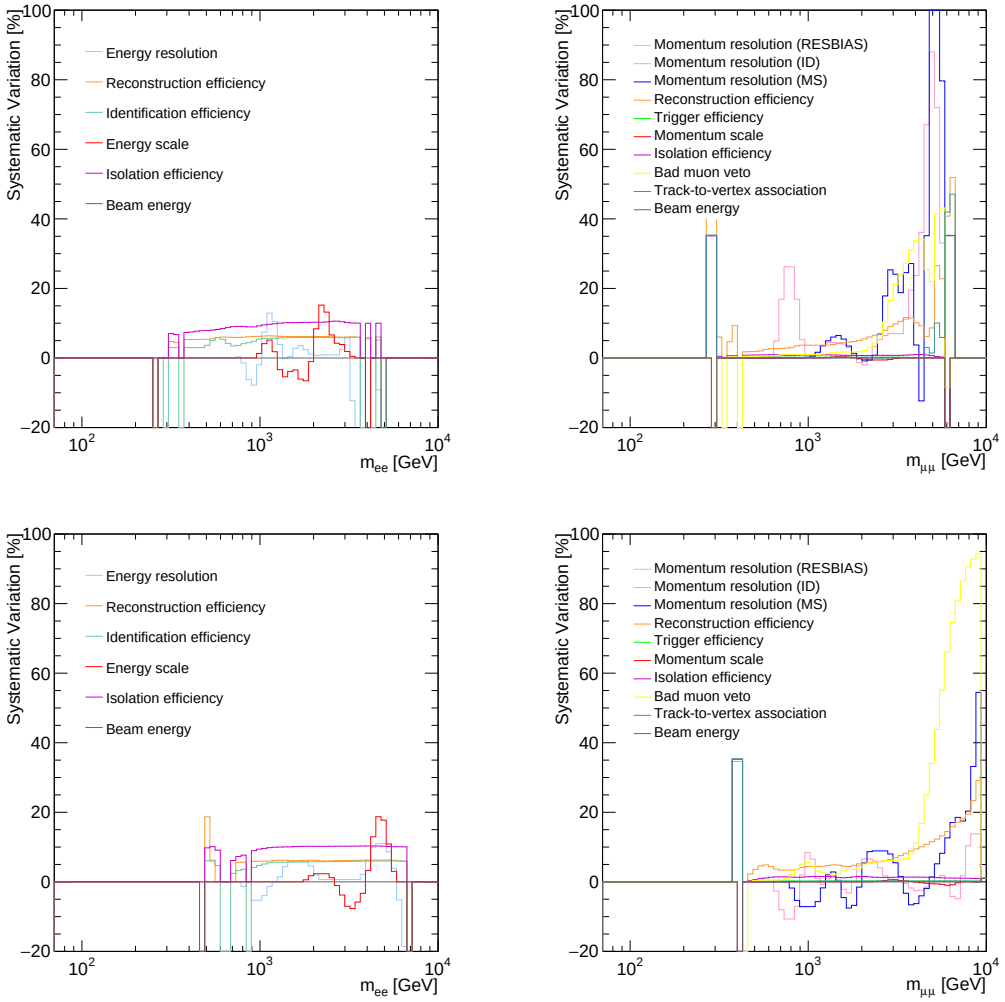

Figure 6.16: Systematic uncertainties on the (top) 2 TeV and (bottom) 4 TeV G^* signals with coupling $k/\overline{M}_{Pl} = 0.1$ as a function of invariant mass from different uncertainty sources in the (left) dielectron channel and (right) dimuon channel.

the final selection, but rather "smear" out the shape of the signal peaks.[16]. As the G^* couplings increase so too does the width of the signal resonances. The more narrow our signal peak is the more we constrain signal systematics from the side-band regions of a signal region. This could also help explain why the differences between the respective couplings from tables 6.8 to 6.7 appear to increase the greater the signal width becomes.

To ensure the cross-section limits of G^* have been produced correctly we can compare them with the limits of Z'_χ, obtained from Ref. [49], due to their similar intrinsic widths. That is, the Z'_χ displays a width of 1.2% of its mass, while the G^* with coupling 0.1

[16]Figure B.5 in Appendix B shows the total signal systematics of each coupling (per mass).

Table 6.7: Overview of expected exclusion limits produced with $L = 139\,\text{fb}^{-1}$ for $m_{G*} \in [0.75, 5.00]$ TeV without systematic uncertainties. The limits are given in fb.

$k/\overline{M}_{Pl}$	Channel	0.75 TeV	1.00 TeV	2.00 TeV	3.00 TeV	4.00 TeV	5.00 TeV
0.1	ee	0.69	0.38	0.11	0.048	0.034	0.032
	$\mu^+\mu^-$	1.26	0.77	0.21	0.10	0.073	0.067
	$ee + \mu^+\mu^-$	0.60	0.34	0.094	0.039	0.026	0.023
0.2	ee	0.97	0.54	0.13	0.056	0.038	0.035
	$\mu^+\mu^-$	1.43	0.86	0.22	0.10	0.071	0.070
	$ee + \mu^+\mu^-$	0.80	0.46	0.11	0.045	0.028	0.025
0.3	ee	1.26	0.71	0.16	0.065	0.043	0.040
	$\mu^+\mu^-$	1.41	0.92	0.25	0.11	0.081	0.076
	$ee + \mu^+\mu^-$	0.92	0.56	0.13	0.051	0.032	0.029

Table 6.8: Overview of expected exclusion limits produced with $L = 139\,\text{fb}^{-1}$ for $m_{G*} \in [0.75, 5.00]$ TeV with systematic uncertainties. The limits are given in fb.

Coupling	Channel	0.75 TeV	1.00 TeV	2.00 TeV	3.00 TeV	4.00 TeV	5.00 TeV
0.1	ee	0.73	0.40	0.11	0.048	0.035	0.032
	$\mu^+\mu^-$	1.48	0.94	0.22	0.10	0.080	0.082
	$ee + \mu^+\mu^-$	0.64	0.35	0.091	0.038	0.027	0.023
0.2	ee	1.14	0.63	0.13	0.055	0.039	0.035
	$\mu^+\mu^-$	1.83	1.11	0.23	0.11	0.076	0.086
	$ee + \mu^+\mu^-$	0.97	0.55	0.11	044	0.029	0.027
0.3	ee	1.75	0.93	0.16	0.066	0.043	0.040
	$\mu^+\mu^-$	1.94	1.25	0.25	0.12	0.090	0.091
	$ee + \mu^+\mu^-$	1.25	0.74	0.13	0.051	0.034	0.029

displays an intrinsic width of $\sim 1.4\%$ of its mass. The comparison was done using a luminosity of $36\,\text{fb}^{-1}$ to match that of the paper. It should be noted that only a direct comparison could be made for coupling $k/\overline{M}_{Pl} = 0.1$, as the limits for the Z'_χ are quoted using fiducial limits[17] for intrinsic widths greater than $0.012 m_{Z'_\chi}$. From the right-most column in table 6.9 the ratios lie relatively close to 100% for masses up to ~ 3 TeV, which indicate the exclusion limits to have been produced correctly for both channels[18]. The greater deviations seen for masses 4–5 TeV could be due to the parton-luminosity tails contained in the m_{ll}-distributions of the Z'_χ, which result in a greater overlap between signal and background compared to that of the G^*.

[17] In which one applies a mass window around the pole mass to exclude the parton-luminosity tail from the Breit-Wigner distribution in order to make an analysis more model-independent. In ref. [49] a mass window of two times the true width around the pole mass is used.

[18] The 19% difference in the ratio for $m_{G^*} = 0.75$ TeV in the dimuon channel could be due to systematic uncertainties. From figure 6.17 the difference between the limits when including vs. excluding systematic uncertainties is approximately 20% for the same mass point.

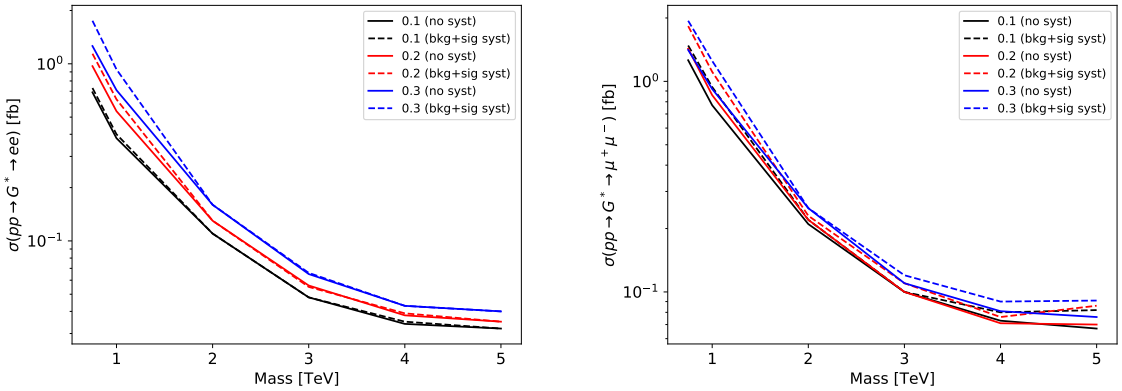

Figure 6.17: Comparison of expected limits when including systematic uncertainties for (left) dielectron and (right) dimuon channels. The solid lines show cross-section limits when ignoring systematic uncertainties, compared to the dashed lines which include systematics as nuisance parameters.

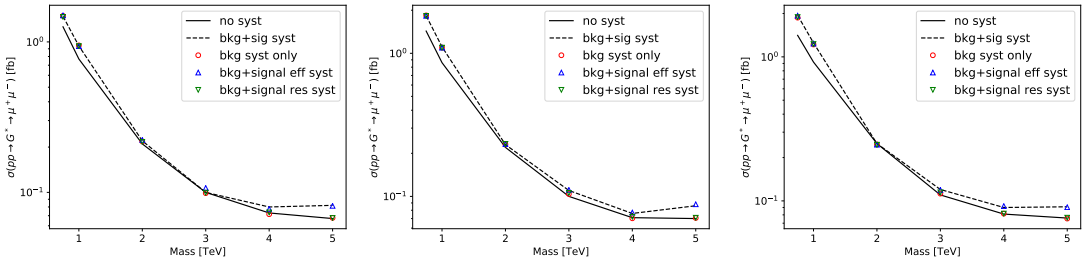

Figure 6.18: Comparison of expected limits when including systematic uncertainties for (from left to right) couplings 0.1, 0.2 and 0.3 in the dimuon channel. The solid lines show cross-section limits when ignoring systematic uncertainties, compared to the dashed lines which include systematics as nuisance parameters. The circles denote limits which have been producing when including only background systematics, the upward-facing triangles represent limits produced with both background and signal efficiency systematics, while the downward-facing triangles show limits produced with background systematics and signal resolution systematics.

Figure 6.19 shows an example of the posterior distributions when including systematic uncertainties. The posterior distributions are shown for $m_{G^*} = 2\,\text{TeV}$ with coupling 0.1 in both channels. The normal priors for the nuisance parameters contribute in the more Gaussian-like shape of the posterior distributions.

Correlation of parameters

The correlation between parameters is extracted form joint posteriors of two parameters at the same time. Figure 6.20 shows the covariance matrices in the dielectron and

Table 6.9: Overview of expected exclusion limits produced with $L = 36\,\text{fb}^{-1}$ with systematic uncertainties. Column four shows the signal acceptance×efficiency for G^* with the upper limits on the signal cross-section σ in column five. Columns six and seven show the acceptance×efficiency and upper cross-section limit for Z'_χ obtained in ref. [49]. The right-most column shows the ratio between the two limits, with (*) indicating a scaling to account for the observed difference in the acceptance×efficiency which could stem from possible improvements in the reconstruction and selections as well as possible differences in the kinematical distributions between the G^* and Z'.

Channel	Mass [TeV]	$N_{\text{sig,max}}$	*This analysis*		Z' *paper* [49]		Limit(*)/paper limit
			$A \times \varepsilon$	Limit [fb]	$A \times \varepsilon$	Limit [fb]	
ee	0.75	140	69%	1.38	61%	1.63	96%
ee	1.00	80	71%	0.74	64%	0.96	86%
ee	2.00	27	73%	0.24	70%	0.27	92%
ee	3.00	20	74%	0.15	71%	0.16	98%
ee	4.00	15	73%	0.13	69%	0.16	85%
ee	5.00	13	73%	0.12	65%	0.23	56%
$\mu^+\mu^-$	0.75	200	50%	3.10	38%	3.43	119%
$\mu^+\mu^-$	1.00	120	49%	1.73	40%	2.07	102%
$\mu^+\mu^-$	2.00	35	48%	0.49	41%	0.56	102%
$\mu^+\mu^-$	3.00	25	46%	0.28	39%	0.34	96%
$\mu^+\mu^-$	4.00	17	44%	0.25	37%	0.35	83%
$\mu^+\mu^-$	5.00	15	41%	0.27	34%	0.58	56%

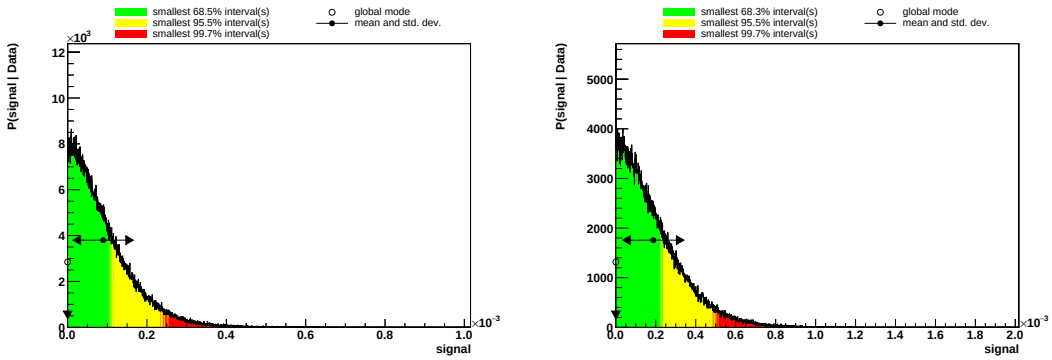

Figure 6.19: Expected posterior density distributions for $m_{G^*} = 2\,\text{TeV}$ with coupling $k/\overline{M}_{Pl} = 0.1$ at $L = 36\,\text{fb}^{-1}$, in the (left) dielectron channel and (right) dimuon channel. The signal cross-section σ (denoted as "signal") is given in pb. The upper limit is defined as the boundary between two and three standard deviations, i.e. 95% and 99.7% quantiles, such that there is less than a 5% probability that $\sigma > \sigma_{up}$.

dimuon channels. The labels on the x-axes are mirroring the labels on the y-axes, which is reflected by the fully correlated elements along the diagonal. Among the nuisance parameters themselves, the first PDF variation (PDF_VAR1) and α_S (ALPHAS) is

correlated by ~ -0.8 in the dielectron channel and ~ -0.6 in the dimuon channel. In other words, the variations of the two parameters move in opposite directions of one another. In the dimuon channel the reconstruction efficiency (EFF_RECO) and the "bad muon" uncertainty is correlated by ~ 0.4, meaning the increase in variations of one slightly increases the variations of the other.

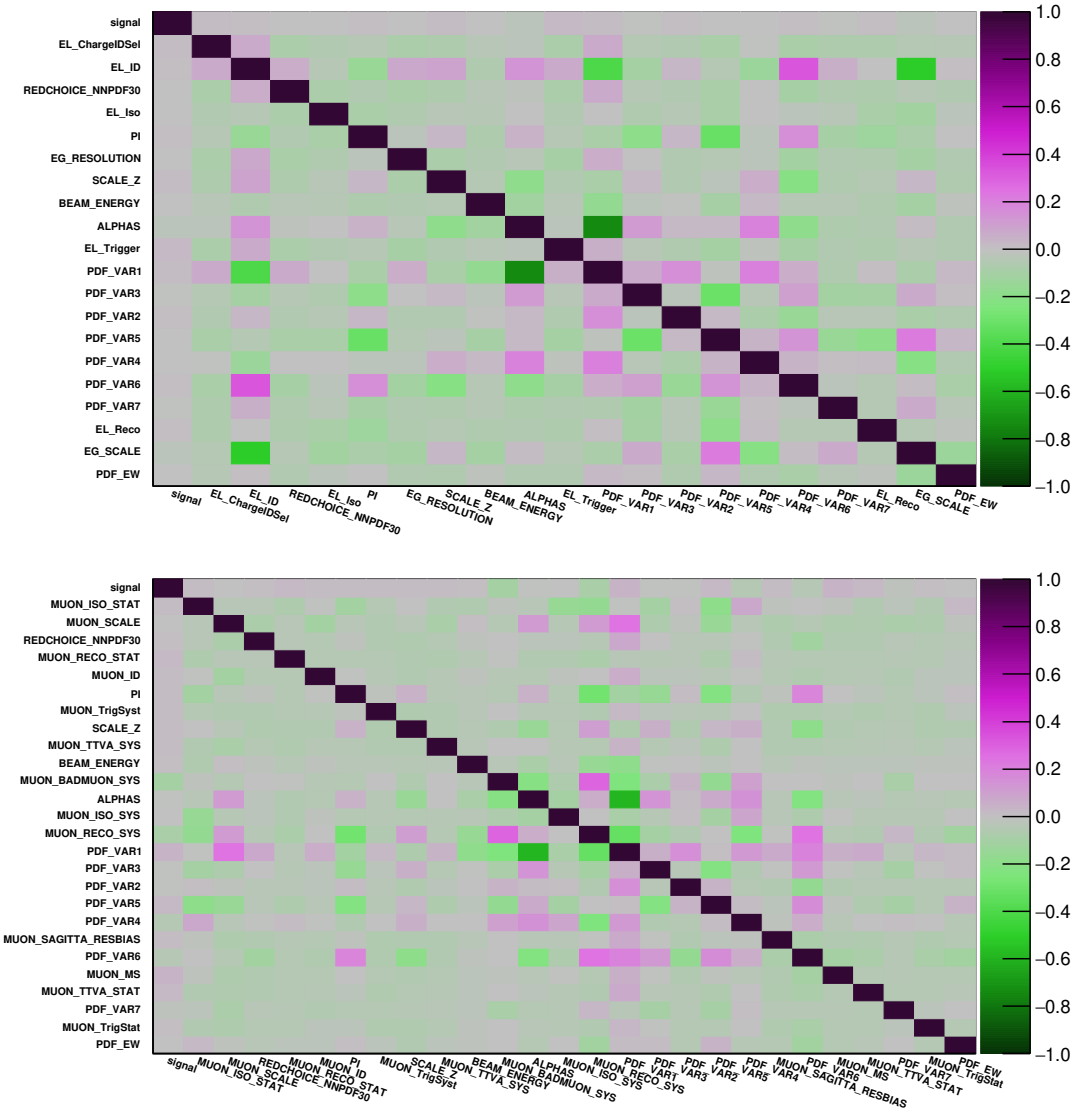

Figure 6.20: Correlation matrices for the (top) dielectron and (bottom) dimuon channels for the signal $m_{G^*} = 2\,\text{TeV}$ with coupling 0.1.

Expected limits from ensembles

If we are interested in the sensitivity of an experiment, we can create ensembles of cross-section limits estimated from *pseudo-experiments*. That is, we create pseudo-data by repeating the procedure described in subsection 5.1.2 a given number of times N. For each pseudo-experiment we draw a random number of "observed" events from a Poisson distribution with an expectation value b_{kl} from bin l of channel k. In addition, sample values for the nuisance parameters are drawn according to a Gaussian distribution. The expected limit, quoted as the median of the distribution of cross-section limits, and the 68% and 95% quantiles are then calculated.

Figure 6.21 shows an example of how the extracted limits, computed from the medians of 10 and 400 pseudo-experiments, and quantiles become more precise as the number of pseudo-experiments increase. The expected (observed) mass limits are then extracted as the intersections between the theoretical and the expected (observed) cross-sections. This is done using an interpolation between the given mass points. The intersection is extracted from a linear extrapolation if the intersection point exceeds the final mass point.

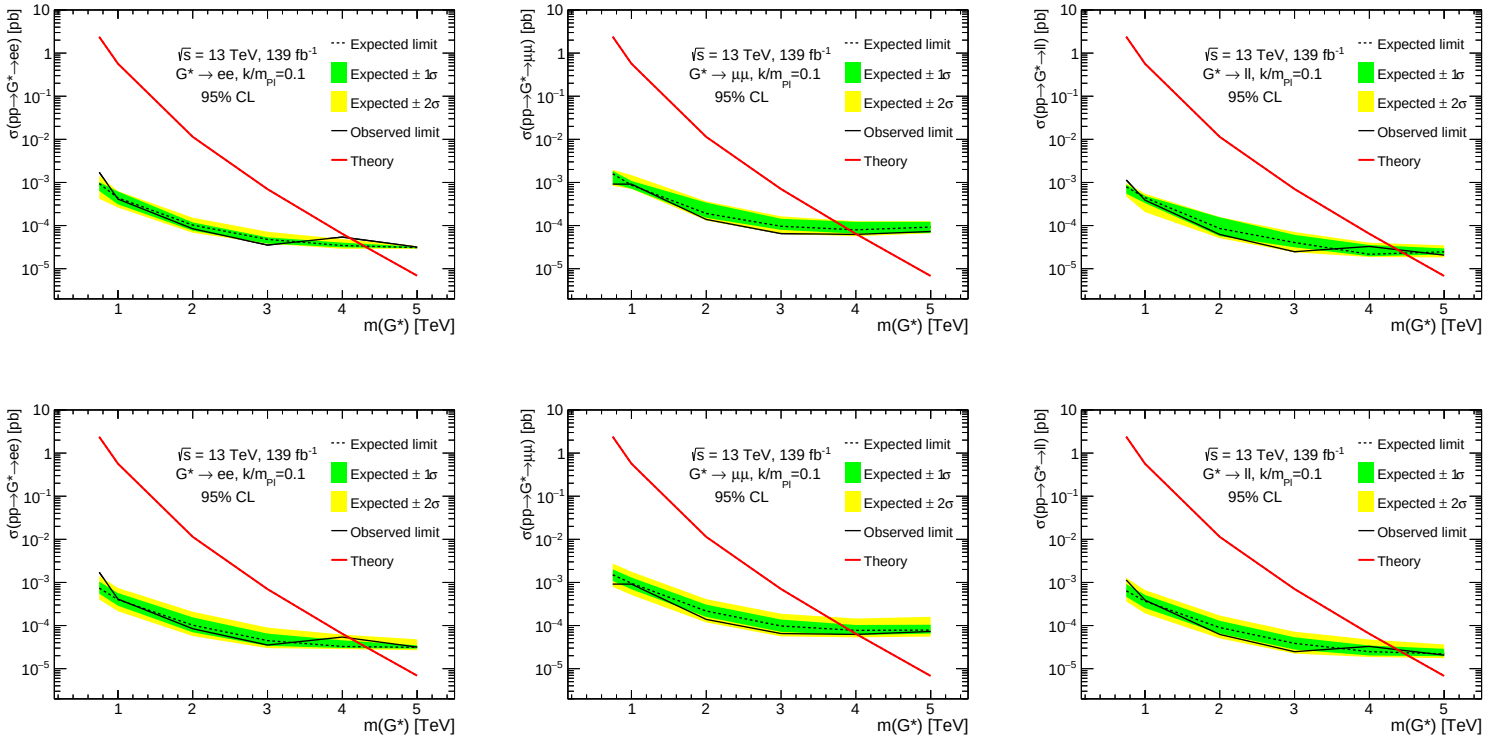

Figure 6.21: Comparison of expected cross-section limits and quantiles extracted from (top) 10 and (bottom) 400 pseudo-experiments for coupling $k/\overline{M}_{Pl} = 0.1$ in the (from left to right) dielectron, dimuon and dilepton channels.

Chapter 7

Final Results

The observed and expected invariant mass distributions in the dielectron and dimuon channels from figure 7.1 appear to be in good agreement with each other. We see slight statistical deviations between some data points and the background expectation towards the tails ($m_{ll} > 2\,\text{TeV}$), but due to the number of events in each bin being less than 10 these deviations could merely be statistical fluctuations.

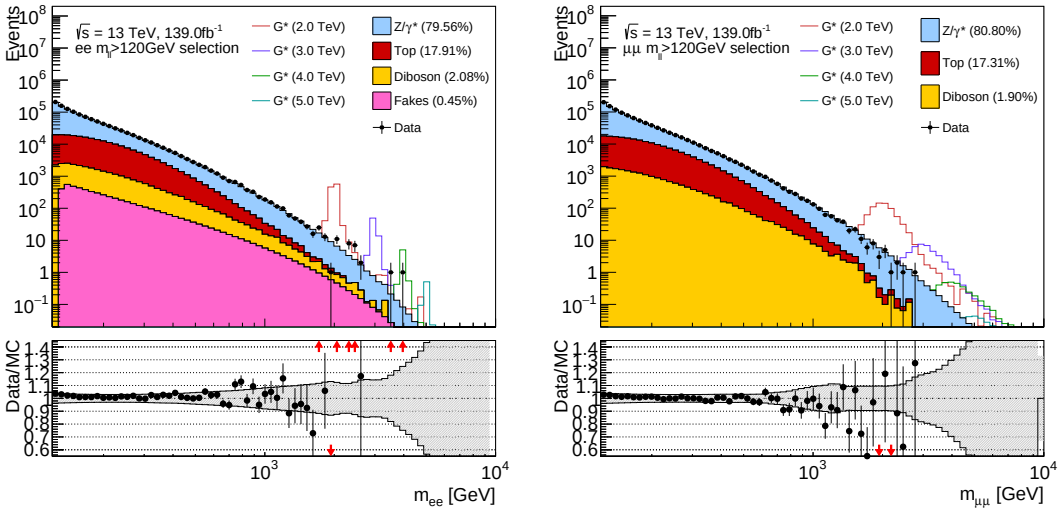

(a) ee (b) $\mu^{\pm}\mu^{\mp}$

Figure 7.1: Comparison of invariant mass distributions provided by background and observed data in the mass range $120 \leq m_{ll} \leq 10\,000\,\text{GeV}$ for the (a) dielectron channel and (b) dimuon channel in the upper subplot, and corresponding ratio of data over background for a given bin in the lower subplot. Signals $m_{G^*} = 2, 3, 4$ and $5\,\text{TeV}$ with coupling 0.1 are also shown.

The maximum number of pseudo-experiments used for the production of exclusion limits and quantiles in this analysis is 950. Table 7.1 shows the expected and observed

95% C.L. lower limits for the graviton mass for couplings $k/\overline{M}_{Pl} = 0.1$–$0.3$ in each channel, with corresponding upper cross-section limits in table 7.2. Figure 7.2 shows the cross-section limits with $\pm 1\sigma$ and $\pm 2\sigma$ bands. The lower mass limits are extracted from the intersection between the theoretical signal cross-sections with the expected and observed signal cross-sections computed from the posterior marginalisation[1]. Figure 7.3 shows examples of the expected and observed distributions of $P(\sigma|\mathbf{n})$, at which the upper cross-section is extracted from, at $m_{G^*} = 2\,\text{TeV}$ for coupling $k/\overline{M}_{Pl} = 0.1$.

Table 7.1: The expected and observed 95% C.L. lower mass limits, given in TeV, on G^* using 950 pseudo-experiments for the expected limits (in this analysis). A comparison for coupling 0.1 is given by the recent CMS publication [50].

	Channel	$k/\overline{M}_{Pl} = 0.1$		$k/\overline{M}_{Pl} = 0.2$		$k/\overline{M}_{Pl} = 0.3$	
		Exp.	Obs.	Exp.	Obs.	Exp.	Obs.
Analysis	ee	4.31	4.10	4.96	4.91	5.38	5.27
	$\mu^+\mu^-$	3.92	4.01	4.57	4.64	4.90	4.98
	$ee + \mu^+\mu^-$	4.44	4.38	5.09	5.11	5.46	5.40
CMS	ee	4.43	4.42	–	–	–	–
	$\mu^+\mu^-$	4.59	4.59	–	–	–	–
	$ee + \mu^+\mu^-$	4.81	4.78	–	–	–	–

The difference in the lower limits on m_{G^*} between this analysis and the CMS paper could perhaps stem from different values used for the free parameters, such as α_s, giving different cross-sections. This could be cross-checked by comparing the theoretical cross-sections computed by ATLAS to those computed by CMS[2]. It could also be due to differences in the resolution. For muons, the differences between this analysis and the CMS limits are enhanced in the dimuon channel, which could be a result of the greater magnetic field in the CMS detector providing a better muon momentum resolution than the ATLAS detector. Although not as pronounced, it could also be due to the parton-luminosity tails, as discussed in subsection 6.4.2. The signal distributions produced in the analysis contain parton-luminosity tails in the lower m_{ll} regions where the background levels are much higher compared to the higher m_{ll} regions. The tails increase for increasing widths, thus it is also reasonable to suspect that the limits produced are somewhat weaker than if we were to use fiducial limits instead. Additionally, the effects of systematics between the ATLAS and CMS detector cannot be ruled out.

Current experimental outlook

Previous searches [27, 52, 50] at $\sqrt{s} = 8\,\text{TeV}$ and $\sqrt{s} = 13\,\text{TeV}$ found no significant excess and led to the observed mass limits of the lightest KK-mode of the RS graviton at variable couplings $k/\bar{M}_{Pl} \in [0.01, 0.2]$. The mass limits produced with $\sqrt{s} = 13\,\text{TeV}$, with a corresponding integrated luminosity of $L = 140\,\text{fb}^{-1}$, are the most stringent to

[1] Expressed in eq. (5.11) in subsection 5.1.2

[2] These are for the moment not given in HEPDATA [51].

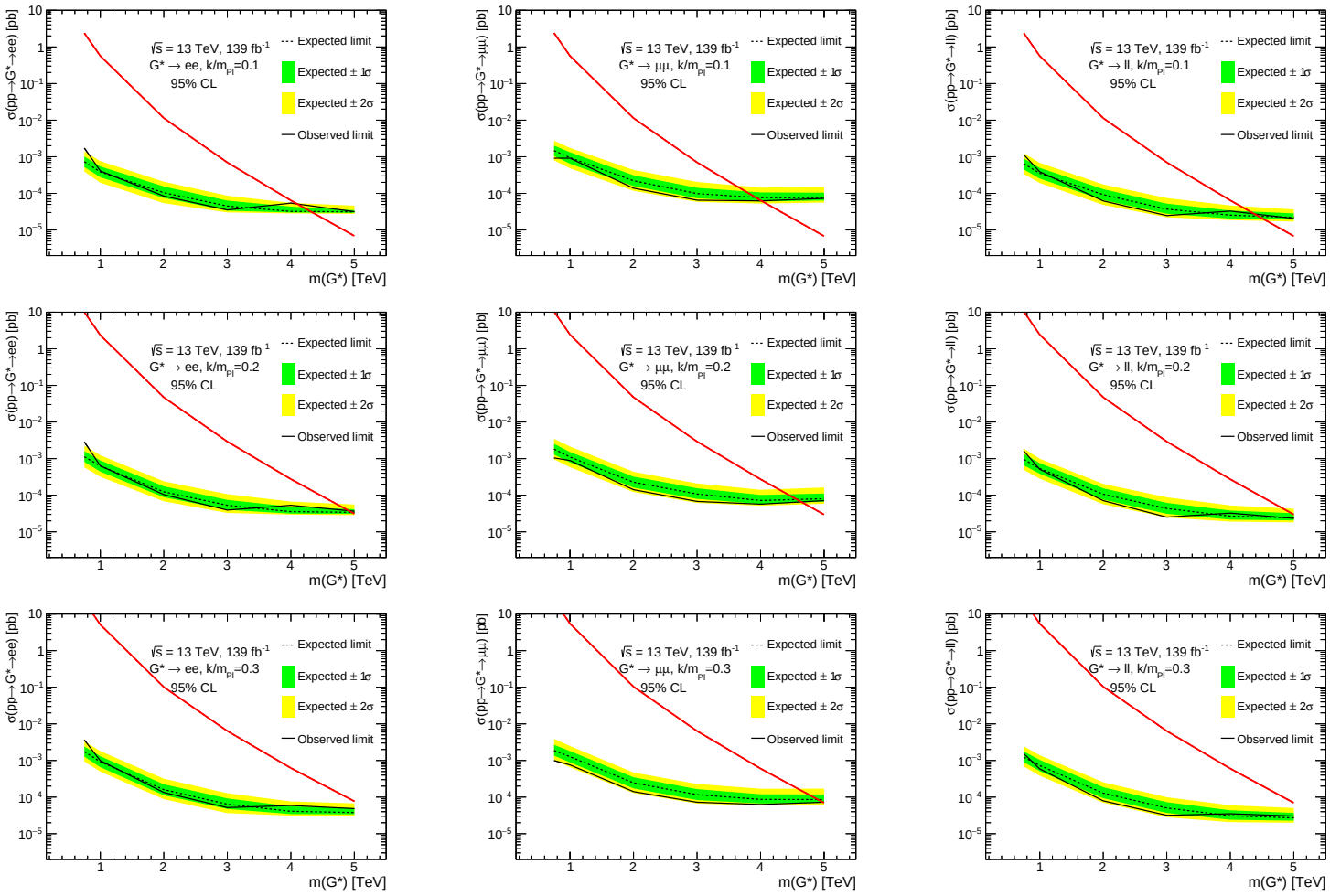

Figure 7.2: The expected and observed 95% C.L. upper cross-section limits, given in pb, on G^* for couplings 0.1–0.3 (top to bottom) in the (left) dielectron, (middle) dimuon and (right) dilepton channels.

date, in which a spin-2 resonance is excluded at 95% C.L. for masses below 4.78 (2.47) for coupling parameter $k/\overline{M}_{Pl} = 0.1$ (0.01) [50]. These are shown in table 7.3.

Table 7.2: The expected and observed 95% C.L. upper cross-section limits, given in fb, at the G^* mass corresponding to the mass limits from table 7.1 using 950 pseudo-experiments for the expected limits.

Channel	$k/\overline{M}_{Pl} = 0.1$		$k/\overline{M}_{Pl} = 0.2$		$k/\overline{M}_{Pl} = 0.3$	
	Exp.	Obs.	Exp.	Obs.	Exp.	Obs.
ee	4.63e-02	5.85e-02	4.16e-02	5.32e-02	4.03e-02	5.10e-02
$\mu^+\mu^-$	1.14e-01	6.36e-02	1.34e-01	1.17e-01	1.21e-01	7.90e-02
$ee + \mu^+\mu^-$	3.90e-02	4.27e-02	2.59e-02	2.48e-02	2.68e-02	3.20e-02

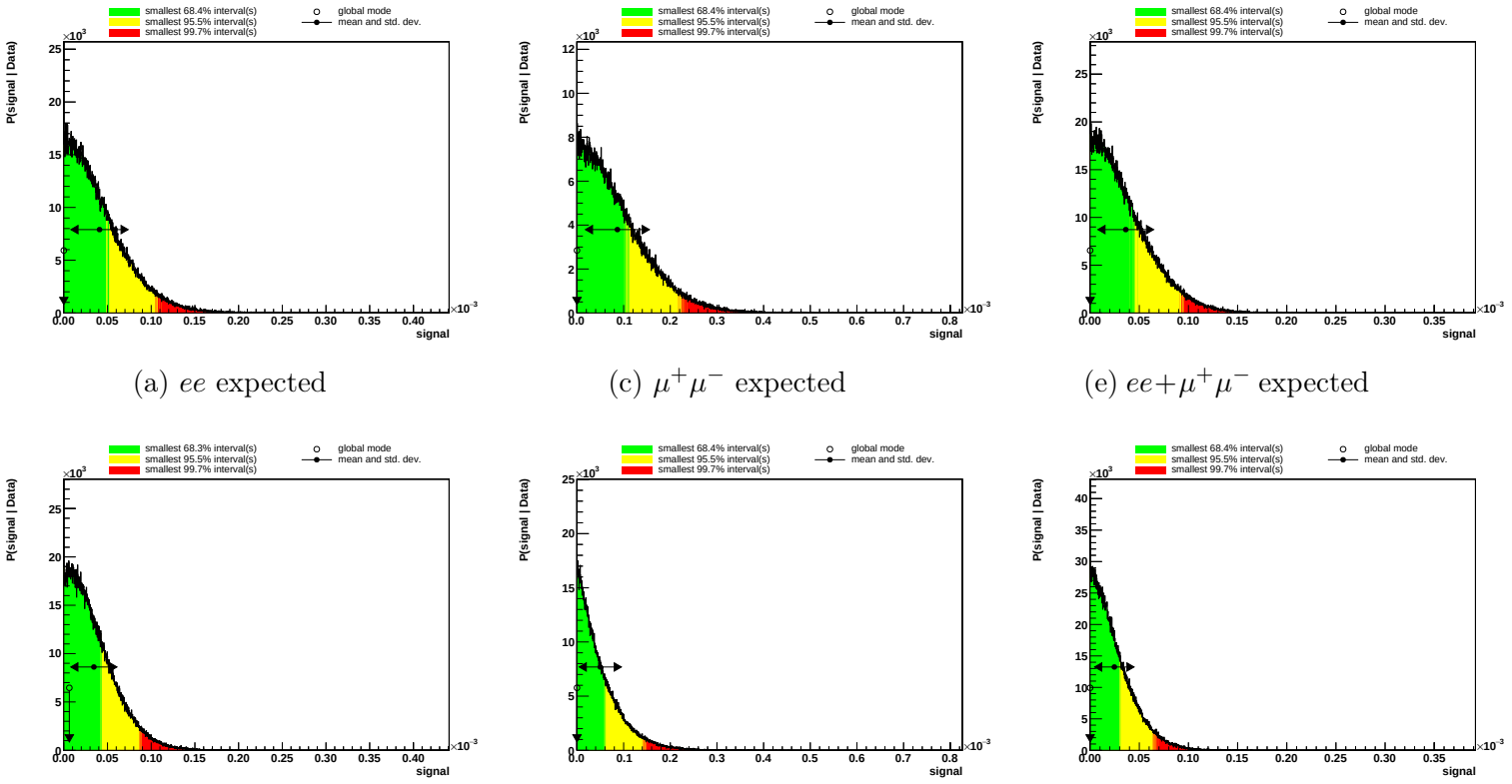

(a) ee expected (c) $\mu^+\mu^-$ expected (e) $ee+\mu^+\mu^-$ expected

(b) ee observed (d) $\mu^+\mu^-$ observed (f) $ee+\mu^+\mu^-$ observed

Figure 7.3: Examples of posterior distributions using $m_{G^*} = 2\,\text{TeV}$ with $L = 139\,\text{fb}^{-1}$ and coupling $k/\overline{M}_{Pl} = 0.1$ in the (a-b) dielectron, (c-d) dimuon and (e-f) dilepton channels.

Table 7.3: The observed and expected 95% C.L. lower limits on the masses of G^* (m_{G^*}) from a center-of-mass energy $\sqrt{s} = 8\,\text{TeV}$ (ATLAS) [27], and $\sqrt{s} = 13\,\text{TeV}$ (CMS) at $L = 36\,\text{fb}^{-1}$ [52] and $L = 140\,\text{fb}^{-1}$ [50]. The couplings $k/\overline{M}_{Pl}$ are shown in the top row, with corresponding expected limits (Exp.) and observed limits (Obs.) from the second row. N/A indicates that a signal with such coupling was not considered in the analysis.

$\sqrt{s}$	L	Channel	0.01		0.03		0.05		0.1		0.2	
			Exp.	Obs.	Exp.	Obs.	Exp.	Obs.	Exp.	Obs.	Exp.	Obs.
13 TeV	$36\,\text{fb}^{-1}$	ee	1.85	1.85	N/A	N/A	3.30	3.30	3.90	3.90	N/A	N/A
13 TeV	$137\,\text{fb}^{-1}$	ee	2.29	2.16	N/A	N/A	3.83	3.70	4.43	4.42	N/A	N/A
13 TeV	$36\,\text{fb}^{-1}$	$\mu^+\mu^-$	2.00	2.05	N/A	N/A	3.50	3.50	4.05	4.05	N/A	N/A
13 TeV	$140\,\text{fb}^{-1}$	$\mu^+\mu^-$	2.32	2.34	N/A	N/A	3.96	3.96	4.59	4.59	N/A	N/A
13 TeV	$36\,\text{fb}^{-1}$	$ee + \mu^+\mu^-$	2.05	2.10	N/A	N/A	3.60	3.65	4.25	4.25	N/A	N/A
13 TeV	$140\,\text{fb}^{-1}$	$ee + \mu^+\mu^-$	2.53	2.47	N/A	N/A	4.19	4.16	4.81	4.78	N/A	N/A
8 TeV	$20\,\text{fb}^{-1}$	$ee + \mu^+\mu^-$	1.28	1.25	1.95	1.96	2.25	2.28	2.67	2.68	3.05	3.05

Conclusion and Future Work

Conclusion

A search for the lightest Kaluza-Klein graviton mode G^* in the dilepton final state using the framework of extra dimensions, described by the Randall-Sundrum model, has been presented. Data collected from proton-proton collisions at $\sqrt{s} = 13\,\text{TeV}$ using the ATLAS detector at the LHC was used for the analysis. This data was extracted from three sub-runs of the LHC during its Run 2 period, each with different integrated luminosities. The total integrated luminosity of $L = 139\,\text{fb}^{-1}$ consists of run a with $L = 36.2\,\text{fb}^{-1}$ (2015-2016), run d with $L = 44.3\,\text{fb}^{-1}$ (2017) and run e with $L = 58.4\,\text{fb}^{-1}$ (2018). Only the opposite-sign channel was considered for muons due to negligible statistics from the same-sign channel. The same could not be said for the electron-channel due to charge-misidentification and thus both the same-sign and opposite-sign channels are considered in order to not lose non-negligible signals. The signal region was set for invariant masses above 120 GeV, thereby vetoing the Z-peak. The simulated background (SM DY, top and diboson processes) and data were in good agreement with each other in the high-statistics regions.

The Randall-Sundrum graviton excitation G^* is described by two free parameters; its mass and coupling strength $k/\overline{M}_{Pl}$. The six available G^* mass points considered in this thesis ranged between 0.75 TeV and 5 TeV, and were all given for the three coupling strengths 0.1, 0.2 and 0.3. Exclusion limits at 95% C.L. for the mass of the G^* were therefore computed with respect to each coupling both in the electron, muon and combined channels. The effects of systematic uncertainties on the limits were also studied. Background systematics play a significant role where the background is large, typically in the lower mass regions. Uncertainties arising from signal systematics related to efficiencies in the muon channel, such as the reconstruction and identification efficiencies, also played a role in the limit setting at higher invariant masses. Masses up to 4.10 TeV, 4.01 TeV and 4.38 TeV in the electron, muon and combined channels, respectively, are excluded at 95% C.L. for coupling 0.1. For coupling 0.2, masses less than 4.91 TeV, 4.64 TeV and 5.11 TeV are excluded in the electron, muon and combined channels, respectively. Lastly, masses less than 5.27 TeV, 4.98 TeV and 5.40 TeV are excluded for coupling 0.3 in the electron, muon and combined channels, respectively.

Future work

The exclusion limits presented in this analysis leave room for the possibility of detecting a graviton signal in the data above the given mass limits. However, even if a signal peak was present in the data we cannot be truly certain if the resonance stems from a Kaluza-Klein graviton signal. It might as easily be from a potential Z'-boson or a scalar resonance. As was briefly mentioned in Chapter 2.2.3, the graviton displays a spin-2 angular distribution, whereas the Z' would display a spin-1 angular distribution. We can differentiate between a graviton signal and other beyond the SM physics by looking at the angular distributions in the center-of-mass frame. This would be interesting to look further into, as it can provide more insight into potential signal resonances with masses beyond the exclusion limits.

Furthermore, theoretical variations of the Randall-Sundrum model imply different search strategies. For instance, the RS2 model takes into account the TeV-brane being embedded in an infinite extra spatial dimension. This results in Kaluza-Klein partners localized not only close to the TeV-brane, but also arbitrarily lighter KK-modes further out along the fifth dimension. An experimental implication is then that the favoured decay of TeV KK-particles is to yet lighter, non-visible KK-modes, thereby appearing as missing energy in the detector.

Additionally, there is no requirement for Standard Model particles, including gauge bosons, to solely be localized to the TeV-brane. In fact, the Standard Model particles can also propagate in the five-dimensional bulk, so long as the Higgs boson is localized on the TeV-brane, in order to maintain a solution to the hierarchy problem. This is with the requirement that the two branes act as boundaries to the bulk, as discussed in the RS1 model, and that the size of the extra dimension be relatively small. In this variation, the graviton is predicted to decay primarily via top-quarks, changing the search strategy quite drastically.

Of course, the Randall-Sundrum model is not the only candidate trying to provide a solution to the hierarchy problem. If no experimental advances to this specific model are made, then it is simply an indication that we should look elsewhere, because "new physics" is just that, it's new. It is unknown, enthralling and playful, situated right at the frontiers. And with the experimental equipment available today, we can push the boundaries of physics even further.

Appendices

Appendix A

A note on General Relativity

This short note is meant as a simple attempt to bring about a few fundamental concepts used within general relativity, with the purpose of supplementing some intuition behind the few variables mentioned in this thesis. The reader is referred to Ref. [53] by Sean M. Carroll for a much more detailed and rigorous explanation of the variables and their applications. This note is based upon the lecture notes from said author [54].

The metric tensor

Before we jump into one of the key concepts of general relativity, curvature in spacetime, we shall have a brief look at a mathematical property used to calculate physical distances. When describing the distance between two points in spacetime we use the line element ds^2, expressed in Cartesian coordinates as

$$ds^2 = -dt^2 + dx^2 + dy^2 + dz^2. \tag{A.1}$$

We can simplify the expression for ds^2 by collecting the coefficients of the spacetime coordinates into a table denoted the *metric* $g_{\mu\nu}$, that is

$$ds^2 = g_{00}dx^0dx^0 + g_{11}dx^1dx^1 + g_{22}dx^2dx^2 + g_{33}dx^3dx^3 = g_{\mu\nu}dx^\mu dx^\nu. \tag{A.2}$$

In short, the metric, $g_{\mu\nu} = \text{diag}(-1, 1, 1, 1)$, is a powerful tool giving us the necessary information to calculate physical distances along a curved path through the sum of infinitesimal path lengths ds along a trajectory. The metric tensor expressed here describes a flat spacetime, which has no curvature. The metric changes according to the geometry of the surface it describes. E.g. the metric of a sphere in two dimensions is $g_{\mu\nu} = \text{diag}(r^2, r^2\sin^2\theta)$ in which the line element takes the form $ds^2 = r^2d\theta^2 + r^2\sin^2\theta d\phi^2$.

Curvature in spacetime

Contrary to our daily experience of being on a seemingly flat surface, the geometry of spacetime can be bent. The curvature of spacetime reveals itself in the effect it has on

moving bodies, and manifests itself in what we call "gravity"[1]. We can determine the curvature of a surface using the *Riemann curvature tensor*, expressed as

$$R^{\rho}_{\sigma\mu\nu} = \partial_{\mu}\Gamma^{\rho}_{\nu\sigma} - \partial_{\nu}\Gamma^{\rho}_{\mu\sigma} + \Gamma^{\rho}_{\mu\lambda}\Gamma^{\lambda}_{\mu\sigma}, \tag{A.3}$$

where the Christoffel symbols $\Gamma^{\kappa}_{\alpha\beta}$ are identified from the metric tensor,

$$\Gamma^{\kappa}_{\alpha\beta} = \frac{1}{2}g^{\kappa\rho}(\partial_{\alpha}g_{\rho\beta} + \partial_{\beta}g_{\rho\alpha} - \partial_{\rho}g_{\alpha\beta}). \tag{A.4}$$

The Riemann tensor provides a tool to calculate the curvature of a surface in all possible directions. However, it also proves tedious to calculate due to the number of components it contains. Two other mathematical objects which also encapsulate the curvature, but perhaps in a more gentle manner, are the *Ricci tensor* (the contraction of the Riemann tensor),

$$R_{\mu\nu} = R^{\lambda}_{\mu\lambda\nu}, \tag{A.5}$$

and the *Ricci scalar*,

$$R = R^{\mu}R_{\mu} = g^{\mu\nu}R_{\mu\nu}. \tag{A.6}$$

The Ricci tensor represents the changing of volume along a curved surface[2], while the Ricci scalar tells us the average curvature along a surface. If there is no curvature present then both the Ricci tensor and the Ricci scalar is zero. The greater the curvature is, the greater the Ricci tensor and scalar become.

[1] For example, if we were to place two objects at a distance from each other along the equator of the Earth, the two objects would move closer and closer together as they simultaneously move towards a common pole, whether it be the North or South. This is due to Earth's spherical shape.

[2] E.g. if two objects were to move simultaneously from the equator to a common pole, any volume between the two objects would decrease due to the curvature of the Earth.

Appendix B

Systematics

The ratio of systematic uncertainties over the total background is shown in figures B.1–B.4, while the ratio of the sum of signal systematic uncertainties over the total signal yield is shown in figure B.5. The nuisance parameters included in this analysis are listed below.

Experimental systematics

- Electron energy resolution
- Muon momentum resolution (ID, MS, RESBIAS)
- Electron identification efficiency
- Lepton reconstruction efficiency
- Lepton isolation efficiency
- Lepton trigger efficiency
- Electron energy scale
- Beam energy scale
- Muon momentum scale
- Misidentified electrons (fakes)
- "Bad muon" veto
- Muon track-to-vertex association

Theoretical systematics

- α_s and EW higher-order corrections
- Photon-induced effect
- PDF variations, PDF scale, PDF choice

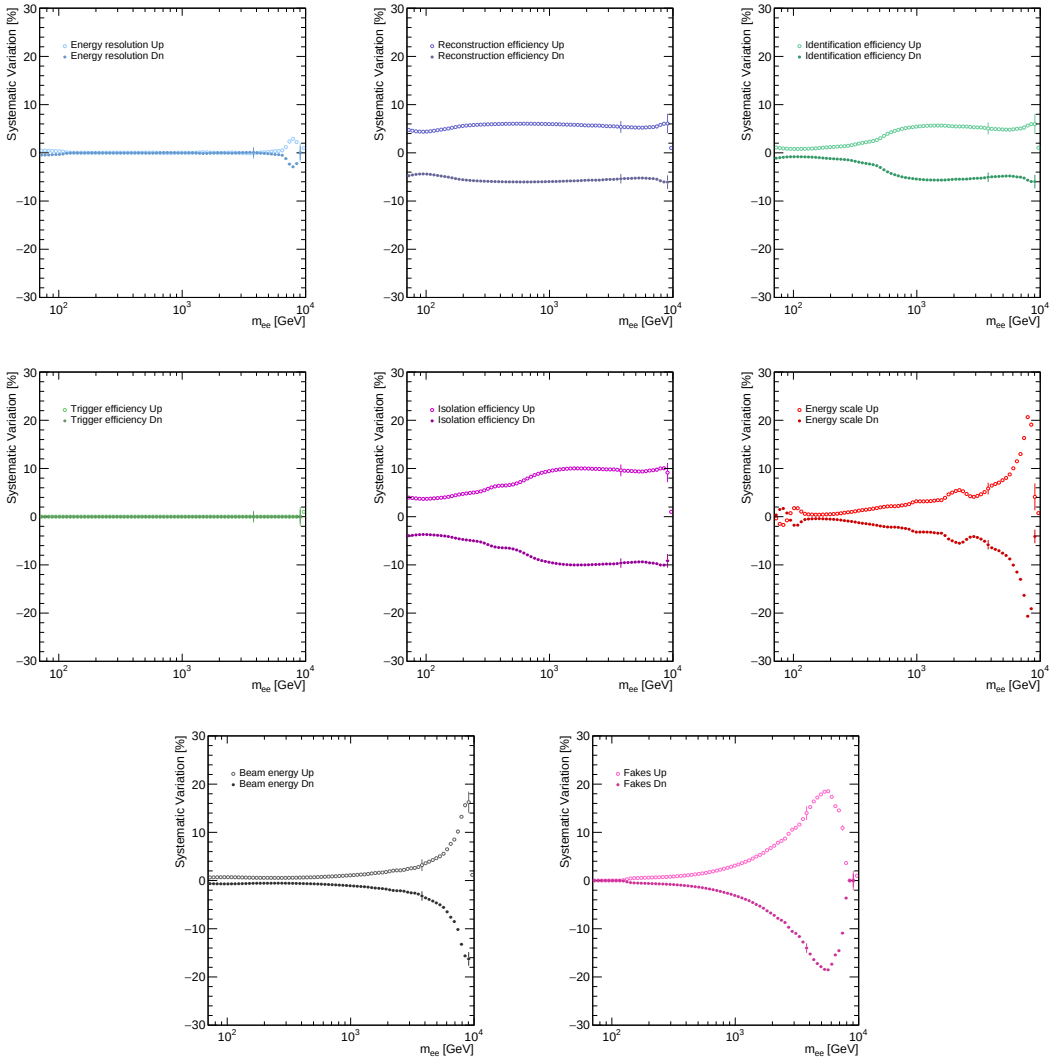

Figure B.1: Experimental background systematics in dielectron channel for $\sqrt{s} = 13\,\text{TeV}$.

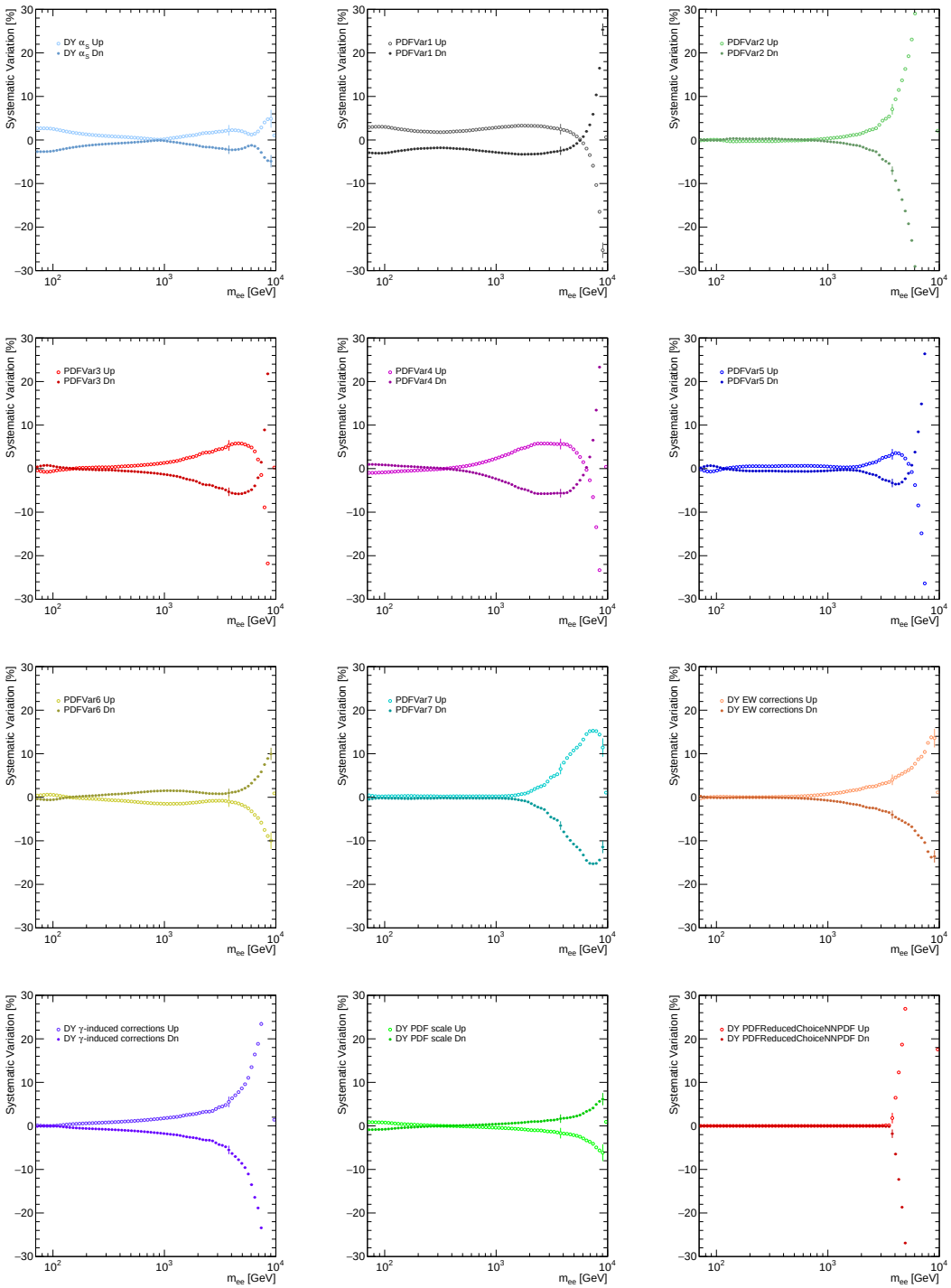

Figure B.2: Theoretical background systematics in dielectron channel for $\sqrt{s} = 13\,\text{TeV}$.

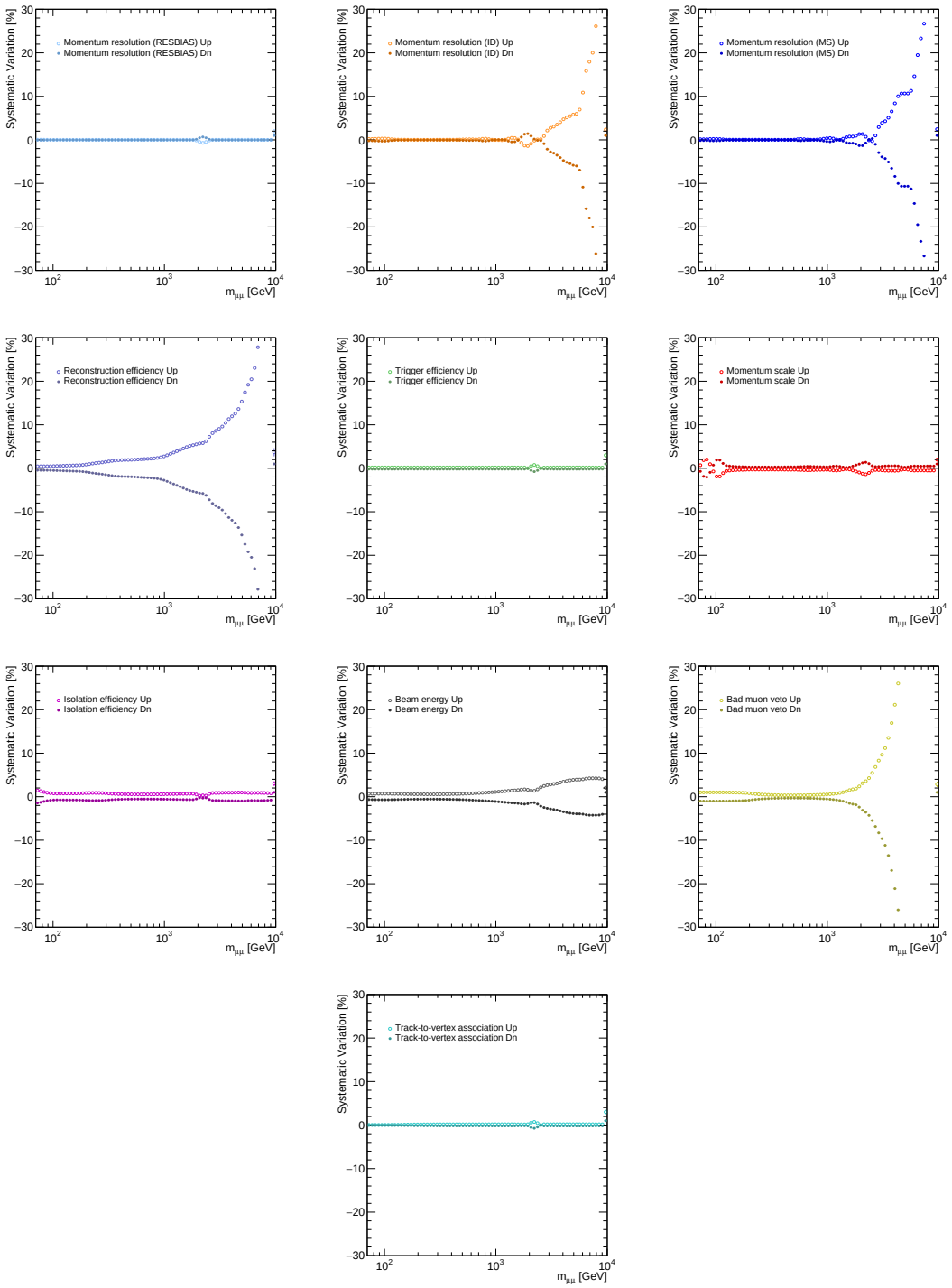

Figure B.3: Experimental background systematics in dimuon channel for $\sqrt{s} = 13\,\text{TeV}$.

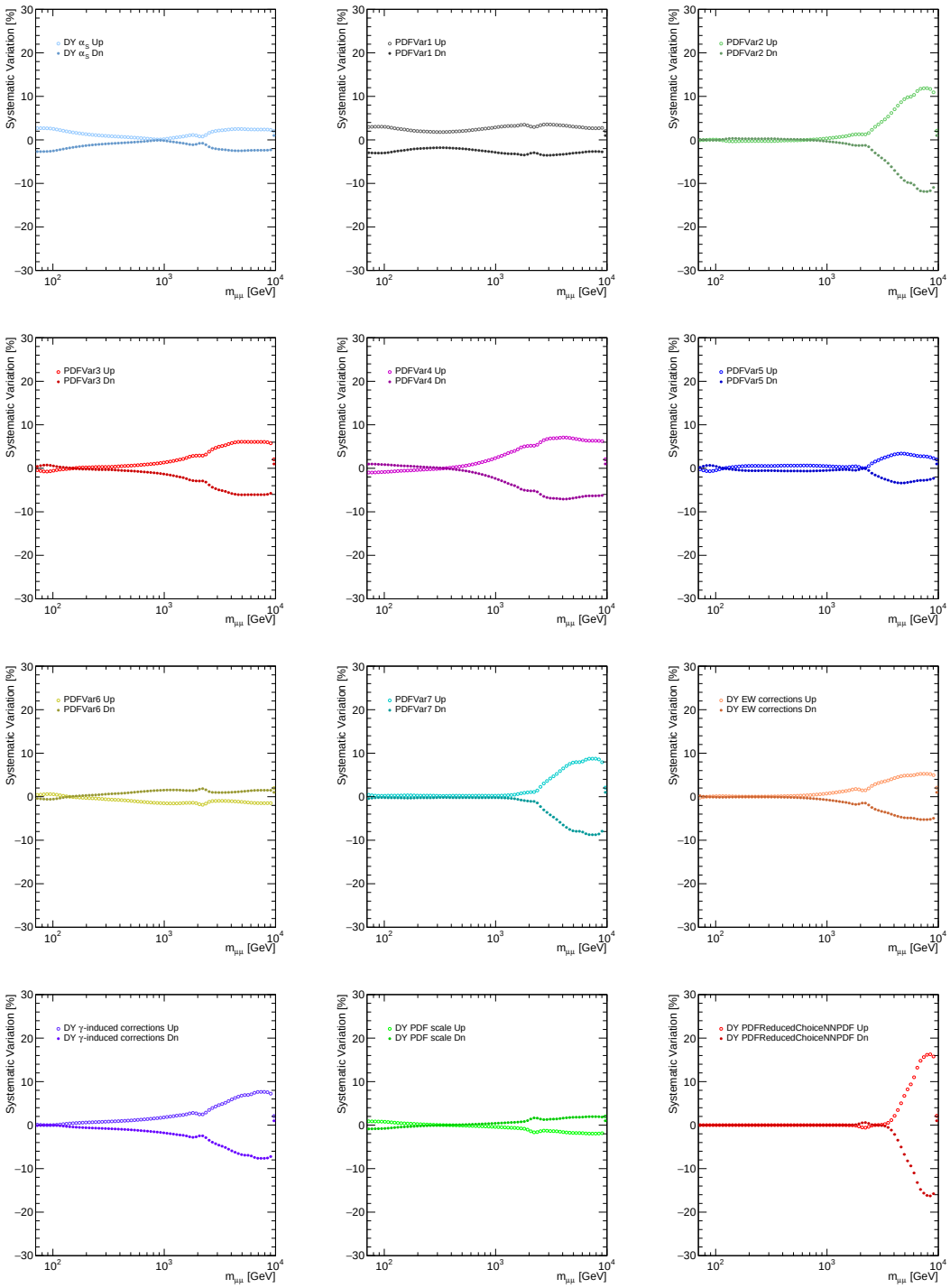

Figure B.4: Theoretical background systematics in dimuon channel for $\sqrt{s} = 13\,\text{TeV}$.

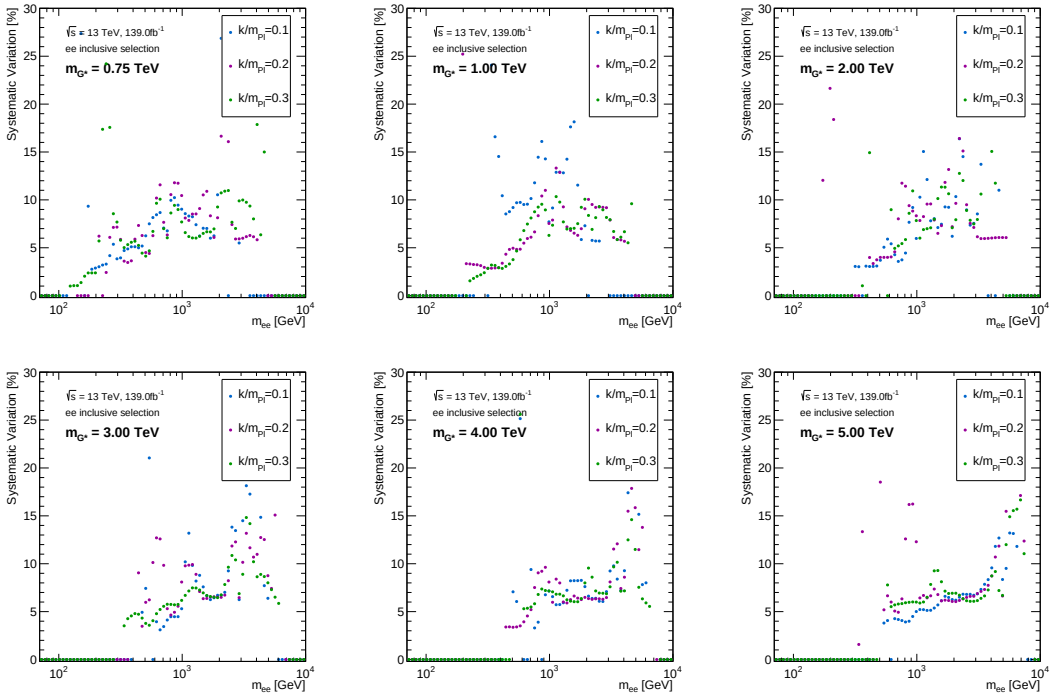

(a) Signal systematics in dielectron channel.

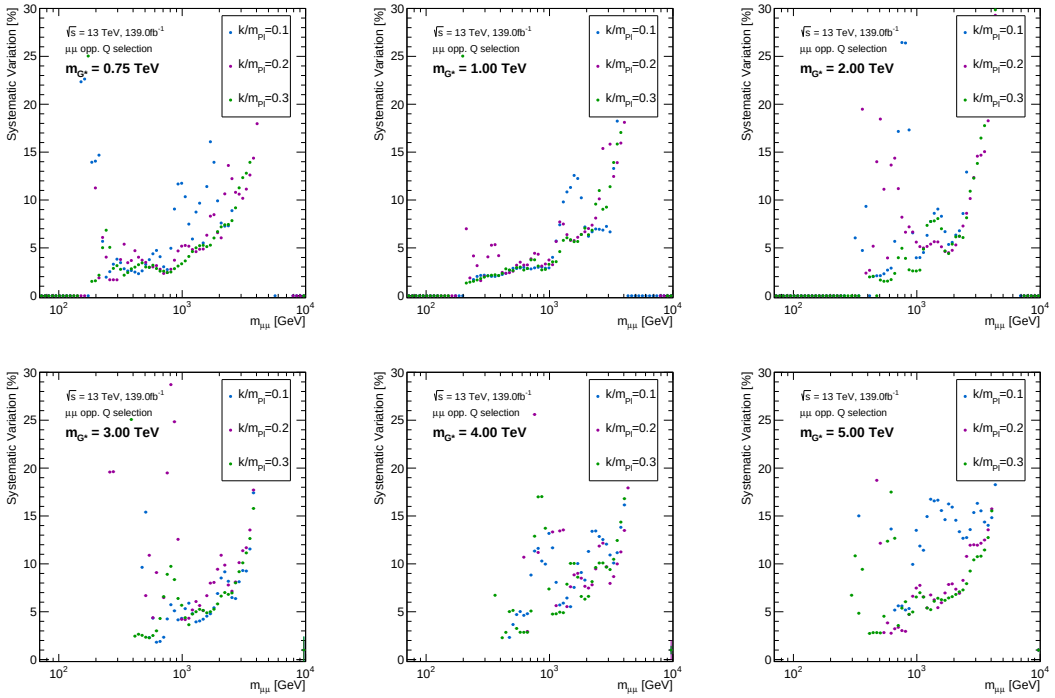

(b) Signal systematics in dimuon channel.

Figure B.5: Signal systematics in (a) dielectron and (b) dimuon channels for masses $m_{G^*} \in [0.75, 5.00]$ TeV.

Bibliography

[1] M. E. Peskin and D. V. Schroeder, *An Introduction to Quantum Field Theory.* Westview Press, 1995.

[2] M. Thomson, *Modern Particle Physics.* Cambridge University Press, fourth ed., 2013.

[3] E. Noether, *Invariant variation problems*, *Transport Theory and Statistical Physics* **1** (Jan, 1971) 186–207.

[4] C. S. Wu, E. Ambler, R. W. Hayward, D. D. Hoppes and R. P. Hudson, *Experimental test of parity conservation in beta decay*, *Phys. Rev.* **105** (Feb, 1957) 1413–1415.

[5] S. L. Glashow, *Partial-symmetries of weak interactions*, *Nuclear Physics* **22** (1961) 579–588.

[6] F. Englert and R. Brout, *Broken Symmetry and the Mass of Gauge Vector Mesons*, *Phys. Rev. Lett.* **13** (Aug, 1964) 321–323.

[7] S. L. Glashow, *The renormalizability of vector meson interactions*, *Nuclear Physics* **10** (1959) 107 – 117.

[8] A. Salam and J. Ward, *Electromagnetic and weak interactions*, *Physics Letters* **13** (1964) 168–171.

[9] S. Weinberg, *A model of leptons*, *Phys. Rev. Lett.* **19** (Nov, 1967) 1264–1266.

[10] P. W. Higgs, *Broken Symmetries and the Masses of Gauge Bosons*, *Phys. Rev. Lett.* **13** (Oct, 1964) 508–509.

[11] ATLAS collaboration, *Observation of a new particle in the search for the standard model higgs boson with the ATLAS detector at the LHC*, *Physics Letters B* **716** (2012) 1–29.

[12] Purcell, A, *The Standard Model infographic developed at the webfest*, 2012.

[13] D. Tong, *Lectures on String Theory.* 2009.

[14] A. Shomer, *A pedagogical explanation for the non-renormalizability of gravity*, Feb, 2008. **0709.3555**.

[15] L. Randall and R. Sundrum, *Large Mass Hierarchy from a Small Extra Dimension*, *Phys. Rev. Lett.* **83** (Oct, 1999) 3370–3373.

[16] L. Randall and R. Sundrum, *An Alternative to Compactification*, *Phys. Rev. Lett.* **83** (Dec, 1999) 4690–4693.

[17] N. Arkani-Hamed, S. Dimopoulos and G. Dvali, *The Hierarchy Problem and New Dimensions at a Millimeter*, *Physics Letters B* **429** (Jun, 1998) 263–â272.

[18] F. Ravndal, *Oskar Klein and the fifth dimension*, Sep, 2013. **1309.4113**.

[19] T. Kaluza, *On the Unification Problem in Physics*, *International Journal of Modern Physics D* **27** (Oct, 2018) 1870001.

[20] O. Klein, *The Atomicity of Electricity as Quantum Theory Law*, *Nature* **118** (Sep, 1926) 516–516.

[21] G. Moore, *What is... a Brane?*, Feb, 2005. `https://www.ams.org/notices/200502/what-is.pdf`.

[22] N. Arkani-Hamed, S. Dimopoulos and G. Dvali, *Phenomenology, astrophysics, and cosmology of theories with submillimeter dimensions and tev scale quantum gravity*, *Physical Review D* **59** (Mar, 1999) .

[23] J. Lykken and L. Randall, *The shape of gravity*, *Journal of High Energy Physics* **2000** (Jun, 2000) 014–014.

[24] B. C. Allanach, K. Odagiri, M. A. Parker and B. R. Webber, *Searching for narrow graviton resonances with the ATLAS detector at the large hadron collider*, *Journal of High Energy Physics* **2000** (Sep, 2000) 019–019.

[25] D. Green, *High p_T Physics at Hadron Colliders*. Cambridge University Press, 2005.

[26] A. D. Martin, W. J. Stirling, R. S. Thorne and G. Watt, *Parton distributions for the LHC*, *The European Physical Journal C* **63** (Sep, 2009) 189–285.

[27] ATLAS collaboration, G. Aad et al., *Search for high-mass dilepton resonances in pp collisions at $\sqrt{s} = 8\,\text{TeV}$ with the ATLAS detector*, *Phys. Rev. D* **90** (Sep, 2014) 052005.

[28] W. R. Leo, *Techniques for Nuclear and Particle Physics Experiments*. Springer-Verlag, 1 ed., 1987.

[29] ATLAS collaboration, *The ATLAS Experiment at the CERN Large Hadron Collider*, *Journal of Instrumentation* **3** (Aug, 2008) S08003–S08003.

[30] M. Aaboud, G. Aad, B. Abbott et al., *Electron reconstruction and identification in the ATLAS experiment using the 2015 and 2016 LHC proton-proton collision data at* $\sqrt{s} = 13\,\text{TeV}$, *The European Physical Journal C* **79** (Aug, 2019) 639–639.

[31] ATLAS collaboration, *Muon reconstruction performance of the ATLAS detector in proton–proton collision data at* $\sqrt{s} = 13\,\text{TeV}$, Dec, 2020. **2012.00578**.

[32] J. Pequenao and P. Schaffner, *How ATLAS detects particles: diagram of particle paths in the detector*, Jan, 2013. `http://cds.cern.ch/record/1505342?ln=en`.

[33] A. Salvucci, *Measurement of muon momentum resolution of the ATLAS detector*, *EPJ Web of Conferences* **28** (Jan, 2012) 12039.

[34] W. Lampl, S. Laplace, D. Lelas, P. Loch, H. Ma, S. Menke et al., *Calorimeter Clustering Algorithms: Description and Performance*, Tech. Rep. ATL-LARG-PUB-2008-002. ATL-COM-LARG-2008-003, CERN, Geneva, Apr, 2008.

[35] O. Behnke, K. Kröninger, G. Schott and T. Schörner-Sadenius, *Data Analysis in High Energy Physics*. WILEY-VCH Verlag GmbH Co. KGaA, 2013.

[36] Z. Marshall, *SUSY Object Definitions (Rel 21)*, Jun, 2020. `https://twiki.cern.ch/twiki/bin/view/AtlasProtected/SusyObjectDefinitionsr2113TeV`.

[37] V. Morisbak, *Searching for new forces of Nature: New neutral gauge bosons in dimuon final states with the ATLAS detector at the LHC*. PhD dissertation, University of Oslo, 2021.

[38] A. Caldwell, D. Kollár and K. Kröninger, *BAT–The Bayesian analysis toolkit*, *Computer Physics Communications* **180** (Nov, 2009) 2197–2209.

[39] N. Metropolis, A. W. Rosenbluth, M. N. Rosenbluth, A. H. Teller and E. Teller, *Equation of state calculations by fast computing machines*, *The journal of chemical physics* **21** (1953) 1087–1092.

[40] Particle Data Group collaboration, *Review of Particle Physics*, *Phys. Rev. D* **98** (Aug, 2018) 030001.

[41] M. Pedersen, *Fake lepton determination, Supersymmetry searches in di-lepton final states, and sharing ATLAS research with young students*. PhD dissertation, University of Oslo, 2014.

[42] S. Alioli, P. Nason, C. Oleari and E. Re, *A general framework for implementing NLO calculations in shower Monte Carlo programs: the POWHEG BOX*, *Journal of High Energy Physics* **2010** (Jun, 2010) .

[43] T. Sjöstrand, S. Mrenna and P. Skands, *A brief introduction to PYTHIA 8.1*, *Computer Physics Communications* **178** (2008) 852–867.

[44] T. Gleisberg, S. Höche, F. Krauss, M. Schönherr, S. Schumann, F. Siegert et al., *Event generation with SHERPA 1.1*, *Journal of High Energy Physics* **2009** (Feb, 2009) 007–007.

[45] S. Agostinelli et al., *GEANT4 - A simulation toolkit*, *Nuclear Instruments and Methods in Physics Research Section A: Accelerators, Spectrometers, Detectors and Associated Equipment* **506** (2003) 250–303.

[46] S. Zambito, *MuonSelectionTool in Rel. 21*, Feb, 2021. `https://twiki.cern.ch/twiki/bin/view/Atlas/MuonSelectionToolR21`.

[47] M. K. Bugge, *Search for new charged bosons and dark matter in final states with one lepton and missing transverse energy with the ATLAS detector at the LHC.* PhD dissertation, University of Oslo, 2015.

[48] E. Gramstad, *Searches for Supersymmetry in di-Lepton Final States with the ATLAS Detector at* $\sqrt{s} = 7\,\text{TeV}$. PhD dissertation, University of Oslo, 2013.

[49] ATLAS collaboration, *Search for new high-mass phenomena in the dilepton final state using* $36\,\text{fb}^{-1}$ *of proton-proton collision data at* $\sqrt{s} = 13$ TeV *with the ATLAS detector*, *J. High Energ. Phys.* **182** (Oct., 2017) .

[50] CMS collaboration, *Search for resonant and nonresonant new phenomena in high-mass dilepton final states at* $\sqrt{s} = 13$ *TeV*, Mar, 2021. **2103.02708**.

[51] CMS collaboration, *Search for resonant and nonresonant new phenomena in high-mass dilepton final states at* $\sqrt{s} = 13\,\text{TeV}$. *HEPDATA*, 2021. **101186**.

[52] CMS collaboration, A. M. Sirunyan, A. Tumasyan et al., *Search for high-mass resonances in dilepton final states in proton-proton collisions at* $\sqrt{s} = 13\,\text{TeV}$, *Journal of High Energy Physics* **2018** .

[53] S. M. Carroll, *Spacetime and Geometry.* Cambridge University Press, Sep, 2019.

[54] S. M. Carroll, *Lecture Notes on General Relativity*, 1997.